

DISSERTATION

Large Crystal Neutron Interferometer Measurements

ausgeführt zum Zwecke der Erlangung des akademischen Grades eines
Doktors der technischen Wissenschaften unter der Leitung von

Univ.-Doz. Dipl.-Ing. Dr. Martin Suda
Ass.-Prof. Dipl.-Ing. Dr. Michael Zawisky
E141 - Atominstitut

eingereicht an der Technischen Universität Wien
Fakultät für Physik

von

Dipl.-Ing. Thomas Potocar
Matrikelnummer: 0230211
Mostgasse 8
A-1040 Wien

Wien, am 6. April 2016

Acknowledgment

This thesis was written at the Institute of Atomic and Subatomic Physics, Technical University of Vienna, in cooperation with the Institut Laue-Langevin in Grenoble and the Physikalisch-Technische Bundesanstalt in Braunschweig (PTB).

I specially would like to thank my supervisors Martin Suda (Martin.Suda.fl@ait.ac.at) and Michael Zawisky (zawisky@ati.ac.at) for their great support and also the whole institute, inter alia Hartmut Lemmel, Josef Springer and Martin Fally.

Interferometer preparation: thanks to U. Kuetgens, J. Hauffe, et. al (Ulrich.Kuetgens@ptb.de, Jens.Hauffe@ptb.de) from the PTB, as well as the Rauch Ges.m.b.H. Thanks to H. Huber for the fabrication of an interferometer model.

Chameleon experiment: T. Jenke, H. Lemmel, G. Pignol, P. Brax, H. Abele, A. Ivanov, M. Pitschmann, M. Wellenzohn, M. Faber as well as P. Geltenbort and T. Brenner from PF2, to support us with a Scrollpump, vacuum tubes and connections, leak valve motor etc.

Further experiments were attended (during the drill on the instrument S18 as well as substitute for the instrument responsible):

- S. Abbas, A. Wagh, H. Lemmel, T. Potocar, H. Rauch: 'High-precision determination of Si-neutron coherent scattering length with a dual non-dispersive sample', AIP Conference Proceedings, 1447 (2012), 479 - 480
- A. Freund, and C. Rehm: 'Effect of crystal shape on neutron rocking curves of perfect single crystals designed for ultra-small-angle scattering experiments', Journal of Physics: Conference Series, 528 (2014), 012002
- Y. Otake, M. Olbinato, et al: 'Research toward the development of compact neutron interference imaging instrument with gratings', Journal of Physics: Conference Series 340 (2012), 011035

Additionally, I want to acknowledge my family, as well as the Austrian Science Fund (FWF, Proj. No. I530-N20) and CENI, Central European Neutron Initiative, the Collaboration Agreement between ILL and TU-Wien (ILL-1132.1-3) for financial support.



Kurzfassung

In dieser Arbeit untersuchen wir den Phasenschub bei Lauetransmission in einer Silizium-Perfektkristallplatte im Detail. Diese 'Laue Phase' wurde bei zwei Wellenlängen, nahe der Bragg-Bedingung, mit einem Neutroneninterferometer gemessen. Insbesondere konnten wir die Empfindlichkeit der Laue Phase bezüglich der Justage des Monochromators zum Interferometer (Rocking Winkel) und der Strahldivergenz nachweisen. Die bemerkenswerte Phasensteigung von 5.5° [(220) Bragg peak] und 11.5° [(440) Bragg peak] pro 0.001 Bogensekunden vom Bragg-Winkel, konnte erreicht werden. Die Analyse der Ergebnisse erfolgte mit einer Software, die hier ebenfalls präsentiert wird.

Weiters, werden die Fertigungsschritte des weltweit grössten Perfektkristall- Neutroneninterferometers vorgestellt ($30 \times 12 \text{ cm}^2$). Ausgehend von einem sehr speziellen Design zur Verbesserung der Winkelauflösung, wurde die Kristallorientierung, das Schneiden und Schleifen, sowie das Ätzen durchgeführt. Die ersten Testmessungen am ILL zeigten bereits einen Interferenzeffekt. Schließlich werden mögliche Anwendungen angesprochen, in denen die grossen Strahlflächen von Interesse sind, z.B. Messungen von Schwerkraft-induzierten Phaseneffekten und hochauflösende Winkelmessungen.

Zusätzlich erfolgte die Durchführung eines weiteren Interferometer-Experiments. Mit einer Vakuumkammer untersuchen wir die so genannte 'Chamäleon' Phase. Sie ist ein Kandidat für die Dunkle Energie. Mit dieser Methode ergibt sich, dass die Chamäleonfeld-Kopplungskonstante β kleiner sein muss als $1.9 \cdot 10^7$. Dieser Grenzwert ist um mehr als eine Größenordnung besser als der momentan angegebene Wert von $5.8 \cdot 10^8$.

Abstract

In this study, we investigate the phase shift induced by Laue transmission in a perfect silicon (Si) crystal blade in detail. This 'Laue phase' was measured at two wavelengths in the vicinity of the Bragg condition within a neutron interferometer. In particular, the sensitivity of the Laue phase to the alignment of the monochromator and interferometer (rocking angle) and beam divergence has been verified. However, the influence of fundamental quantities, such as the neutron-electron scattering length on the Laue phase is rather small. The fascinating steep phase slope of 5.5° [(220) Bragg peak] and 11.5° [(440) Bragg peak] per 0.001 arcsec deviation from the Bragg angle has been achieved. The results are analyzed using an upgraded calculation tool.

Furthermore, the fabrication stages of the world's largest crystal interferometer are presented ($30 \times 12 \text{ cm}^2$). Starting from a very special design for increasing the angular resolution, the crystal orientation, cutting, fine grinding, and etching have been performed. First test measurements at the ILL show the expected interference effect. Finally, possible applications are discussed where the large area enclosed by the interfering beams can be of great value, e.g. measurements of gravity induced phase effects and high angular resolution experiments.

A further interferometric experiment has been performed as well. With a vacuum chamber, we investigate the so called 'chameleon' phase. It is a candidate for dark energy. We found with our method, that the chameleon field coupling constant β must be smaller than $1.9 \cdot 10^7$. This limit is more than one order better than the current value of $5.8 \cdot 10^8$.

Contents

1. Introduction	1
2. Laue phase	7
2.1. Theoretical	7
2.1.1. Dynamical diffraction theory	7
2.1.2. Laue transmission phase	11
2.2. Experimental	16
2.2.1. Experimental setup	16
2.2.2. Measurement principle	21
2.3. Measurements and Calculations	23
2.3.1. (220) case	23
2.3.2. (440) case	26
2.3.3. Measured $\delta\theta$ -shift	26
2.4. Systematic effects on the Laue phase	30
2.4.1. Interferometer geometry	32
2.4.2. Temperature	40
2.4.3. Monochromator	44
2.4.4. Beam divergence	47
2.4.5. Rocking position	51
2.4.6. Al prisms	54
2.4.7. Wavelength	64
2.4.8. Scattering length	68
2.5. Relative Laue method	71
2.5.1. Scattering length	73
2.5.2. Measurement with the relative Laue method	74
3. Preparation of a new interferometer	77
3.1. Dimensions and key parameters	77
3.2. Preparation steps	78
3.2.1. Silicon perfect crystal ingot	78
3.2.2. Cutting	79
3.2.3. Orientation	80
3.2.4. Grinding	81
3.2.5. Etching	83
3.2.6. Final geometry	84
3.3. Original version	86
3.4. Testing the new interferometer	88

4. Chameleons	91
4.1. Theoretical	91
4.2. Experimental	95
4.3. Measurement	99
4.3.1. Method I: phase vs. pressure (at fixed chamber position)	99
4.3.2. Method II: phase vs. chamber position	101
4.3.3. Method III: phase (between 2 chamber pos.) vs. p	102
5. Summary and conclusions	105
A. Supplements	107
A.1. IFMSIM	107
A.2. Data analysis script for Igor Pro	110
A.3. Labview control program	111
A.4. Interferometer	112
A.5. Temperature setup	115
A.6. Determination of σ_θ with rocking curves	121
A.7. Rocking position, further influences	125
A.8. Scattering length tables	126
A.9. New interferometer: geometry measurement	129
A.10. Chameleon method II: wall thickness	131
Bibliography	133

1. Introduction

Throughout this work, thermal neutrons (n) have been used for interferometry. Some properties of the neutrons are listed in tab. 1.1. The lifetime (β decay¹) of the free neutron is 14 min and 47(2) sec, and it can be influenced via the gravity, weak, strong, and electromagnetic interaction. Some wavelength ranges are listed as well. The existence of the neutron was predicted by Ernest Rutherford (1920) and experimentally discovered by James Chadwick (1932), which led to nuclear power production (1942) and to nuclear weapons (1945).

Table 1.1.: Properties of the free neutron. $E = m_n \cdot v^2/2$ is the kinetic energy of the neutron with group velocity v .

Mass	$m_n = 1.67492716(13) \cdot 10^{-27}$ kg
Spin	$s = \hbar/2$ (fermion)
Lifetime	887(2) s
Baryon	1 up, 2 down quarks
Compton wavelength	$\lambda_C = h/(m_n c) = 1.319695(20) \cdot 10^{-6}$ nm
De Broglie wavelength	$\lambda = h/(m_n v)$
Ultracold n	$E < 0.2$ meV, $\lambda > 2$ nm
Cold n	$E < 2$ meV, $\lambda = 2000 \dots 640$ pm
Thermal n	$E < 100$ meV, $\lambda = 640 \dots 90$ pm
Epithermal n	$E < 1$ eV, $\lambda = 90 \dots 28$ pm

A Mach-Zehnder type interferometer (IFM) has been used. Due to the difficult alignment of the beam splitter/mirrors/analyzer, the blades are cut from a single crystal Si ingot, fig. 1.1.

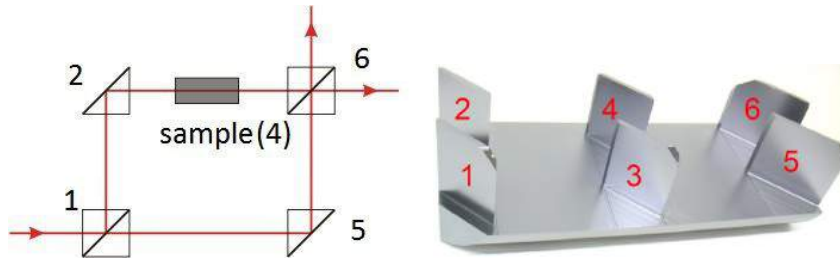


Figure 1.1.: Mach-Zehnder interferometer principle (left) and a 6 blade neutron interferometer (right), (1)...(6) blades/sample.

¹ $n \rightarrow p^+ + e^- + \bar{\nu}_e$ (proton mass $m_p = 1.672621777(74) \cdot 10^{-27}$ kg, electron mass $m_e = 9.10938291(40) \cdot 10^{-31}$, antineutrino $\bar{\nu}_e$ (mass: 'KATRIN' experiment))

Like for x-ray interferometers, the interaction of the neutron wave within the IFM is described by the dynamical theory of diffraction [1]. The phase shift of a material in the interferometer is given by [2]:

$$\phi = -\lambda N b D \quad (1.1)$$

with the number of nuclei per unit volume N , the coherent scattering length b and the sample thickness D . Diffraction from the lattice planes of a perfect single crystal allow coherent splitting of an incident neutron beam, according to Bragg's law (William Lawrence Bragg 1912):

$$\lambda = 2d_L \cdot \sin \theta_B \quad (1.2)$$

with d_L , the spacing between the planes in the atomic lattice.

Chap. 2 is dedicated to the Laue phase, where a large 6-blade Si perfect crystal interferometer with precisely oriented lattice planes was used; the planes are perpendicular to the lamella surfaces within 13.5 arcsec ($''$). The IFM is shown in fig. 1.2, together with the sample. As sample serves a lamella of the interferometer, because it is already

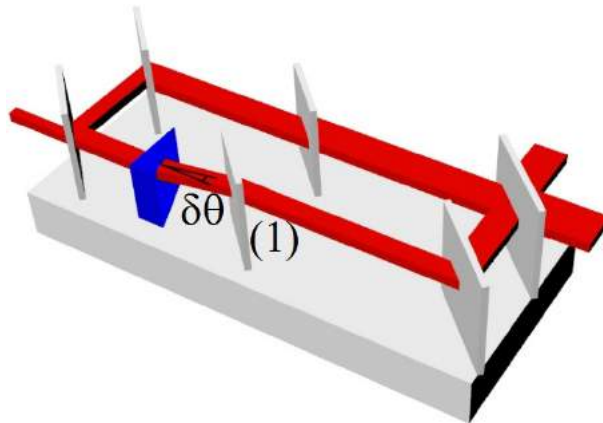


Figure 1.2.: Laue phase measurement principle: neutron interferometer with a prism to deflect ($\delta\theta$) the beam in front of the sample (1).

perfectly aligned. The phase change versus a small beam deviation, close to the Bragg condition is the 'Laue phase'. First measurements to this phase are presented in [4]. They offer in principle the possibility of extracting fundamental quantities such as the neutron-electron scattering length, gravitational short-range interactions and the Debye-Waller factor [5], [6]. For this purpose, it is necessary to improve the accuracy of the phase measurement - and consider all systematic phase effects in the analysis. Reference [4] left several open questions concerning the influence of different parameters, therefore this work presents a more systematic investigation of the Laue phase. Important parameters are the type of monochromator, its mosaicity, rocking position (alignment angle between monochromator and interferometer) and IFM geometry. As experimental improvements, an aluminum box for temperature stabilization of the interferometer has been installed, the number of measurements have been increased and the angular range of the beam deflection has been further enlarged. We compare the experiment with theoretical calculations of the Laue phase. All these calculations are performed using an upgraded simulation tool, using less free parameters and more calculation possibilities;

a detailed description of the software 'IFMSIM' is provided in [7]. Previous publications related to the Laue phase are [1], [4], [5], [8], [9], [10], [11], [12]. Our results are published in the journal 'Acta Crystallographica Section A: Foundations of Crystallography' [13].

In chap. 3 the preparation of a new IFM, the world's largest Si perfect-crystal neutron interferometer is described (fig. 1.3). To reduce disturbances, a thick basis for such a large interferometer is of interest. The non-trivial fabrication steps are performed together with our co-operation partner at the 'Physikalisch-Technische-Bundesanstalt' (PTB in Germany). Possible applications will be for instance the gravity induced phase experiment 'COW' [14] and high angular resolution measurement, where the Laue phase can be used to detect very small beam deflections [15]. For this, a large area of the enclosed interfering beams as well as thick sample lamellas are necessary.



Figure 1.3.: New IFM (left) together with the first Si perfect crystal IFM (right).

In chap. 4 an astrophysical application for neutron interferometry is given [16]. A theoretical scalar field (chameleons) describing the dark energy is discussed and a measurement in a vacuum cell is performed (fig. 1.4). This cell serves as a sample in the IFM, a phase shift due to the chameleon field is predicted at low pressure. Dark energy is introduced to explain the observations that the universe is expanding at an accelerating rate. The universe contains 4.9% ordinary matter, 26.8% dark matter and 68.3% dark energy [18]. The results are published in 'Physical Letters B' [19]².

²The article is also available at 'ArXiv: 1502.06023 (2015)'.

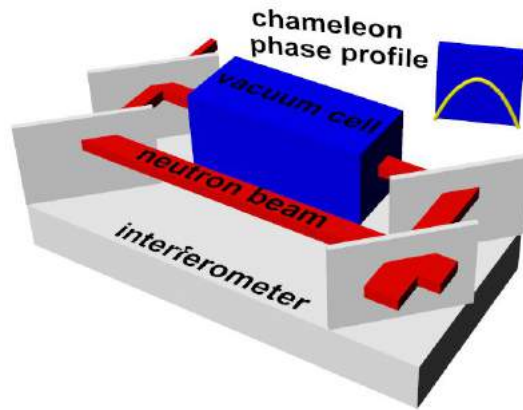


Figure 1.4.: Chameleon experiment: neutron interferometer with vacuum chamber. The theoretically predicted phase profile between the chamber walls is shown as well.

All measurements were performed at the instrument S18 at ILL Grenoble fig. 1.5, 1.6. The institute was founded 1967 by France and Germany and is named after Max von Laue (German, crystal structure from x-ray diffraction) and Paul Langevin (French, neutron moderation).

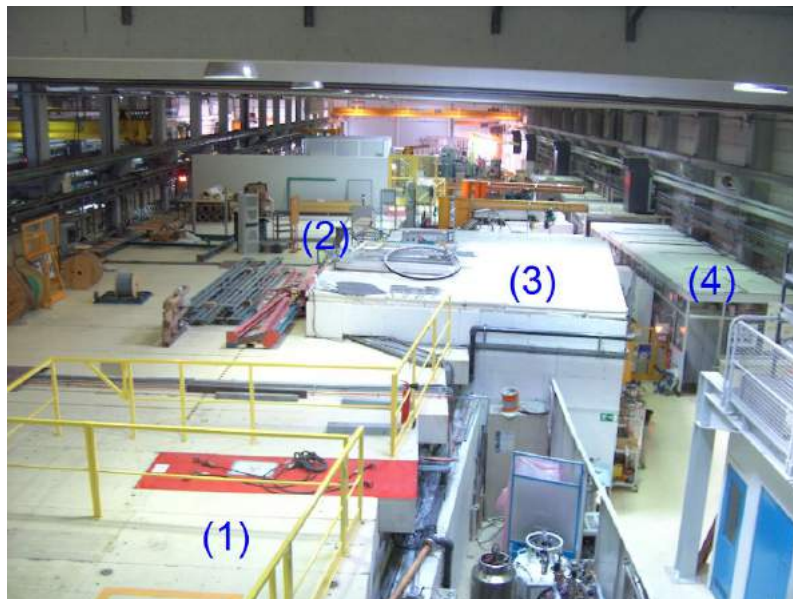


Figure 1.5.: Neutron guide hall at ILL. (1) Neutron guide from the reactor, (2) vacuum pump for the neutron guide, (3) S18 measuring hut, (4) S18 control room.

2. Laue phase

2.1. Theoretical

2.1.1. Dynamical diffraction theory

The dynamical diffraction theory describes the behavior of neutrons passing through a periodic potential, like the interferometer blades [2], [3], [21], [22]. A detailed description for x-rays, where the absorption is not negligible is given in [1], [23], [24]. Furthermore, the electron case can be found in [25], [26].

Within this theory, the neutron wave function ψ is calculated inside the crystal by solving the stationary Schroedinger equation:

$$\left(-\frac{\hbar^2}{2m_n}\Delta + V(\vec{r}) \right) \psi(\vec{r}) = E\psi(\vec{r}) \quad (2.1)$$

With the boundary conditions of continuity on the crystal surface, this leads to a equation of the allowed wave vectors inside the crystal ('dispersion surfaces').

The reduced Planck constant $\hbar = 1.05457 \cdot 10^{-34}$ Js, Δ is the Laplace operator, m_n represents the neutron mass (tab. 1.1), $E = \hbar^2 K^2 / (2m_n)$ its energy, and \vec{r} represents the spatial vector (\vec{K} is the wave vector, K is the wave number inside the crystal).

A Bloch ansatz for

$$\psi(\vec{r}) = e^{i\vec{K}\vec{r}} \sum_H u_H e^{i\vec{H}\vec{r}} \quad (2.2)$$

is used, as well as the Fermi pseudo potential:

$$V(\vec{r}) = \frac{2\pi\hbar^2 b}{m_n} \sum_i \delta(\vec{r} - \vec{r}_i) \quad (2.3)$$

Here, \vec{H} is the reciprocal lattice vector, u_H the amplitude, and \vec{r}_i is the position of the nucleus; the scattering length b describes the scattering power of a particular isotope.

Inserting eq. 2.2 and eq. 2.3 in eq. 2.1, leads to a system of equations, where an one- and two-beam approximation can be used. In case the crystal is oriented with respect to the incident beam, so that more reflections are excited simultaneously, then this is called the 'multiple-beam case'¹.

¹In general this would be the case in our setup for the Si (220) reflection and the exact $\theta_B = 45^\circ$ angle, where the (-220) and (040) reflections are due the Bragg's law simultaneously excited [27]. However, these diffracted intensities are by three orders of magnitude lower as compared to the intensity of the (220) because these reflections are in the dispersive arrangement with respect to the perfect crystal monochromator.

In the case of the **one beam approximation**, the phase shifter is described (this is equivalent to the model of index of refraction). The beam angle is far off the Bragg condition or the sample is non-crystalline. The incident wave is for instance given by a plane wave: $e^{i\vec{k}\vec{r}}$ where \vec{k} is the wave vector outside the sample ($k = |\vec{k}| = 2\pi/\lambda$). The wave number inside the crystal K_0 is given by:

$$K_0 = k \cdot \sqrt{1 - V_0/E} \approx k \cdot \left(1 - \frac{V_0}{2E}\right) \quad (2.4)$$

with the mean crystal potential (characterizing the medium) $V_0 = 2\pi\hbar^2 Nb/m_n$, which is significantly smaller than the energy of the incoming neutrons. N representing the atomic number density, which is: $8/a^3 = 4.9939669 \cdot 10^{22} \text{ cm}^{-3}$ for Si. The lattice constant a for Si is $5.431020504(89) \cdot 10^{-10} \text{ m}$ at 22.5°C [28]. Similar to light optics, the index of refraction for such a potential is given by:

$$n = \frac{K_0}{k} \approx 1 - \lambda^2 \frac{Nb}{2\pi} \quad (2.5)$$

In the case of the **two beam approximation** of the dynamical diffraction theory, the IFM blade (the Si single crystal) with the beam approximately satisfying the Bragg condition is described. Additional to the transmitted beam, a reflected beam is observed. The reflected wave is given by: $r \cdot e^{i\vec{k}_H\vec{r}}$ where r is the reflection amplitude and \vec{k}_H the wave vector of the reflected beam. The reflected wave vector inside the crystal is $\vec{K}_H = \vec{K}_0 + \vec{H}$. The transmission and reflection amplitudes of the lattice planes for the neutron wave function behind a crystal are given by [11]:

$$t(\eta) = \exp \left[-iA_0(1 + \bar{\epsilon}) - A_H \cdot \eta \right] \left(\cos(A_H \sqrt{1 + \eta^2}(1 + \epsilon)) + \frac{i\eta}{\sqrt{1 + \eta^2}} \sin [A_H \sqrt{1 + \eta^2}(1 + \epsilon)] \right) \quad (2.6)$$

$$r(\eta) = \exp \left[-iA_0(1 + \bar{\epsilon}) + iA_H \cdot \eta + iz_0\eta k|V_H|/(E \cos \theta_B) \right] \cdot \sqrt{\frac{V_H}{V_{-H}}} \frac{-i}{\sqrt{1 + \eta^2}} \sin [A_H \sqrt{1 + \eta^2}(1 + \epsilon)] \quad (2.7)$$

where $\bar{\epsilon} = \epsilon(1 + |V_H|^2/V_0^2)/2$, $\epsilon = |V_H|/(2E \cos^2 \theta_B)$, z_0 the position of the crystal blade and:

$$\eta = 2 \sin \theta_B [\sin \theta_B - \sin(\theta_B - \delta\theta)] \cdot E/|V_H| \quad (2.8)$$

As our study concerns only very small angles, η is then equal to the usually used y -parameter:

$$y = -\delta\theta \cdot \sin(2\theta_B) \cdot E/|V_H| \quad (2.9)$$

D represents the thickness of the crystal, $A_0 = DkV_0/(2E \cos \theta_B)$ and:

$$\begin{aligned} A_H &= \pi D / \Delta_H \\ \Delta_H &= \frac{\pi}{2d_L(\vec{H})Nb(\vec{H})e^{-W(\vec{H})} \tan \theta_B} \end{aligned}$$

Here, $\delta\theta$ is the beam deviation from the Bragg angle $\theta_B = 45^\circ$, $V_H = \frac{\pi\hbar^2 N}{4m_n} b(\vec{H})F(\vec{H})$ is the crystal potential, and Δ_H denotes the Pendelloesung length², with $d_L(\vec{H}) = a/\sqrt{h^2 + k^2 + l^2}$ the lattice plane distance (h,k,l are the Miller indices), and W representing the Debye-Waller factor (chap. 2.4.8). The absolute value of the momentum transfer is given by $H = 2\pi/d_L$, and $F(\vec{H})$ is the structure factor³. Note that b is here the atomic scattering length, which includes the constant b_N and adds momentum transfer dependent the neutron-electron scattering length (chap. 2.4.8).

The Bragg reflected beam shows a Lorentzian-shaped peak with rapid oscillations (versus y), which are due to the interference of two internal wave fields with slightly different wave vectors. This 'Pendelloesung oscillations' depend on the ratio of the crystal thickness and the Pendelloesung length.

An average over these oscillations yields:

$$\langle I_H(y) \rangle = \frac{1}{2(1 + y^2)} \quad (2.10)$$

and

$$\langle I_0(y) \rangle = \frac{1}{2} \left(1 + \frac{y^2}{1 + y^2} \right) \quad (2.11)$$

The average reflected intensity falls to half its maximum value when the y -parameter is unity (Darwin width):

$$\Delta\theta_{1/2} = \frac{\lambda^2 N F(\vec{H}) b(\vec{H})}{8\pi \sin 2\theta_B} \quad (2.12)$$

The Darwin width therefore describes the angular acceptance of a crystal.

²According to the dynamical theory of diffraction, the Pendelloesung length describes the period length of the wave field oscillation within the crystal [31].

³For Si: $F = 8$ (sum of the Miller indices is divisible by 4), $F = 4 \pm i4$ (Miller indices all odd) and $F = 0$ (all other cases).

Laue vs. Bragg geometry: depending whether the reflected beam leaves on the front or back surface of the blade, one distinguishes between the Laue and Bragg geometry, as illustrated in fig. 2.1. The lattice planes are parallel (Laue) or perpendicular (Bragg) to the surface normal, as we consider here the 'symmetric Laue case', the lattice planes are oriented exactly parallel to the crystal surface normal. The blades of the interferometer are cut in Laue geometry.

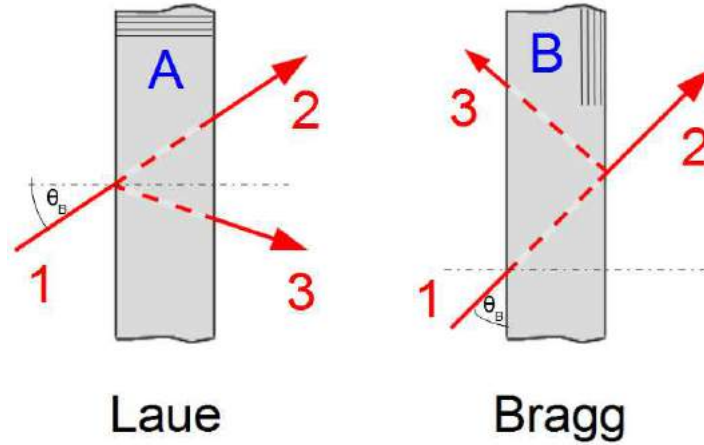


Figure 2.1.: (A) Laue geometry, lattice planes parallel to the surface normal (dashed dotted line), (B) Bragg geometry, lattice planes perpendicular to the surface normal. (1) Incident neutron beam, (2) transmitted beam, (3) reflected beam. θ_B is the Bragg angle, eq. 1.2 .

2.1.2. Laue transmission phase

The interferometer blades are cut in Laue geometry, therefore we will call the phase in the transmitted beam 'Laue transmission phase' or short 'Laue phase', as introduced in [4]. Note that in Ref. [11] the name 'diffractive phase' and in Ref. [5] 'dynamical phase' is used.

In the following, the properties of the phase are given, first with a plane wave as incident beam and secondly as a superposition of plane waves, creating a spherical wave. The Laue phase is antisymmetric with respect to the very small (0.1 arcsec) crystal rotation angle $\delta\theta$. The extreme angular sensitivity and the non-linearity in the y -parameter are important, since they constitute the main difference to the phase shift induced by a non-crystalline material or a perfect-crystal far off any Bragg condition. Close to θ_B , the angular dependence of the phase is determined by the crystal thickness and the lattice plane distance.

Plane Wave

The argument⁴ of the transmission factor in eq. 2.6 gives the Laue phase of the neutron beam in forward direction $\phi(\eta) = \arg[t(\eta)]$. An analytical expression of this phase for a monochromatic plane wave in a perfect crystal blade is [4]:

$$\begin{aligned} \phi_{Laue}(\eta) = & -A_0(1 + \bar{\epsilon}) - A_H\eta \\ & + \arctan \left[\frac{\eta}{\sqrt{1 + \eta^2}} \tan[A_H\sqrt{1 + \eta^2}(1 + \epsilon)] \right] \end{aligned} \quad (2.13)$$

As mentioned before, we use only small angles where η is equal to y .

The non-linearity of the phase in the y -parameter is described by the arctan term (or equivalently $\cos[A_H\sqrt{1 + y^2}] + \frac{iy}{1+y^2} \sin[A_H\sqrt{1 + y^2}]$ in eq. 2.6). These structures are related to the before mentioned Pendelloesung oscillations, therefore we will call this phase nonlinearities 'Pendelloesung plateaus'. An important point is, that the sensitivity to fundamental parameters, such as the scattering length, is enhanced here. This can be seen in eq. 2.13, the phase plateaus are at the poles of the tangent function, small changes in its argument $A_H\sqrt{1 + y^2} = (2n + 1)\pi/2$ show an enhanced sensitivity to the phase.

The Laue phase for this plane wave case will be compared with the spherical theory later, see fig. 2.3.

An **approximation** in the limit $|y| \rightarrow \infty$ is given in [36] :

$$\phi_{Laue;approx}(y) = \phi_{Laue;approx}(0) - A_H(y \pm \sqrt{1 + y^2}) \quad (2.14)$$

The plus (minus) sign corresponding to positive (negative) y .

Closely around the Bragg condition, the Laue phase can be approximated for thick crystals by [15]:

$$\phi_{Laue}(y) \approx \phi_{Laue}(0) - y \cdot A_H + O(y^3) \quad (2.15)$$

$$\phi_{Laue}(\delta\theta) \approx \phi_{Laue}(0) + \delta\theta \cdot \pi D/d_L + O(\delta\theta^3) \quad (2.16)$$

so just depending on the ratio between crystal thickness and lattice plane distance.

⁴The 'argument' means the angle between a complex number with the positive real axis.

Spherical theory

Note that in eq. 2.13 the phase is calculated using just a plane wave, our calculations⁵ however consider a **coherent superposition of many plane waves** [7], [11]. This creates a localized beam, it is a coherent wave packet with the divergence σ_α with a point source at \vec{r}_0 in the direction α_0 . The wave function in real space is given by a Fourier transform of the wave function in momentum space:

$$\psi(\vec{r}) = \frac{1}{2\pi} \int d^2k e^{i\vec{k}(\vec{r}-\vec{r}_0)} \psi(\vec{k}) = \frac{k_0}{2\pi} \int_{-\pi}^{\pi} d\alpha g_\alpha(\alpha) e^{i\vec{k}_0(\vec{r}-\vec{r}_0)} \quad (2.17)$$

where in the momentum space and with polar coordinates the wave function is $\psi(k, \alpha) = \delta(k - k_0) g_\alpha(\alpha)$. As a simplification, the calculations are monochromatic⁶ and our 'spherical' beam is rather a two-dimensional beam with a representation in polar coordinates.

As an angular distribution one can use a Gaussian function:

$$g_\alpha = \frac{1}{\sqrt{2\pi\sigma_\alpha^2}} \cdot \exp\left(-\frac{(\alpha - \alpha_0)^2}{2\sigma_\alpha^2}\right), \quad (2.18)$$

a square function:

$$g_\alpha = \theta(\alpha - \sigma_\alpha) - \theta(\alpha + \sigma_\alpha), \quad (2.19)$$

where θ is the Heaviside step function. Furthermore, our calculation program has been extended to use a Bragg function as angular distribution:

$$g_y = 1 \text{ for } |y| < 1 \text{ and } 1 - \sqrt{1 - y^{-2}} \text{ for } |y| > 1. \quad (2.20)$$

The whole interferometer is a combination of crystal-blades, where the calculated transmitted and reflected beams after a blade is used as incident wave on the following blade. This is shown in fig. 2.2, all possible beams after the individual beam splitters are visible, the beam between blade (3) and (4) is blocked in order to yield a one-loop interferometer. The absolute square of the interfering wave function - integrated over the beam profile, yields the total intensity, which is measured in the experiment. The phase between the two beam paths is determined from an interferogram; which is the intensity at (O) versus different values of an additional phase factor in one beam path.

⁵All the calculations are performed with the software 'IFMSIM' in chap. A.1.

⁶The calculation with only one wavelength leads to a much smaller beam divergence than the typical experimental 0.25...0.5 degree.

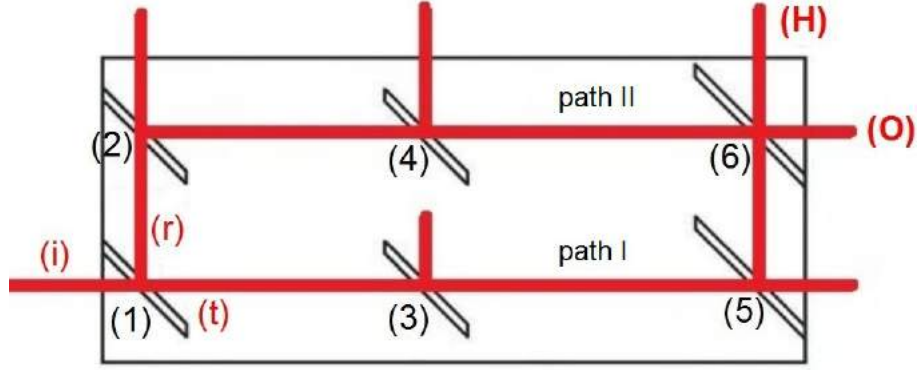


Figure 2.2.: Combination of beam splitters in Laue geometry (fig. 2.1) to yield an interferometer. (i) Incident neutron beam, (t) transmitted beam, (r) reflected beam for the first beam splitter (1). This (r) and (t) beams are used as incident beams for the following beam splitters (2)(3), and so on. (3) and (4) are used as sample blades (single-crystals). The outgoing beams of the last beam splitter (6) are denoted by (O) and (H).

Phase averaging by the beam divergence: the average phase factor from a distribution of phase shifts $P(\phi)$ within this beam divergence is given by: $\langle e^{i\phi} \rangle = \int d\phi P(\phi) e^{i\phi}$, which can be rewritten for a narrow distribution with the average phase shift $\langle \phi \rangle = \int \phi P(\phi) d\phi$ and the mean fluctuation $\langle \delta\phi^2 \rangle = \langle \phi^2 \rangle - \langle \phi \rangle^2$ as well as $\langle \phi^2 \rangle = \int \phi^2 P(\phi) d\phi$ to:

$$\langle e^{i\phi} \rangle = e^{i\langle \phi \rangle} \int d\phi P(\phi) e^{i(\phi - \langle \phi \rangle)} \approx e^{i\langle \phi \rangle - \langle \delta\phi^2 \rangle / 2} \quad (2.21)$$

where $e^{-\langle \delta\phi^2 \rangle / 2}$ describes the reduction of the visibility (or contrast). Further reasons for a reduction, besides this phase distribution within the beam divergence, are an interferometer defocusing (non-ideal geometry) or asymmetric beam-path intensities⁷.

With the interferometer and this beam, we can now calculate the phase change due to a small beam deflection in front of blade 3 (Laue phase, fig. 1.2). The measurement principle of the Laue phase is given later in chap. 2.2.2 in detail.

A calculation of the Laue phase for an interferometer with 3 mm thick blades is depicted in fig. 2.3 for a spherical and a plane wave, respectively. It shows a decrease of the phase slope for the spherical wave as compared to the plane wave, due to the phase averaging within the beam divergence. Note the Pendelloesung plateaus.

The crystal thickness of the sample blades has a large influence on the phase slope as well. The calculation for the 3 mm ideal interferometer and one with 15 mm sample blades, increases the slope around the Bragg condition, from approximately 6 to 30°/0.001" as depicted in fig. 2.4. For the thicker crystal the plateaus come closer to the center, however the contrast drops faster.

⁷Rotating a Laue crystal inside an interferometer changes the beam path's intensity as well.

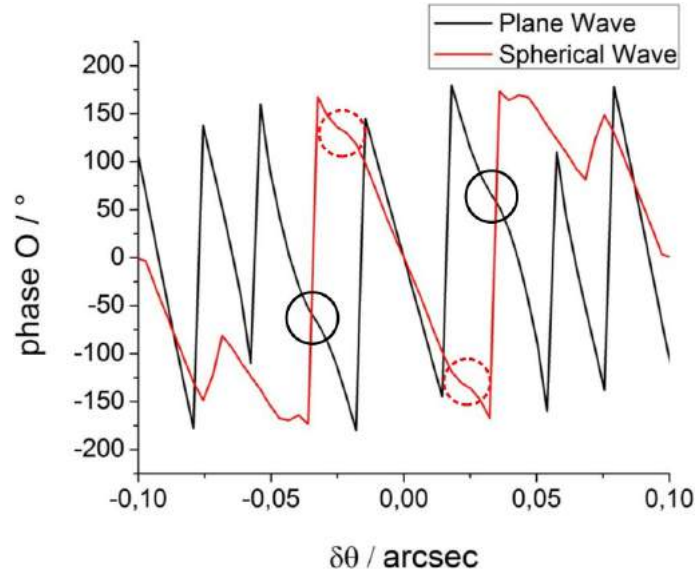


Figure 2.3.: Laue phase calculation with a plane wave and a spherical wave. The 4 circles mark the first pairs of Pendelloesung plateaus. The phase slope around $\delta\theta = 0''$ is $10^\circ/0.001''$ (plane wave) or $6^\circ/0.001''$ (spherical wave), respectively. Parameters: crystal thickness: 3 mm, $\theta_B = 45^\circ$, (220) case.

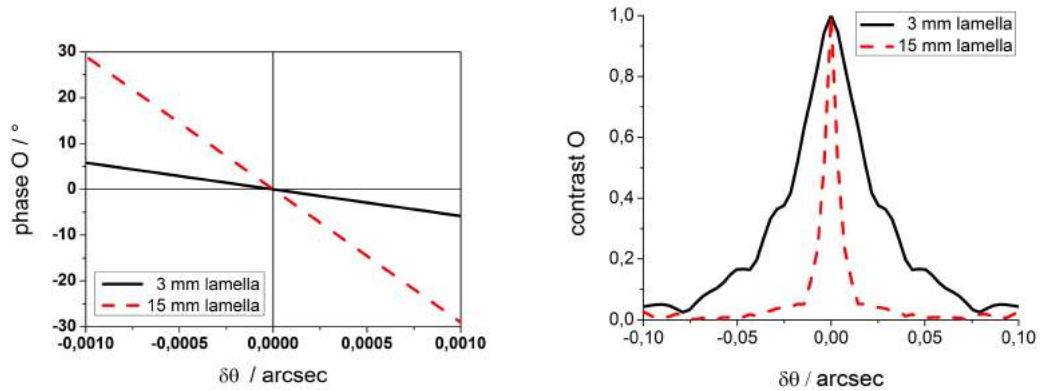


Figure 2.4.: (left) Increase of the angular sensitivity by thicker samples. (right) Decreasing width of the contrast curve with thicker samples; (220) case.

So far the phase slope was calculated for only two different sample thicknesses; in fig. 2.5 the phase slope⁸ is calculated now for several sample thicknesses (blade 3 and 4 are $3 \text{ mm} \pm 25 \mu\text{m}$). Additionally, the thickness change of only one of the sample blades (3 or 4) is given as well. The corresponding contrast decreases with the geometry error (thickness difference between blade 3 and 4) and reaches half of its value at about $20 \mu\text{m}$. Of course the contrast remains constant if both sample blades change the thickness simultaneously.

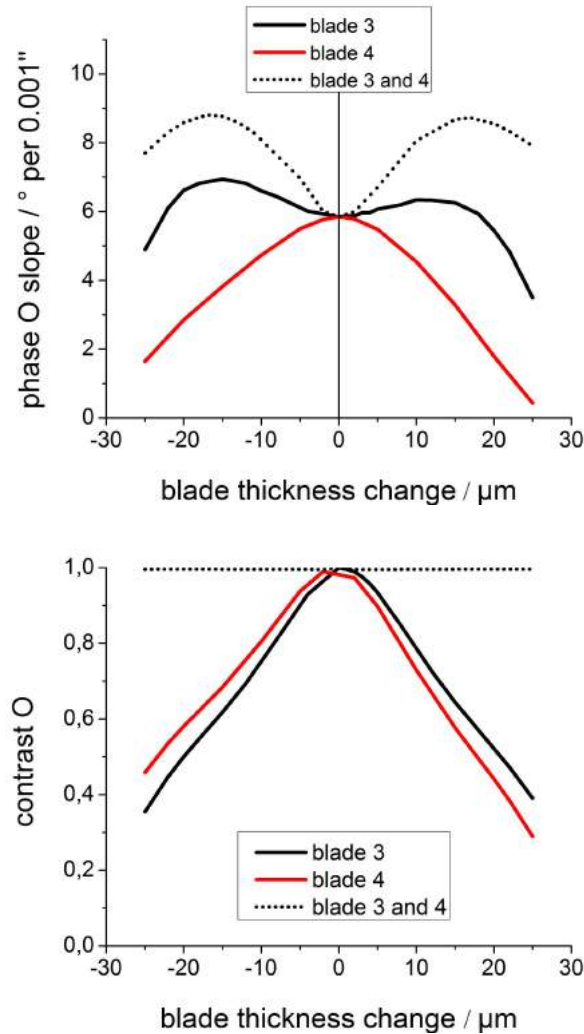


Figure 2.5.: (top) Phase slope vs. thickness deviation of blade 3 only, 4 only, or 3&4. (bottom) Corresponding contrast from (top). Parameters: ideal interferometer (IFM) with 3 mm thick blades, spherical wave, (220) case.

⁸The phases are obtained in every case from a blade 3 rotation.

2.2. Experimental

In the following an overview of the experimental components and their alignment is given. All measurements were carried out at instrument S18 at ILL Grenoble. The neutrons are produced in the high-flux reactor with a thermal power of 58.3 MW ($1.5 \cdot 10^{15}$ neutrons per second per cm^2) [20]. The beam, leaving the evacuated supermirror neutron guide H25 after the monochromator has an neutron flux of about $1.4 \cdot 10^4$ neutrons per $\text{s} \cdot \text{cm}^2$.

2.2.1. Experimental setup

An overview of the experimental setup for the Laue phase experiment is depicted in fig. 2.6. The perfect crystal Si monochromator is placed in the neutron guide behind the shutter⁹ (1), the Bragg angle of it is $(45 \pm 0.25)^\circ$ in order to extract the neutrons from the neutron guide to the experimental area. In front of the aperture are Si prisms for the (220) or (440) wavelength selection (2). The perfect crystal Si interferometer is placed in the aluminum box (3). To reduce vibrations, the interferometer and monochromator are mounted on the optical table (A), which is isolated by springs from the other part of the bench (B). To move the sample in the interferometer a robot (C) is used, the former not being connected to (A) because of the vibrations. The neutrons are counted at detectors, which are indicated by (O) and (H) in the picture. In the following the components along the beam path are described and details to their alignment are given in chap. A.5.

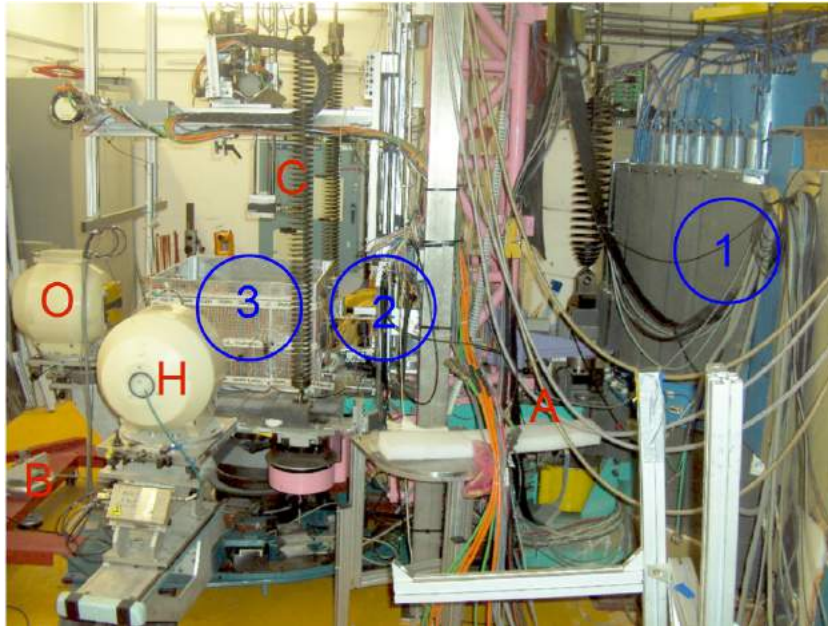


Figure 2.6.: Overview of the Laue phase experiment. (1) Monochromator/neutron guide /shutter, (2) aperture and 6 Si prisms, (3) interferometer/Al box, (A)(B) optical bench/vibration reduced table, (C) robot to move the sample, (O)(H) neutron detectors.

⁹Depending on the Bragg angle, two out of 10 lead blocks are lifted by a compressed air system.

Monochromator: the monochromator is placed in the neutron guide. This Si crystal reflects neutrons obeying the Bragg condition for a certain wavelength/direction distribution to our experiment. It is mounted on a rotatable slide to choose the Bragg peak and adjust the beam position (fig. 2.7).

Wavelength selection: the beam then passes six 140° Si prisms for a separation of the higher order reflections (fig. 2.7)¹⁰, in order to compare the Laue phase at different wavelengths. Without the prisms the intensity is higher and the peak is asymmetric due to the peak overlap. The measured intensity ratio of the peaks (220):(440):(660) are 1:0.35:0.04. The separation with the prisms of the (220) and (440) Bragg peak amounts to $13''$, for the (440) and (660) Bragg peak $2.34''$. It can be determined by performing a rocking curve, where the rocking angle describes the rotation of the IFM in the x-y plane relative to the incident beam (fig. 2.7, 2.11). The separation values can be calculated with eq. 2.22 [29], where $\beta_i = 140^\circ$, λ is the wavelength, $N = 4.9939669 \cdot 10^{22} \text{ cm}^{-3}$ the number of nuclei per unit volume for Si and $b_N = 4.1507(2) \text{ fm}$ its nuclear scattering length.

$$\delta(\lambda) = \lambda^2 \sum_{i=1}^6 \frac{N b_N}{\pi} \tan \frac{\beta_i}{2} \quad (2.22)$$

The results are: $12.56''$ (220)-(440), $2.26''$ (440)-(660) and $0.81''$ (660)-(880).

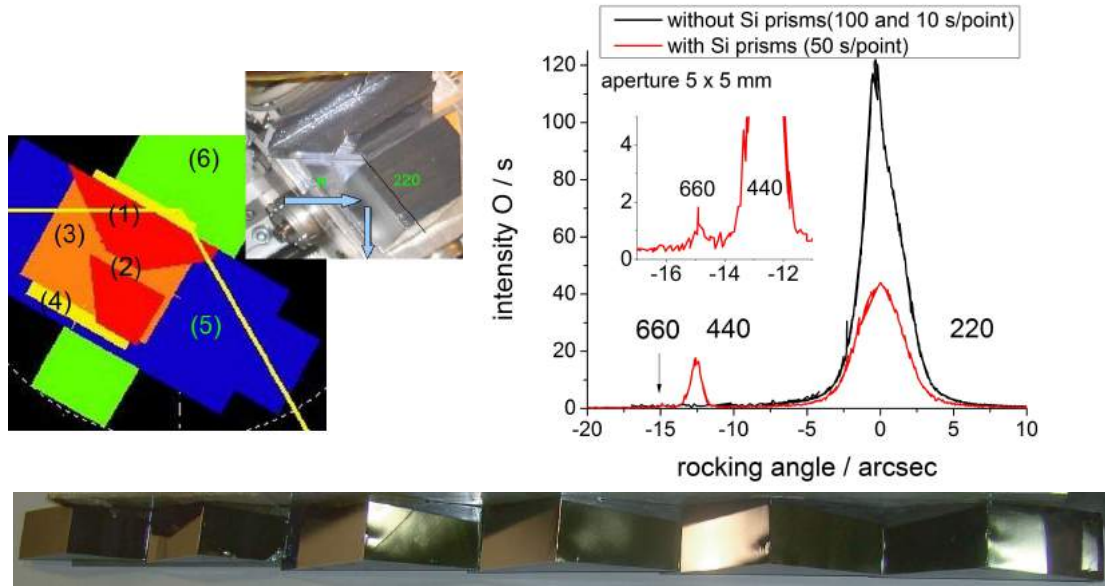


Figure 2.7.: (left) Sketch of the neutron beam (1), monochromator crystal (2), and slides to adjust its orientation (3)...(6). (right) Rocking curve with and without Si prisms. The (440) is $13''$ separated from the (220) Bragg peak. The phase measurements will be performed exactly at each peak maximum. (bottom) The 6 Si prisms are placed after the monochromator.

¹⁰For the separation of the (220) and (440) Bragg peak, 2 prisms would be sufficient.

The aperture: is mounted after the prisms, it is made of cadmium¹¹. The rectangular beam window can be chosen up to 26 x 26 mm², for our experiment we use 5 x 5 mm² to ensure that the beam fits through all components with sufficient intensity during the measurements. Typical value of the counted neutrons are visible in fig. 2.7, e.g. for the (220) Bragg peak at the interferometer output O: 160 neutrons per s·cm².

Interferometer with sample

The six blade Si perfect-crystal interferometer is described in chap. A.4. Its size is very large (length: 23.5 cm, width: 10 cm), so that it is possible to insert bulky components such as prisms and beam stops (fig. 2.8). It is placed on 10...20 layers of papers on a 2 kg flat Al disk with 40 cm in diameter (B). **Piezo:** the disk can be rotated by a piezo-electric device ($\pm 0.18''$, Burleigh Instruments: Inchworm Motor IW-701). Drifts of up to 4''/hour can occur if the piezo control stays activated, therefore the rocking position (chap. 2.4.5) requires to be continuously checked and the control system needs to be deactivated after read out¹².

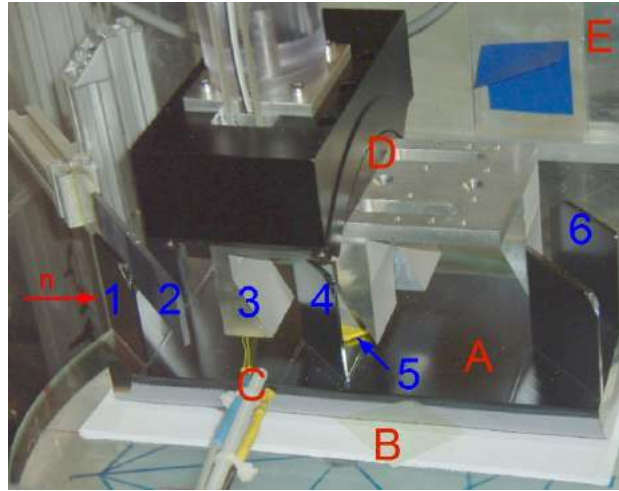


Figure 2.8.: Experimental setup. (A) Interferometer (23.5 x 10 cm²), (B) IFM support, (C) temperature sensor, (D) rotatable prism holding device, (E) Al box, (1) interferometer blade 1 (beam splitter), (2) phase shifter: Si 3 mm thick, (3) Al prism for beam deflection in front of interferometer blade 3 (4), Cd for beam absorption (5), (6) interferometer blade 6 (beam recombination).

Behind the aperture, the neutron beam (n) enters the Al box and is split in two beams at interferometer blade 1 (1). **Phase shifter:** a $D = 3$ mm thick Si phase shifter (2) is used to obtain the interference pattern. The tab. 2.1 lists the measured phase shifter thicknesses at the positions depicted in fig. 2.9. The relation of the phase shifter *angle*¹³ and the thickness difference in the two beams is given in the following eq. [2]:

$$\Delta D(\text{angle})/D = \left(\frac{1}{\cos \theta_B + \text{angle}} - \frac{1}{\cos \theta_B - \text{angle}} \right) \quad (2.23)$$

¹¹Note that Cd is toxic (gloves). It has a high absorption cross section for thermal neutrons.

¹²Press 'stop' in the motor section of the S18 control program after the piezo selection, chap. A.3.

¹³The angle of the phase shifter, when it is parallel to the interferometer lamella, is subtracted.

A typical interferogram consists of about 24 points, separated by 0.06° (220) and 0.12° (440) steps, respectively. The measurement time is about 30 s/point. The intensity I is normalized to the O+H detector signal; afterwards, a least squares fit (eq. 2.24) gives the parameters A (intensity offset), B (amplitude), $C \cdot \Delta D$ (known phase from phase shifter rotation) and ϕ (unknown phase).

$$I(\Delta D) = A + B \cdot \sin(C \cdot \Delta D + \phi) \quad (2.24)$$

The fringe visibility V follows from the largest (I_{max}) and smallest (I_{min}) measured intensity values of the interferogram:

$$V = \frac{I_{min} - I_{max}}{I_{min} + I_{max}} \quad (2.25)$$

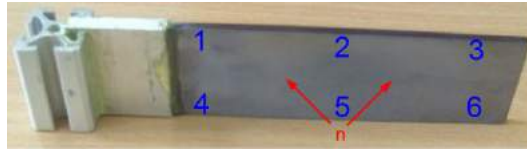


Figure 2.9.: Phase shifter made of Si ($10.2 \times 3 \times 0.3 \text{ cm}^3$). (1)...(6) Positions of the phase shifter where the thickness measurements were performed (see tab. 2.1). After the interferometer blade 1, the two neutron beams (n) pass through the phase shifter, approximately at the indicated position.

Table 2.1.: Measured phase shifter thicknesses D at the positions shown in fig. 2.9 (with a micrometer caliper).

position:	1	2	3
D / mm:	3.033(3)	3.016(1)	2.991(2)
position:	4	5	6
D / mm:	3.034(3)	2.991(3)	2.936(1)

AlMgSi0.5 prisms: are used due to their excellent homogeneity for a beam deflection in front of interferometer blade 3. Two pairs of prisms are used to avoid a defocusing of the interferometer and to compensate the phase shift in the other beam path. Both prism pairs are mounted on a rotatable prism holding device. The correlation of this beam deflection with the rotation angle α of the prisms is [5]:

$$\delta\theta = \delta \cdot \sin \alpha \quad (2.26)$$

$$\delta = 2(1 - n) \frac{\sin \beta}{\cos \beta + \cos 2\epsilon} \quad (2.27)$$

$$n = 1 - \frac{\lambda^2 N b_N}{2\pi}$$

The angle β of the prisms is 25° and ϵ , the deviation from the symmetric prism mounting, is 12.5° (fig. 2.11). The alignment of several prism angles is discussed in chap. 2.4.6. λ is the wavelength and $N b_N = 2.08 \cdot 10^{10} \text{ cm}^{-2}$, the scattering length density [2].

In principle three interferometer loops are selectable in this interferometer type, which are shown in fig. 2.2. A **beam stop** made of cadmium is placed between the interferometer's blades (3) and (4), to use the big loop only. The beam is recombined at the interferometer blade 6, the two exiting beams O and H are counted in the detectors (O,H).

Detectors

The neutrons are absorbed in the detector gas and produce an electrical signal. The used ^3He detectors are cylindrical with a diameter of 5 cm and a length of 10 cm and operate with a voltage of about 1.5 kV and an efficiency of $\approx 98\%$ (XERAM).

2.2.2. Measurement principle

Before we discuss the Laue phase measurement in the next chapter, its measurement principle will be presented here in detail. In general, a phase within an interferometer is measured by recording the output intensity in the O detector versus the rotation angle of an auxiliary phase shifter. A Mach-Zehnder type interferometer together with the sinusoidal interferogram is depicted in fig. 2.10(a), 2.10(b). The principle of measuring the Laue phase is illustrated in fig. 2.10(c), 2.10(d) with a 'rotating' sample, where the rotation angle is denoted by $\delta\theta$. The sample is a perfect Si crystal like the interferometer blades. The additional blade in the second beam compensates for the refractive phase of the sample at $\delta\theta = 0''$. For each $\delta\theta$ a complete interferogram is taken. The phase change of the interferogram due to the small sample rotation is the 'Laue phase'. The tilt of the interferometer versus the monochromator (ρ -axis angle) is adjusted in order to yield the rocking curve with the smallest width (chap. A.5).

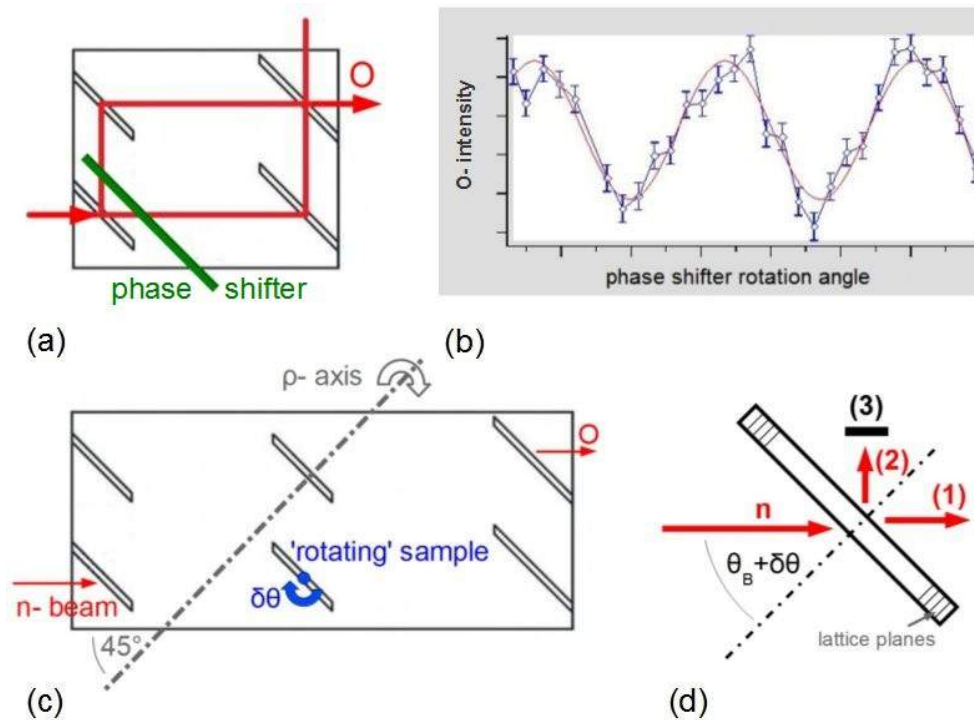


Figure 2.10.: (a) Sketch of a Mach-Zehnder interferometer with a phase shifter intersecting the two beam paths. (b) Typical interferogram in the output O: the intensity is recorded versus the phase shifter rotation. The phase and fringe visibility is derived from this sinusoidal intensity modulation. (c) Neutron interferometer with rotating sample (the phase shifter is here not shown). (d) Top view of the sample with the $\delta\theta$ angle: (1) transmitted beam, (2) diffracted beam, (3) beam stop.

As the rotation of the IFM blade 3 is impossible, we manage a rotation of the beam instead by a pair of aluminum prisms. A scheme of the experiment is given in fig. 2.11 and a photography is provided in fig. 2.8. There, the second prism avoids a defocusing of the interferometer and the second pair of prisms compensates the phase shift in the other beam path. This beam deflection is controlled via a rotation α around the beam axis of the prisms. The correlation between the beam deflection and the rotation angle α of the prisms, as well as the used wavelength is given in eq. 2.26. In our upgraded setup, a range of $\alpha = \pm 15^\circ$, is experimentally accessible, which accounts for the (220) wavelength to $\delta\theta = \pm 0.06$ arcsec and ± 0.015 arcsec for the (440) wavelength. Compared to previous measurements [4], a new prism holding device was constructed, in order to realize this larger beam deflections¹⁴. Due to unavoidable intrinsic interferometer phase drifts, a commonly used 'IN-OUT' measurement process is used to obtain the phase values. IN and OUT denote two different rotation angles of the prisms within the beam. The phase at an IN position $\delta\theta$ is always subtracted by the phase value at $\delta\theta=0''$ (OUT position) for each phase shifter position in an interferogram.

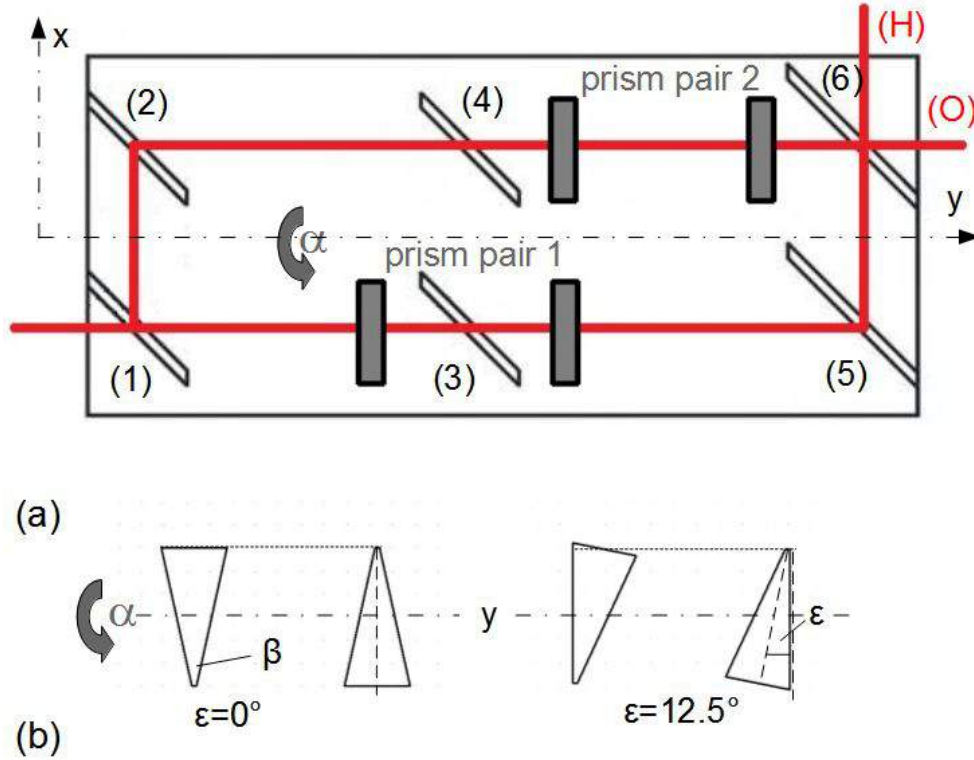


Figure 2.11.: (a) Top view of the experiment (the phase shifter is here not shown). The incident wave is split at blade (1) and passes through the sample blades (3), (4) and prisms - which rotate around the y -axis (α). After recombination in blade (6), the interferogram in the transmitted beam (O) is recorded. (b) Prism side view and mounting angle $\epsilon = 12.5^\circ$ ($\beta = 25^\circ$).

¹⁴Note that the sample volume is slightly different, where the beam passes due to the beam deflection.

2.3. Measurements and Calculations

In the last chapter we discussed the setup and the measurement principle, now the results of our measurement at ILL are presented. As mentioned in the introduction, this study follows the previous measurements in [4] and [30], with the aim to improve the accuracy of the phase measurement and extend the angular range $\delta\theta$ of our sample rotation in order to extract fundamental quantities, discussed later in chap. 2.4.8. Therefore, as the main experimental improvement, an aluminum box for temperature stabilization of the interferometer has been installed. Details together with its active heating and cooling possibilities are described in chap. A.5. During these measurements we paid attention to further alignment parameters, like the rocking angle, ρ -axis and prism mounting; their influences on the Laue phase are investigated later (chap. 2.4). The planned comparison measurement at NIST (National Institute of Standards and Technology), with a different setup was not possible due to limited time; in particular a mosaic crystal monochromator is available there. Unfortunately, a lot of time consuming interferograms can not be used, due to visibility problems with large interferometers.

The measurements are compared with numerical calculations as described in chap. 2.1.2. The parameters in our calculation program IFMSIM are:

- Bragg monochromator curve with Darwin width=1 and
- the IFM geometries: 'real I' and 'ideal'; its exact values are listed in chap. A.4.

The use of the Bragg monochromator curve is a main improvement compared to the calculations in [4], because it describes the physical monochromator function. Its influence will be discussed in chap. 2.4.3.

In order to compare the Laue phase at two wavelengths, two Bragg peaks from the silicon monochromator have been chosen: (220) and (440).

2.3.1. (220) case

Fig. 2.12 shows the Laue phase, contrast and intensity for the (220) Bragg peak; each measurement-point represents an average value of about 10 single measurements. This experimental values were taken with the setup alignment from March 2013, where the visibility conditions were the best and therefore the Laue phase error bars are minimized. In the (220) case, the wavelength is about 2.72 \AA . The neutron beam deflection is performed in front of blade 3 with Al prisms and its beam deflection range is about $\pm 0.06''$. For this deflection, a prism rotation angle of $\alpha = \pm 14^\circ$ is necessary at this wavelength. This range is larger than in [4], where $\delta\theta = \pm 0.04''$ ($\alpha = \pm 10^\circ$). This is important in order to study the influences of several parameters on the Laue phase at a wide $\delta\theta$ range, in particular for higher order reflections. The beam deflection depends on λ^2 c.f. eq. 2.27.

Phase:

Note that the Laue phase formula in eq. 2.13 describes the Laue phase with only one plane wave, whereas our calculations consider a coherent superposition of many plane waves (spherical wave). Important for the understanding of the phase and contrast behavior is the averaging over all of this plane-wave components. Therefore, the phase

slope becomes about 1/3 smaller than for a single plane wave; however, it still constitutes a very fascinating steep phase slope. In particular, the slope of the phase curve in the vicinity of the exact Bragg condition, amounts to $5.5^\circ/0.001$ arcsec and is well in agreement with the calculation, fig. 2.12 (top). The slope calculated with a plane wave would be steeper with $8^\circ/0.001$ arcsec. Two non-linearities in the phase curve ('Pendelloesung plateaus') can be identified at each side in the vicinity of the Bragg position. Their $\delta\theta$ positions are: 1st : $\pm(0.02 \dots 0.03)''$ and 2nd : $\pm(0.04 \dots 0.05)''$ (tab. 2.11). These structures are related to oscillations resulting from the interference of two internal wave fields with slightly different wave vectors [31]. They appear exactly at the minima of the transmitted intensity and are described by the arcus tangents in eq. 2.13. The change of the phase will be evaluated at this positions, there the sensitivity to fundamental parameters like the scattering length is enhanced. The influence of several other parameters, like the exact interferometer geometry is discussed in chap. 2.4. Important is the result, how accurate the Laue phase can be measured. The error bars of the phase values are about $\pm 9^\circ$ for the first plateaus and $\pm 15^\circ$ for the seconds and will be compared later with the influence of several parameters. These values are obtained from the difference $\text{IN}(\delta\theta)$ minus $\text{OUT}(\delta\theta=0'')$ according to the measurement procedure, in order to avoid arbitrary phase drifts. Note that the phase accuracy is obtained from an average of ≈ 10 single measurements.

Contrast:

Besides the phase, the fringe visibility (contrast) of an interferogram (fig. 2.10) is considered as well. The diminishing of the interference pattern with increasing $\delta\theta$ is shown in fig. 2.12 (middle). Due to the low contrast, measurements at $\delta\theta > 0.02$ arcsec become increasingly challenging. The contrast reduction is mainly caused by a distinct phase distribution within the divergence of the incoming beam. Asymmetric beam-path intensities reduce the fringe visibility as well [2]:

$$V \propto \frac{\sqrt{I_{\text{beamI}} I_{\text{beamII}}}}{I_{\text{beamI}} + I_{\text{beamII}}} \quad (2.28)$$

This asymmetry results from the blade 3 rotation during the measurement, the beam path I and II are marked in fig. 2.2. The measured curve results from a relative measurement of $\text{IN}(\delta\theta) / \text{OUT}(\delta\theta=0'')$, therefore the contrast is 1 at $\delta\theta=0''$ in fig. 2.12 (middle). The average of all OUT measurements is 14% (absolute contrast at O)¹⁵. This constitutes the challenging conditions for large neutron interferometry. For comparison: smaller IFMs (length ≈ 15 cm) usually work at visibility values $>60\%$. The Pendelloesung plateaus in the contrast curve are also visible, their positions are the same as for the phase curve.

Intensity:

The measured intensity in fig. 2.12 (bottom) results as well from the $\text{IN}(\delta\theta) / \text{OUT}(\delta\theta=0'')$ measurement procedure. It shows a marked decrease near Bragg due to a diffracted beam which exits the sample as well. Interesting are the intensity oscillations, where the minima position fits with the Pendelloesung plateaus of the phase and contrast. This can be clearly seen in both the measured and calculated data and acknowledges the reliability of the calculation program IFMSIM.

¹⁵Maximal 20%, the best observed value during all our measurements is 35%.

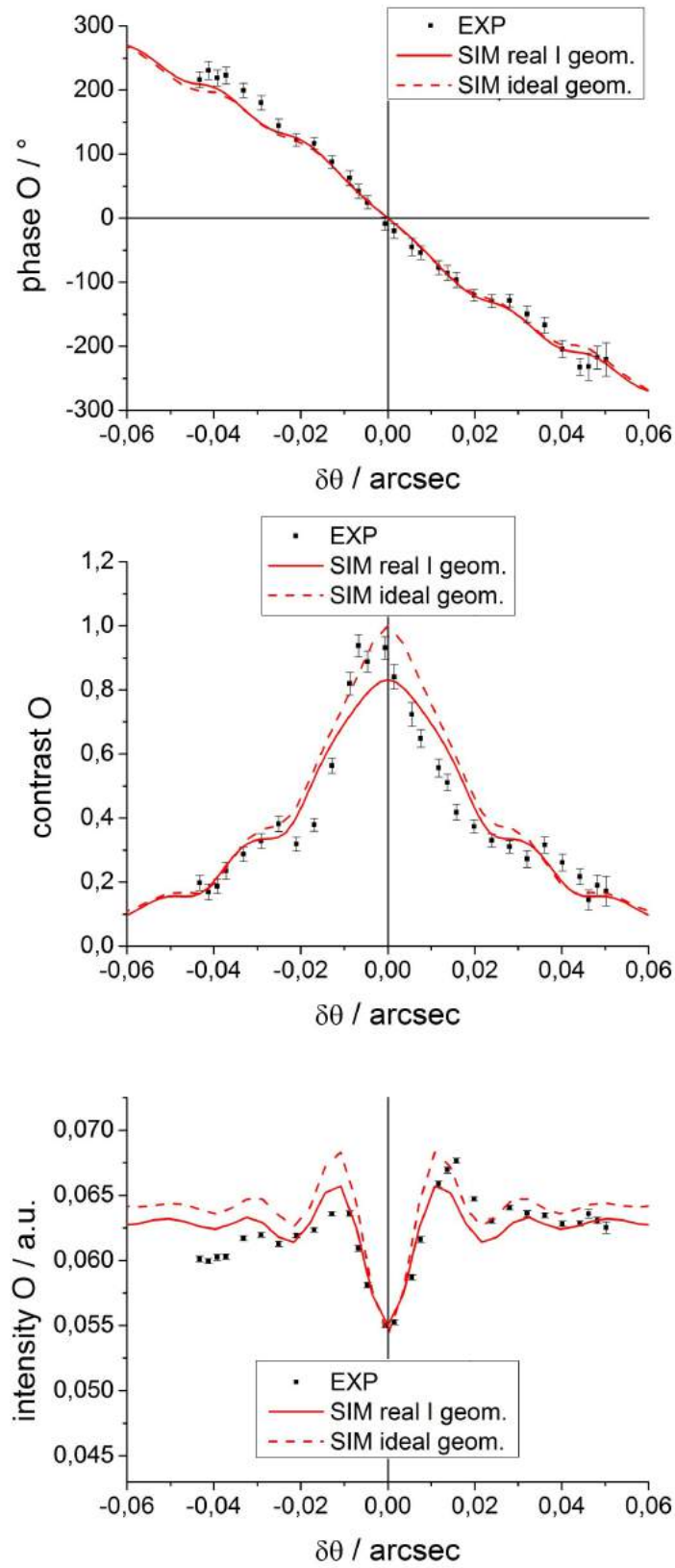


Figure 2.12.: Measured (EXP) and calculated (SIM) Laue phase (top), contrast (middle), and intensity (bottom) of the (220) O beam, EXP shifted by $\delta\theta=0.0035''$.

The measured values of the phase, contrast, intensity are shifted all together in $\delta\theta$ to be centered around $\delta\theta = 0''$, this shift in the diagrams is discussed below.

2.3.2. (440) case

Fig. 2.14 shows the Laue phase, contrast and intensity for the (440) Bragg peak, the wavelength is about 1.34 Å. The measurements were taken with different setup alignments from July 2012 and August 2012, due to limited measurement time. Each point in the plot represents an average value of about 5 single measurements. The realizable $\delta\theta$ range is smaller, due to the wavelength dependence in eq. 2.26. It amounts to $\pm 0.015''$ ($\alpha = \pm 14^\circ$)¹⁶. Only one pair of Pendelloesung plateaus is within this range, for higher reflections only the slope of the Laue phase can be measured with this prism configuration. The $\delta\theta$ positions of the plateaus for the phase and contrast are the same, and fit with the minima of the intensity. Their $\delta\theta$ values are about half of the (220) case: 1st : $\pm(0.01 \dots 0.015)''$ and the 2nd would be at $\pm(0.02 \dots 0.025)''$. The measurement and the calculations are again in good agreement.

Phase: the slope of the phase curve in fig. 2.14 (top) near the exact Bragg condition amounts to $11.5^\circ/0.001$ arcsec. It is steeper (about the double) than in the (220) case, hence it constitutes an extremely sensitive phase versus angle correlation [15]. The slope is now well in agreement with the calculation, and improves previous measurements [4] (tab. 2.2). There the mismatch is suspected due to a misalignment of the rocking angle. This is confirmed by our measurements in chap. 2.4.5. The feasible measurement accuracy of the Laue phase for this wavelength is represented by the error bars in the first plateaus, which is about $\pm 12^\circ$. **Contrast:** the relative fringe visibility is shown in fig. 2.14 (middle), the average of all OUT measurements is 16% (absolute contrast). As in the (220) case, the visibility decreases fast with $\delta\theta$ (phase mismatch). The different size of the error bars stems from different numbers of individual measurements per point. **Intensity:** the intensity oscillation around $\delta\theta = 0''$, with its minima at the Pendelloesung plateaus, like in the (220) case is again visible in fig. 2.14 (bottom).

2.3.3. Measured $\delta\theta$ -shift

The measured values in all diagrams are centered around the $\delta\theta = 0''$ position¹⁷; the calculated values are not shifted. This shift is illustrated in fig. 2.13 for the intensity curve. Such a $\delta\theta$ -shift was already observed in [4], [30]; several reasons are discussed like:

- if the lattice planes would not be orthogonal to the lamella surface,
- imperfect interferometer geometry,
- crystal strains, and
- the Coriolis forces - which was favored as explanation¹⁸.

¹⁶It is wider than in [4]: $\pm 0.01''$ ($\alpha = \pm 10^\circ$).

¹⁷The phase offset at $\delta\theta = 0''$ for the $\delta\theta = 0.0035''$ shift is 33° .

¹⁸In future studies this force can be implemented in IFMSIM.

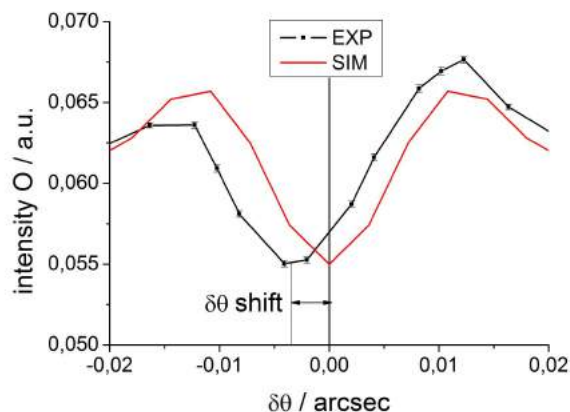


Figure 2.13.: Illustration of the $\delta\theta$ -shift. The zero position of the prisms is aligned with a water level, however the measured values are not centered at $\delta\theta = 0''$.

In our study an additional small contribution to this $\delta\theta$ -shift has been found in chap. 2.4.5, caused by a deviation from the exact rocking angle in combination with the non-ideal interferometer geometry¹⁹. Furthermore, IFMSIM has been extended with the possibility to calculate with prisms; different alignment errors which can rise such a $\delta\theta$ -shift will be investigated later in chap. 2.4.6. We found that a shift would be possibly due to a relative rotation between first and second prism, however this should not be the case in our setup.

The shift values from our measurement as well as the old ones are summarized in tab. 2.2. Additional to the measured Laue phase and contrast shifts we listed the intensity shifts as well. Within its maximal error limits, the shifts are approximately in agreement with the previous measurement in [4]. The (440) contrast shift value is about the half of (220). The contrast maximum can be influenced by the different rocking position, which is indicated by the smaller phase slope value in [4]. The values are obtained with a Gauss-fit around the maximum in the contrast and intensity curve. The zero position of the prisms defines $\delta\theta = 0''$ and it is aligned with a water level. The maximal prism rotation error is about $\alpha = 0.1^\circ$, which is $0.0004''$ (220) / $0.0001''$ (440).

Table 2.2.: Measured contrast (contr.), intensity (int.), and phase shift as well as the phase slope. A different slope value, between the two (440) measurements, indicate a different rocking position.

measurement	contr. shift / ''	int. shift / ''	phase shift / ''	slope / ° per 0.001''
(220)	-0.006(3)	-0.0035(20)	+0.002(4)	5.5
(220) [4]	-0.0080(4)	-	-0.008	6.0
(440)	-0.0025(30)	+0.0035(10)	+0.0015(40)	11.5
(440) [4]	-0.0045(3)	-	-0.0045	8.5

¹⁹About $\delta\theta = 0.001''$ up to $0.003''$, for a rocking angle deviation of $0.18''$ to $0.9''$ (real I geometry, (220)).

Summary

Summarizing the measurement at the two Bragg peaks, the smaller wavelength yields a higher phase slope; however, the achievable beam deflection range is reduced. For the used large neutron interferometer, the absolute contrast average over all measurements at $\delta\theta = 0''$ was about 15%, this is a very challenging condition. However, the expected large slope of phase shift per misset angle as well as the Pendellosung plateaus are clearly evident in the data. The resulting measured relationships and the calculations are in good agreement. However, whether the accuracy of the measurements is sufficient will be discussed in chap. 2.4.8, in order to determine parameters like the scattering length. For a measurement with higher order reflections, a better rocking angle rotation device and a higher angular stability of the whole setup is necessary, because the FWHM of (660) is about $0.5''$ and for (880) it is just $0.25''$, while the rocking angle accuracy is $0.18''$. Deviations from the exact rocking position will change the phase strongly, see chap. 2.4.5.

In the next chapters, the influence of varying different parameters will be discussed and the change of the Laue phase will be evaluated, particularly at the plateau positions. Additionally, another method to measure the phase, will be introduced in chap. 2.5.

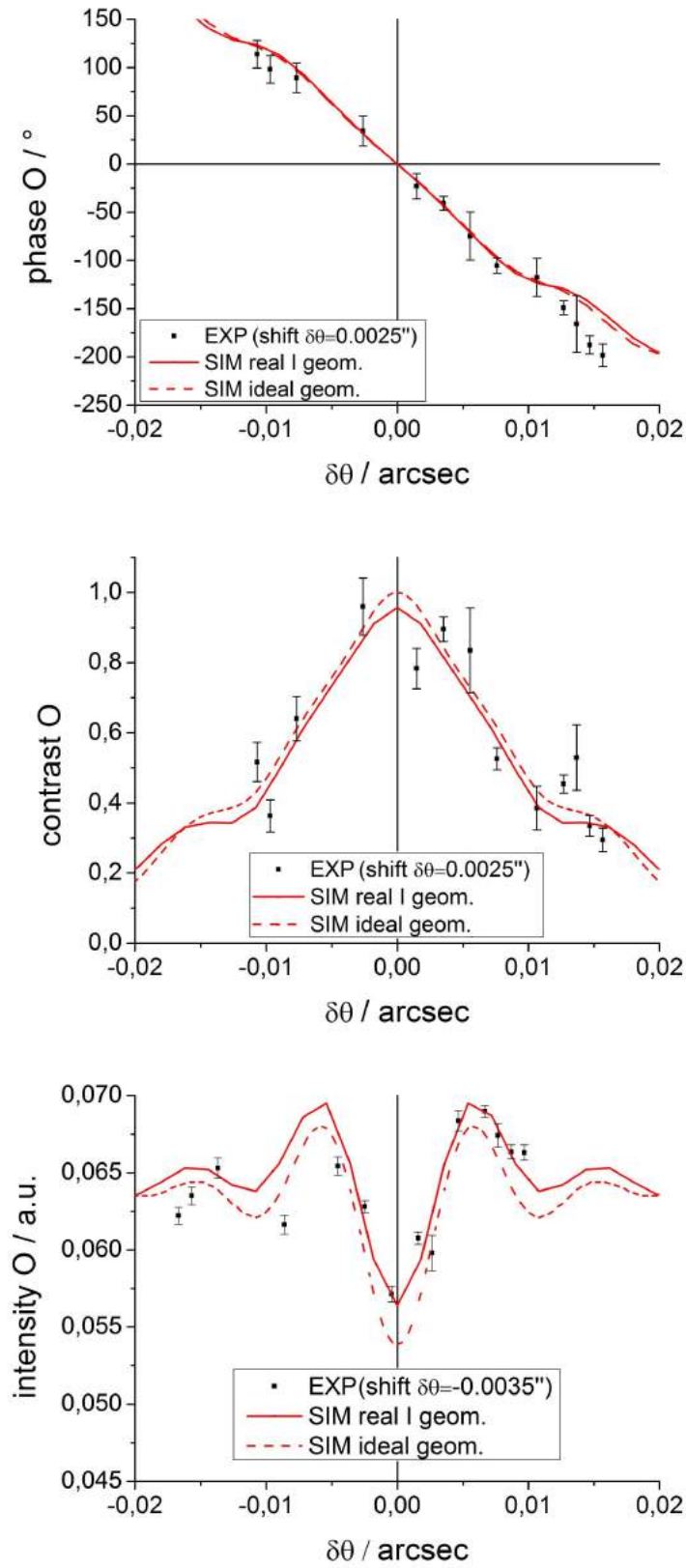


Figure 2.14.: Measured and calculated Laue phase (top), contrast (middle), and intensity (bottom) of the (440) O beam.

2.4. Systematic effects on the Laue phase

In the previous chapter the accuracy of the Laue phase measurement of our setup has been demonstrated. Here we want to figure out which parameter has an influence on the Laue phase and compare it with our measurement accuracy. Such parameters addresses e.g. the experimental alignment of the components, the used interferometer geometry, wavelength etc. Possible phase changes are evaluated at specific $\delta\theta$ -values (where the Pendelloesung plateaus are located) and the phase slope is obtained in the vicinity of $\delta\theta = 0''$. The contrast and intensity behavior is taken into account as well.

Especially for a reliable measurement of fundamental quantities the behavior of the system has to be known; therefore, in particular the following parameters are investigated in the next sections in detail:

- geometry (e.g. blade thickness)
- temperature
- monochromator function
- beam divergence and ρ -axis angle (fig. 2.10)
- rocking position
- Al prisms
- wavelength
- fundamental parameters (e.g. scattering length b_{ne})

Another parameter is the roll of the whole optical bench, its rotation axis is parallel to the interferometer's length direction²⁰. During all measurements the roll of the optical bench is adjusted within $0.001 \dots 0.01^\circ$ to the zero position²¹. This roll simply changes the situation in the gravity field, the arising COW phase²² is subtracted due to the IN-OUT measurement procedure (chap. 2.2.2).

Fig. 2.15 shows measurements of the Laue phase and contrast, at a roll of 0.063° ²³ and 0° . The phase and contrast have indeed the same behavior for this two roll angles. Every point at 0.063° represents an average value of about 5 to 6 single measurements. The values at 0° are taken from chap. 2.3.

²⁰Note that the roll of the bench does not change the rocking curve (the monochromator is tilted as well).

²¹This zero position is the horizontal bench position, approximately orientated with a water level.

²²A roll of 0.063° yields a COW phase of: 67° (220), 34° (440), 22° (660) [14].

²³Note that this roll is negligible as compared to the zero point of the Al prisms (chap. 2.4.6).

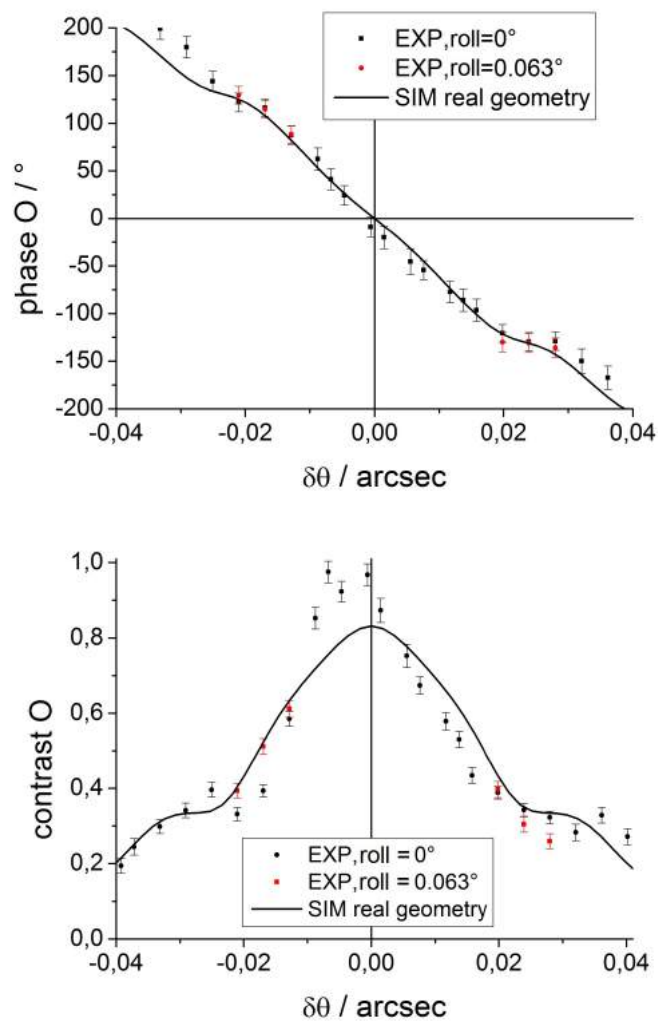


Figure 2.15.: Laue phase (top) and contrast (bottom) at different roll of the optical bench. The EXP values are shifted by $\delta\theta = 0.035''$ according to chap. 2.3.

2.4.1. Interferometer geometry

In general, the design of the interferometer is based upon the characteristics of the used sample, which results in the use of this large IFM. With 'interferometer geometry' we basically mean the blade thicknesses and the blade distances. The detailed geometry in the μm -range depends on the preparation possibilities. Therefore, the IFM in the experiment has a geometry, which deviates slightly from the intended ideal values. The geometry can be measured and will be denoted as 'real'. Hence, the geometry can be different for the particular position where the beam traverses the interferometer blades. This non-ideal geometry constitutes a complex system, creating a special phase distribution within the beam. The Laue phase, as an average of this distribution is studied in this chapter as a function of the blade thickness. This is important for the question, how accurate the geometry has to be known, to measure fundamental parameters at a prescribed precision. In general, an ideal interferometer includes identical IFM blade thicknesses and equal distances between the blades, however the sample blades 3 and 4 are allowed to have a different thickness. This would lead to a change in the slope of the Laue phase according to eq. 2.16. To enhance the angular sensitivity of the Laue phase, our new interferometer described in chap. 3 is prepared with 15 mm thick sample blades. The influence of the geometry on further parameters will be investigated separately in the subsequent chapters. The geometry of the prisms is discussed in chap. 2.4.6.

Blade shapes

First we take a look at the thickness measurements over a certain region on each blade from tab. A.3. The deviation of the thickness values from their average values are drawn in fig. 2.16, for all lamellas. It reveals a wedge shape with a thinner blade at the IFM basis. The deviation maxima within the scanned area and its calculated angles are listed in tab. 2.3. Note the very small wedge angle difference of blade 3 and 4. Note, that the Laue phase is measured in this work at blade 3 and in [30] at blade 4. Unfortunately,

Table 2.3.: IFM blade wedge shapes in \dot{x} and \dot{z} direction within $2.5 \times 2.5 \text{ cm}^2$, cf. fig.2.16.

blade no.	$\dot{x} / \mu\text{m}$	\dot{x} angle / $^\circ$	$\dot{z} / \mu\text{m}$	\dot{z} angle / $^\circ$
1	1	0.0023	6	0.0138
2	1	0.0023	0.5	0.0011
3	0	0	2	0.0046
4	1	0.0023	1.5	0.0034
5	2.5	0.0057	3	0.0069
6	0.5	0.0011	6	0.0138

the calculation program is limited by parallel blade surfaces so far (no wedge shapes of crystalline materials are possible). However, an estimation of its influence can be done by inserting a non-crystalline Si wedge with an angle of 0.0138° . This will lead to a very small beam deviation of only $0.0012''$ (eq. 2.22). On the other hand, we will now estimate a possible influence of such a geometry deviation only by blade thickness changes.

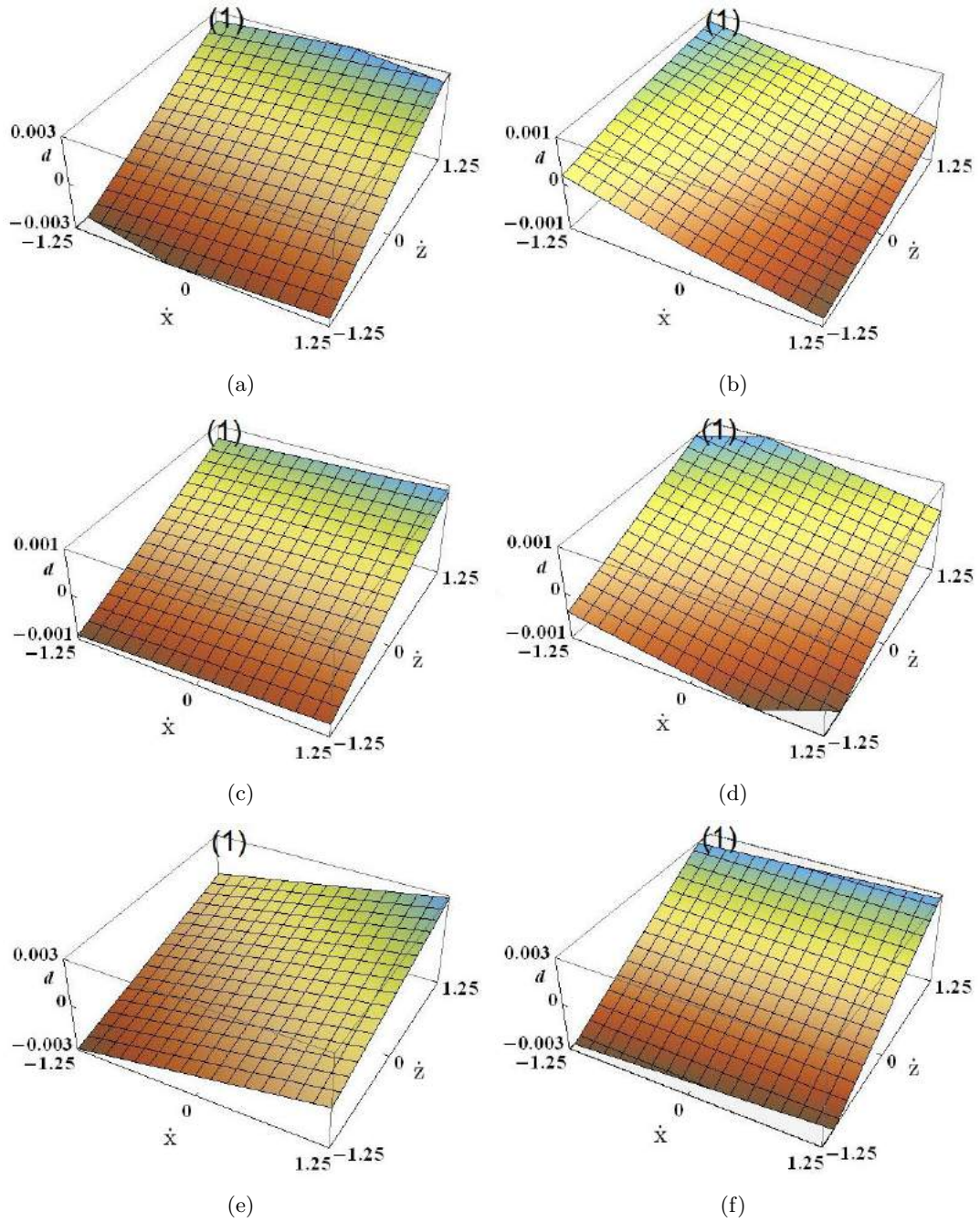


Figure 2.16.: Interferometer blade thickness (minus average value) d . The blade no. 1...6 (a)...(f) and coordinates are indicated in fig. 2.17. The wedge values are listed in tab. 2.3. Note that the \dot{x} and \dot{z} axis are in cm, while the difference d is in mm. Position (1): $\dot{x}=-1.25$ cm, $\dot{z}=1.25$ cm etc.

Thickness change of all interferometer blades

Here we will calculate in general the influence of changing the IFM blade thicknesses. Its effect on the Laue phase will be evaluated at the Pendelloesung plateaus. We focus on the Laue phase versus the blade 3 rotation. The lamella thicknesses will be changed from $D=3$ mm, by adding an additional contribution ΔD separately to each blade. This is illustrated in fig. 2.17 for blade 1 only; the thickness change is in the range of $\Delta D = 0.1$ to $10 \mu\text{m}$ (chosen according to the thickness measurement in tab. A.3).

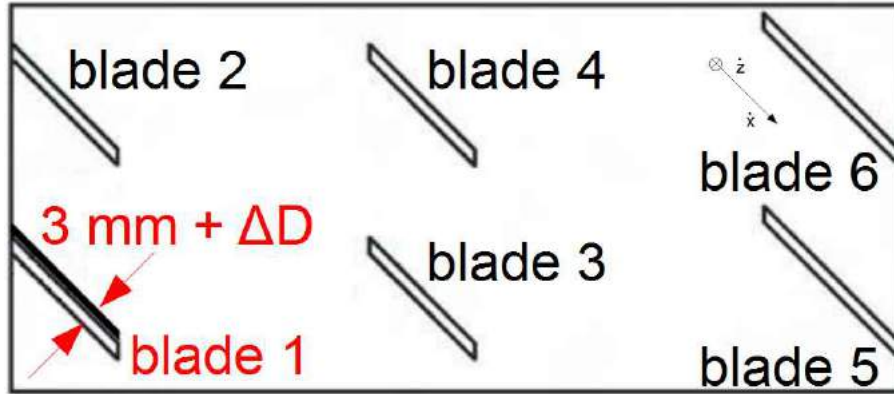


Figure 2.17.: The interferometer blade thicknesses are 3 mm, only blade 1 is thicker: $\Delta D = 0.1 \dots 10 \mu\text{m}$. The resulting Laue phase with this geometry is calculated in fig. 2.18.

Laue phase: in fig. 2.18 the Laue phase is shown for the ideal interferometer, where all blade thicknesses are 3 mm. The modified Laue phase due to the thickness change of each blade is drawn as well. The phase is characterized by its offset at $\delta\theta = 0''$, slope and position of the plateaus. The offset does not change with the thickness variation in blade 1 and 6, however a thickness change of the blades in the left beam path (blade 3, 5) shifts the offset in positive - right path (blade 2, 4) in negative direction. This offset is simply a result of additional material in one beam path, described by eq. 1.1. Due to our IN-OUT measurement method this offset is subtracted in the experiment. The phase slope results from averaging a distinct phase distribution within the beam, it changes stronger with thickness deviations of blade 2, 5 and 6, than thickness changes of the other blades. The largest influence on the curve shape, due to the thickness change appears for blade 6. For the blade 3 thickness variation, the 1st plateaus are very flat. The change of the Laue phase is enumerated in tab. 2.4 for the first two plateaus. Concerning the determination of fundamental parameters employing Laue phase measurements, we obtain the important result that the geometry of the interferometer blades, have to be known with an accuracy below $1 \mu\text{m}^{24}$, exactly where the neutron beam passes.

²⁴This would mean a change of our hitherto used measuring method at Rauch company, chap. A.4.

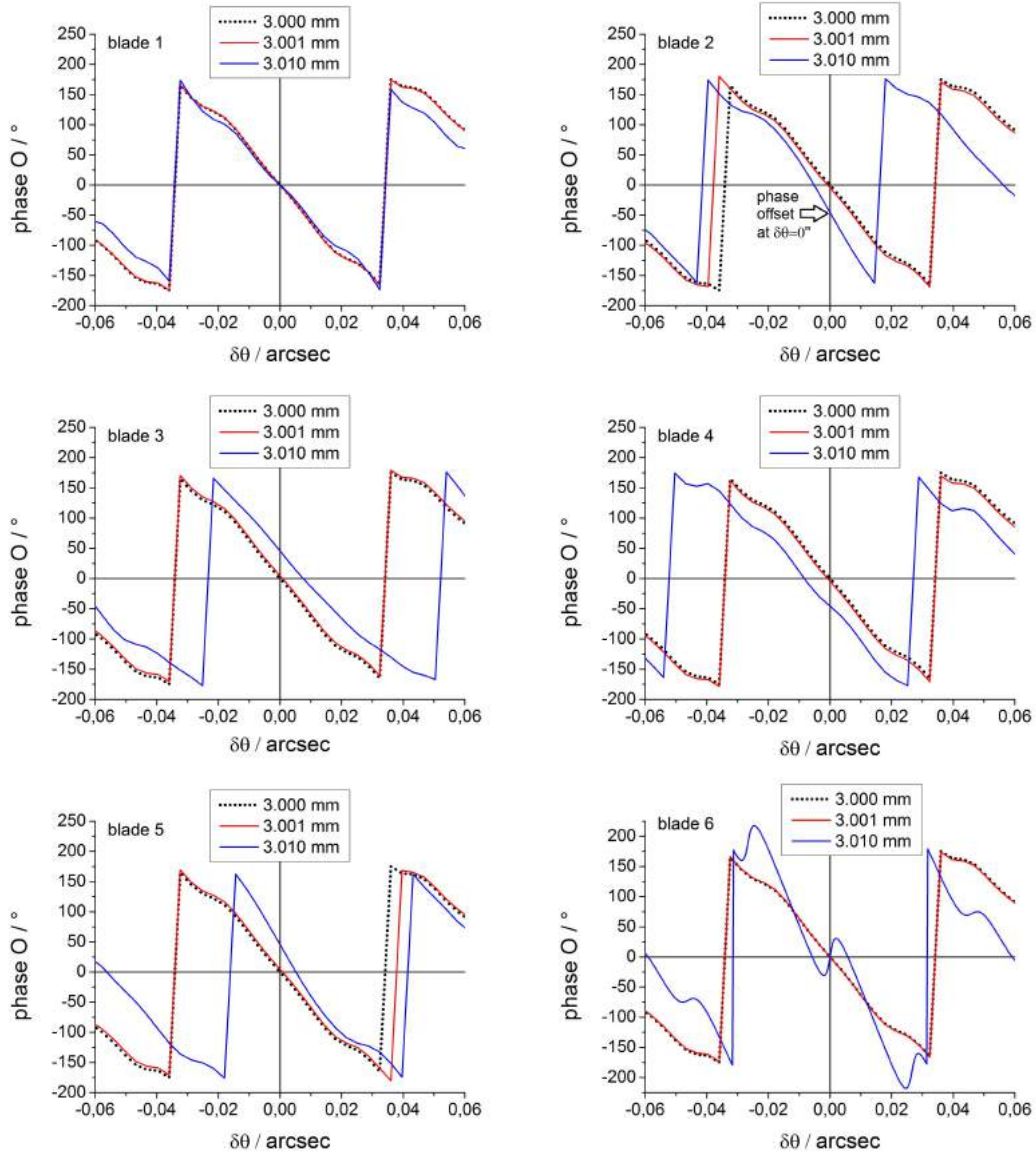


Figure 2.18.: Blade thickness influence on the Laue phase. Only one blade deviates $1 \mu\text{m}$ or $10 \mu\text{m}$ from 3 mm . The phase curve is characterized by its offset at $\delta\theta = 0''$, the slope and the position of the plateaus. Parameters: blade 3 rotation, (220). Note that the phase is plotted mod 2π (except blade 6).

Table 2.4.: Blade thickness influence on the Laue phase. Evaluated at specific $\delta\theta$ values: 1st and 2nd plateaus. The stated values are phase O changes, relative to the ideal IFM geometry (all blades 3 mm thick). The phase at $\delta\theta = 0''$ in fig. 2.18 is subtracted.

blade no. + thickness change	phase change /° 1 st plateaus	phase change /° 2 nd plateaus
blade 1 + 0.1 μm	0.04	0.07
blade 1 + 1 μm	0.4	0.7
blade 1 + 5 μm	1.4	10.6
blade 1 + 10 μm	13	34
blade 2 + 0.1 μm	0.11	0.11
blade 2 + 1 μm	0.85	0.85
blade 2 + 5 μm	6.2	12.2
blade 2 + 10 μm	34	60
blade 3 + 0.1 μm	0.04	0.09
blade 3 + 1 μm	0.4	0.9
blade 3 + 5 μm	3.2	5
blade 3 + 10 μm	10	10
blade 4 + 0.1 μm	0.06	0.07
blade 4 + 1 μm	0.7	0.7
blade 4 + 5 μm	2	3
blade 4 + 10 μm	3.2	5
blade 5 + 0.1 μm	0.12	0.12
blade 5 + 1 μm	0.85	0.85
blade 5 + 5 μm	6.18	12.2
blade 5 + 10 μm	30	60
blade 6 + 0.1 μm	0.07	0.15
blade 6 + 1 μm	1.09	1.8
blade 6 + 5 μm	13.65	18.62
blade 6 + 10 μm	90	90

The contrast curve in fig. 2.19 is characterized by its height value at $\delta\theta = 0''$, curve shape and symmetry around $\delta\theta = 0''$. The largest height reduction and shape change is due to the thickness variation in blade 6 and 1. Note the similar behavior of blade 3 and 4, but like in the phase the 1st plateaus are smeared out. Referring to chap. 2.3.3, note that the increasing blade thickness in one beam path can not shift the peak in $\delta\theta$.

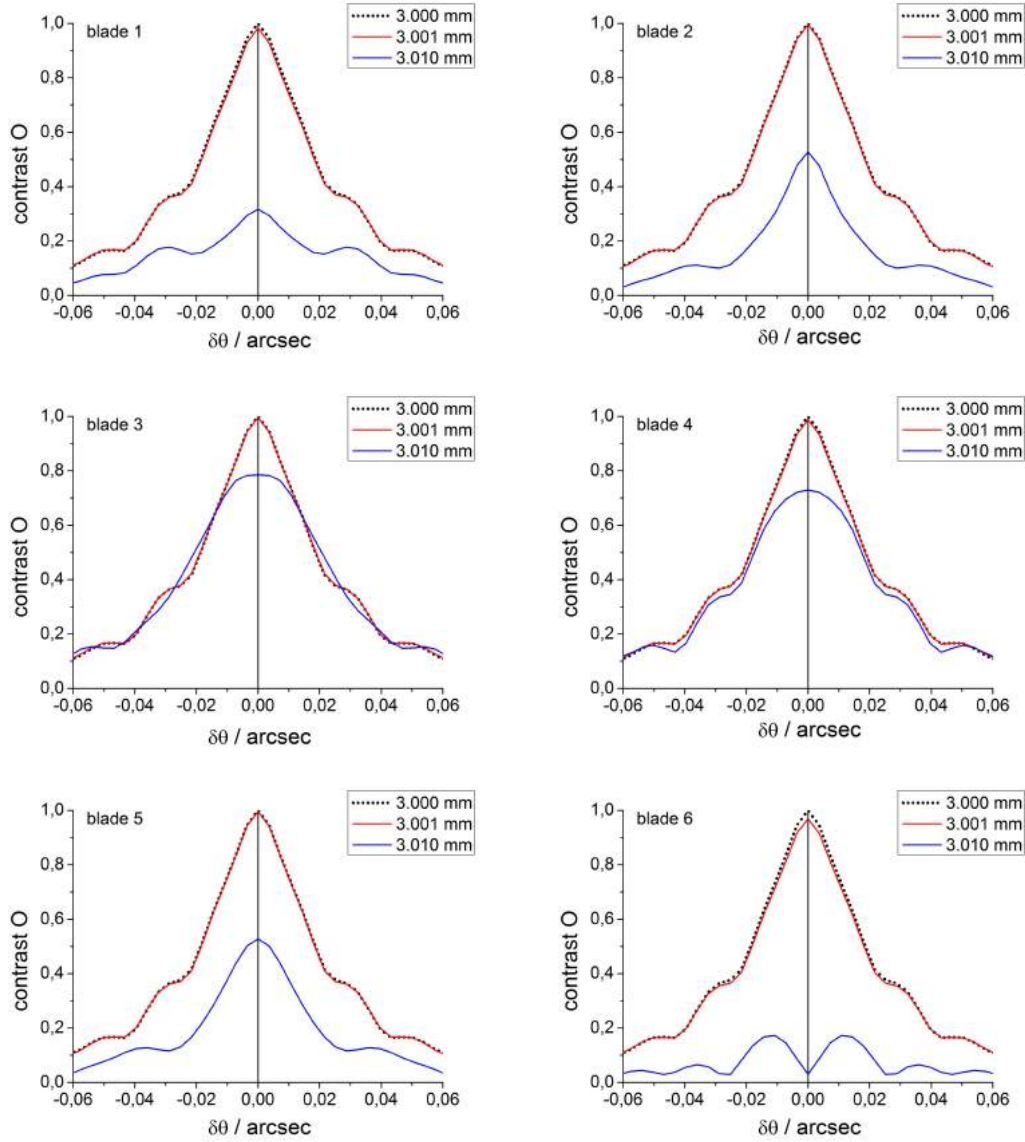


Figure 2.19.: Blade thickness influence on the contrast. Only one blade deviates $1 \mu\text{m}$ or $10 \mu\text{m}$. The contrast curve is characterized by its height value, curve shape and symmetry around $\delta\theta = 0''$. Same parameters as in fig. 2.18.

The geometries 'ideal', 'real I', and 'real II'

So far we changed only an individual blade thickness, now a specific combination of different blades with simultaneous thickness changes will be performed. This specific thickness values are given by our interferometer geometries. We use basically three different geometries: an ideal interferometer with 3 mm thick blades and two measured geometries, where 'real I' and 'real II' are from two different measurements at two different positions on the interferometer blades. The position is chosen approximately according the area where the neutron beam passes the IFM blades. We will determine which measuring geometry is more suitable.

The fringe visibility at $\delta\theta = 0''$ is significantly higher for the ideal than for the real interferometer geometry, due to equal blade thicknesses in both IFM paths. The real I geometry does not show large thickness deviation of a single blade (tab. A.2), while in the real II geometry - the blade 2 deviates about $2. \dots 4 \mu\text{m}$ from the other lamellas. The Laue phases are calculated with these geometries and their phase differences are shown in fig. 2.20. The influence of these geometries is in the range of up to 10° .

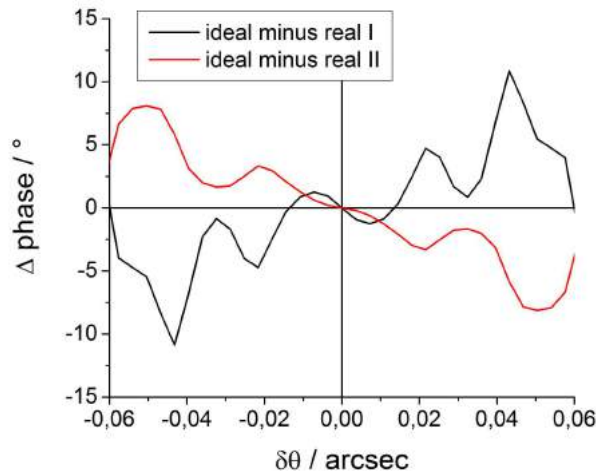


Figure 2.20.: Difference of the Laue phase with geometry real I, II, ideal.

Phase versus rocking angle

The phase versus the rocking-angle reveals a fascinating dependence on the geometry²⁵ (this is not the Laue phase !). This strong phase change can be understood with the different type of phase averaging if the rocking position changes; the specific geometry plays an important role, therefore we used the phase versus the rocking angle to determine our interferometer geometry, whether real I or real II is more suitable. Fig. 2.21 shows this phase for the calculated geometries 'ideal', 'real I', and 'real II', and compare it with measurements. In the measurement procedure, at every phase shifter position, the rocking angle is changed two times. In detail, the phase difference is measured between the rocking angle -0.9 and 0.9 arcsec for (220) and between -0.36 and 0.36 arcsec

²⁵Personal communication H. Lemmel

for the (440) Bragg peak. Therefore, the points at rocking angle -0.9 and -0.36 arcsec are arbitrary in height and hence shifted to the calculated values of real I. The measured points represent an average value of 41 (220) and 32 (440) single measurements. As a result, the 'real I' geometry is favored for both wavelength, therefore it will be used in the following chapters. This is probably because the thickness measurement in real II is done at a higher position than where the neutron beam passes the interferometer.

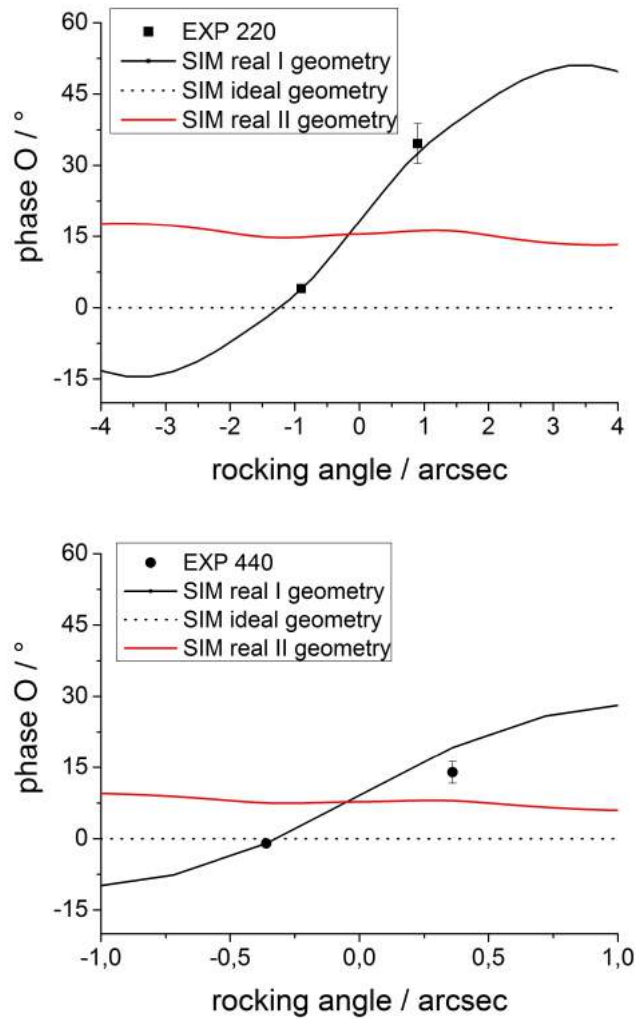


Figure 2.21.: Rocking phase of the real I, II and ideal geometry; (top) for the (220) and (bottom) for the (440) Bragg peak. If all blades would be equally thick, this phase would be zero. The measured values favor the 'real I' geometry.

2.4.2. Temperature

First correlations between the interferometer phase and the temperature changes on a small neutron perfect-crystal interferometer have been demonstrated in [32]. Therefore, the temperature is recorded and can be changed during our measurements with the larger interferometer. The possibilities of the used temperature setup are presented in chap. A.5. In the following, the temperature of the interferometer and its surrounding is investigated. In order to improve the contrast and therefore enhance the accuracy of the phase measurements.

Rocking: a series of rocking curves is compared with the interferometer's temperature within 9 days. The rocking curve is the intensity versus a rotation of the interferometer in the horizontal plane, according to fig. 2.34 (no prism rotation). The development of the intensity maximum and the FWHM of this rocking curve is depicted in fig. 2.22. Additionally, its peak maximum positions are given in fig. 2.35. The measurement time per point in the rocking curve is here 6 seconds. A clear correlation might not be visible for this sensor position (laterally, basis right).

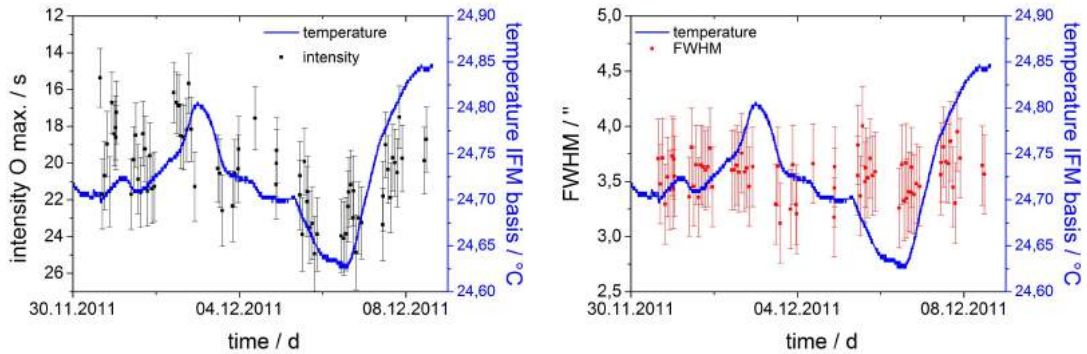


Figure 2.22.: Rocking curve and interferometer temperature. (left) Intensity maximum, (right) FWHM, for the peak maximum positions see fig. 2.35.

Phase and contrast of the empty interferometer: we record the interferometer's intrinsic phase/contrast, and compare it first with the temperature of the monochromator and then with the temperature of the interferometer itself. The phase and contrast are measured with the phase sifter rotation and without a sample, typical values of such an interferogram are listed in chap. 2.2.1. The monochromator temperature can not be controlled, it changes due to an insufficient isolation from the neutron guide hall. This temperature is compared with the phase/contrast in fig. 2.23 within 48 h. The sensor for the monochromator is an integrated-circuit temperature sensor²⁶ with an accuracy of about $\pm(10...20)$ mK. The interferometer temperature (at its basis) is in the first 24 h decreasing from 23.77°C to 23.68°C and in the second half constant at $23.674(1)^{\circ}\text{C}$, there the contrast is significantly higher. For the stability of the intrinsic phase however, no difference between the first and the second 24 hours is observable.

²⁶LM35 Precision Centigrade Temperature Sensor from National Semiconductor.

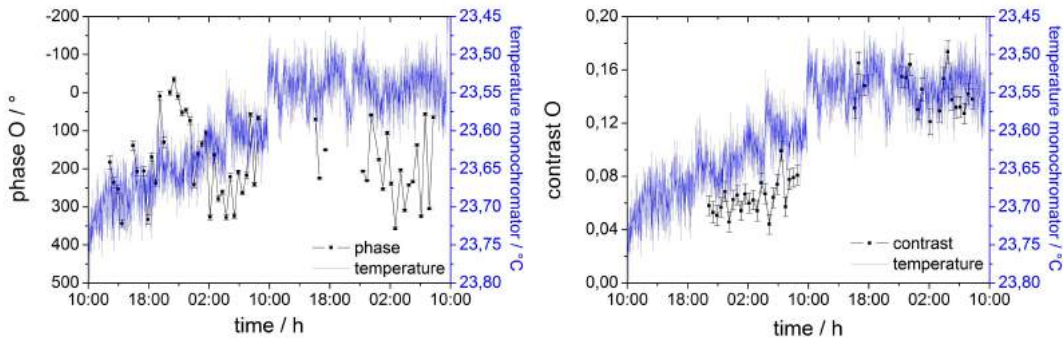


Figure 2.23.: Measured phase (left) and contrast (right) of the empty interferometer, compared with the monochromator temperature within 48 h.

Several parameters have been varied:

- use of the heating mat (around the Al box/below the stage) or the Al box only
- mounting the Peltier elements on the box wall or on the lid
- with/without air circulation in the box (compressed air flow or slit on the box top/bottom)
- set temperature of the control loop (higher/lower than outside the box, following monochromator)
- temperature differences: box center - wall, box center - monochromator, box center - outside the box, vertical difference in the box center
- two additional boxes in the Al box, closely around the interferometer

All these measures did not lead to a reproducible contrast control; most likely, the visibility reductions are due to small temperature gradients at the interferometer blades. Furthermore, the temperature of the monochromator has to be taken into account as well, therefore a stabilization of the whole experimental room would be necessary²⁷ [33]. However, in fig. 2.24 we found a correlation of the IFM temperature and the contrast/phase within 14 hours. The sensor position is placed on the base of blade 2.

For a 1 mK temperature change of the interferometer, the phase changes about 7° . The contrast varies from 10% to 35%. Note the larger time scale in the rocking peak position diagram.

Laue phase, contrast and intensity: in fig. 2.25 the Laue phase, contrast and intensity measurements are shown for two different interferometer temperatures: $22.5(3)^\circ\text{C}$ and $23.15(5)^\circ\text{C}$. The phase, contrast and intensity behavior do not change²⁸. Every point at $23.15(5)^\circ\text{C}$ represents an average value of about 7...9 single measurements. The values at $22.5(3)^\circ\text{C}$ are taken from chap. 2.3.

²⁷An active temperature control of the monochromator would be interesting.

²⁸For a small contribution from the Debye-Waller factor to the scattering length, see chap. 2.4.8.

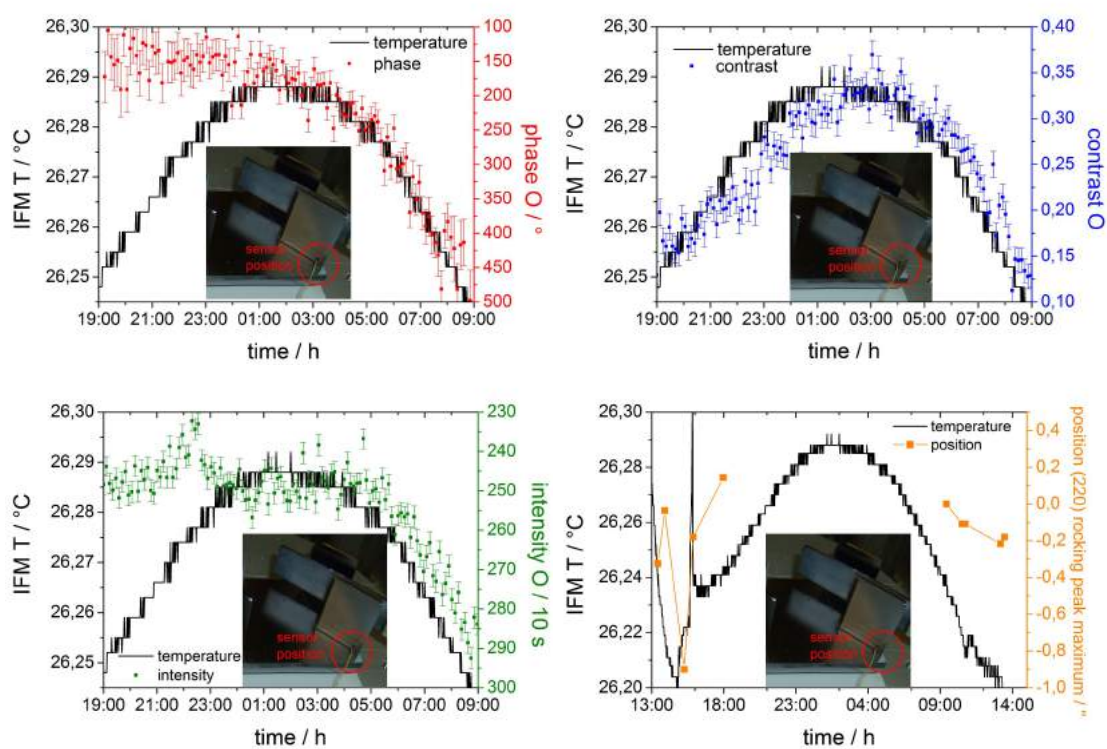


Figure 2.24.: IFM temperature and phase (top left), contrast (top right), intensity (bottom left) and rocking peak maximum position (bottom right). The monochromator temperature during this time remains constant at $23.05(5)^{\circ}\text{C}$.

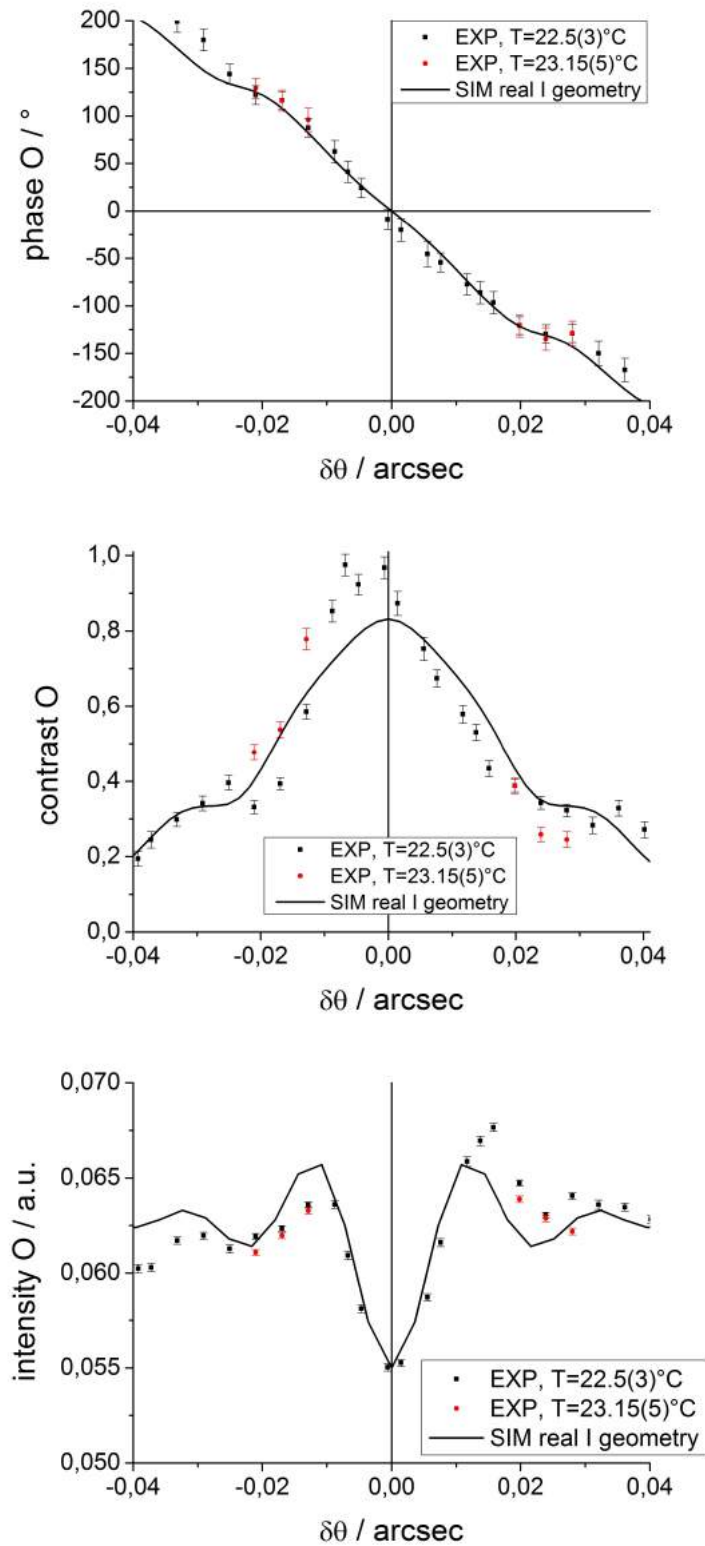


Figure 2.25.: Laue phase (top), contrast (middle) and intensity (bottom) for different absolute interferometer temperatures; (220) Bragg peak. The EXP values are shifted for $\delta\theta = 0.0035''$ according to chap. 2.3.

2.4.3. Monochromator

At the monochromator a Bragg reflection directs the neutrons to the interferometer with a certain angular divergence and wavelength distribution. The angular distribution of the intensity within the beam divergence is of interest in this chapter, because it characterizes different types of monochromators. In our experiments a perfect-crystal monochromator is used, which is described in chap. 2.2. The specific alignment procedure can be found in chap. A.5. For the calculations this monochromator is described by the Bragg distribution function, the analytical expression is given in the following equation, where I represents the intensity:

$$I = 1 \quad |y| < 1$$

$$I = 1 - \sqrt{1 - y^{-2}} \quad |y| > 1 \quad (2.29)$$

In principle, one could also use a mosaic-crystal monochromator; which is represented by a Gaussian reflection curve. Such a monochromator is employed at the NIST facility. In order to study the difference resulting from this different types of monochromators, we extended our simulation program, where additionally a square function can be chosen. All three monochromator reflection curves ('Square', 'Gauss' and 'Bragg') are shown in fig. 2.26 (left), the y - $\delta\theta$ relation is given in chap. 2.1.

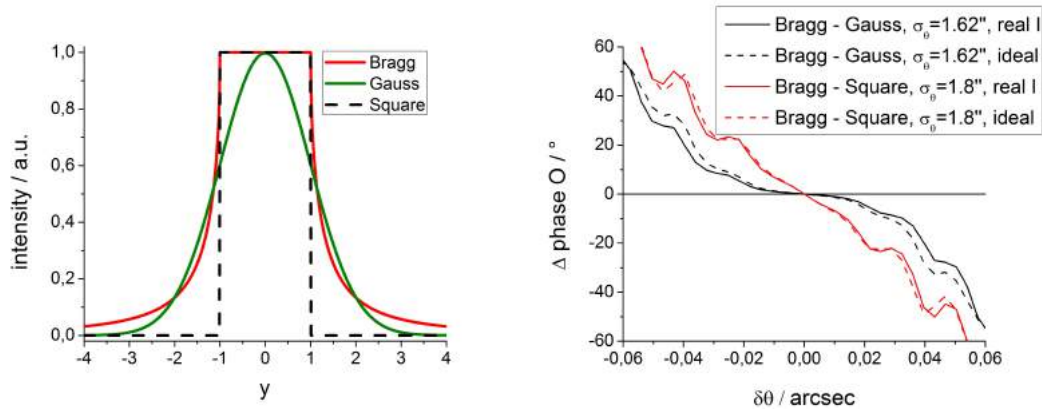


Figure 2.26.: (left) Comparison of Bragg, Gauss and Square monochromator functions. (right) Calculation of the Laue phase difference (Bragg minus Gauss and Bragg minus Square) vs. the beam deflection $\delta\theta$ for the (220) case and ideal/real I geometry.

Calculations of the Laue phase can now be performed with each of this reflection curves. The difference in the phase calculated with a Bragg monochromator minus the phase calculated with a Gauss (Square) function is drawn in fig. 2.26 (right). It shows a remarkable effect of the used monochromator type on the Laue phase. This phase difference is caused by different excitations of plane wave components that are slightly off-Bragg.

Furthermore, the phase difference depends strongly on the beam divergence σ_θ and will be investigated separately. Here we use the σ_θ values which are determined in the next section, from a comparison to rocking-curve measurements. The result is $\sigma_\theta = 1.62''$ (Gauss) and $\sigma_\theta = 1.8''$ (Square). In the calculations with the Bragg function the Darwin

width equal to 1 is used. However, in IFMSIM, it is possible to change the Darwin width of the Bragg curve and interpret it as the mosaicity of the monochromator, or the divergence of a single wavelength²⁹.

The evaluation of the calculations are given in tab. 2.5 in detail. The Laue phase change in the plateaus are listed for several beam divergences.

Table 2.5.: Laue phase O change with different monochromator functions with respect to the Bragg curve. This phases are evaluated for the (220) case and 'real I' interferometer geometry at specific $\delta\theta$ values (1st and 2nd plateaus).

monochromator function	phase change 1 st plateaus	phase change 2 nd plateaus
Bragg, Darwin width = 1	0°	0°
Gauss, $\sigma_\theta = 1.44''$	1°	17°
Gauss, $\sigma_\theta = 1.62''$	7°	27°
Gauss, $\sigma_\theta = 1.8''$	12°	35°
Square, $\sigma_\theta = 1.44''$	10°	23°
Square, $\sigma_\theta = 1.62''$	17°	37°
Square, $\sigma_\theta = 1.8''$	23°	48°

The contrast and intensity for the different monochromator functions are shown in fig. 2.27. It reveals a change in height of the Pendelloesung plateaus. Therefore, an imperfect monochromator can be a possible explanation for a deviation between measurement and calculation. The intensity and phase versus the rocking angle for all three monochromator functions are compared in fig. 2.28, the measurements can not clearly favor the Bragg curve. However, in the following calculations the Bragg function is used because it is the physical monochromator function.

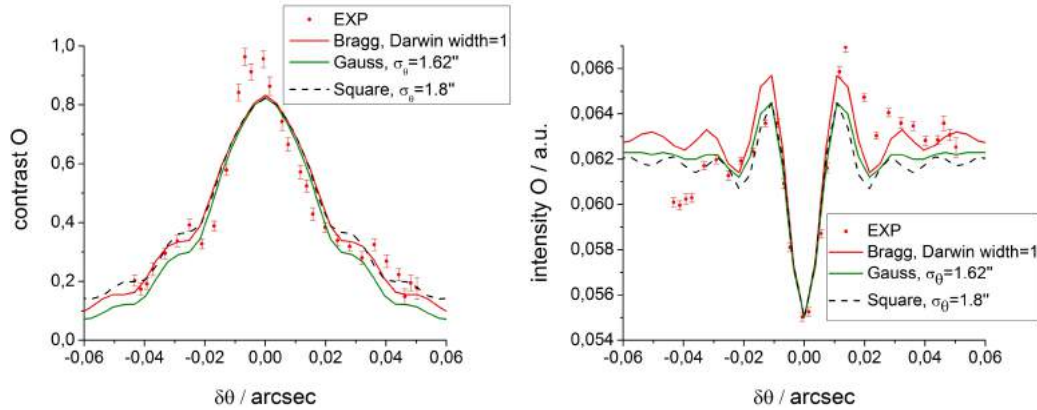


Figure 2.27.: Calculation of the contrast (left) and intensity (right) with different monochromator functions. The measurements are taken from chap. 2.3.

²⁹The calculations are done for a single wavelength only, since the wavelength dependence is negligible within our wavelength distribution.

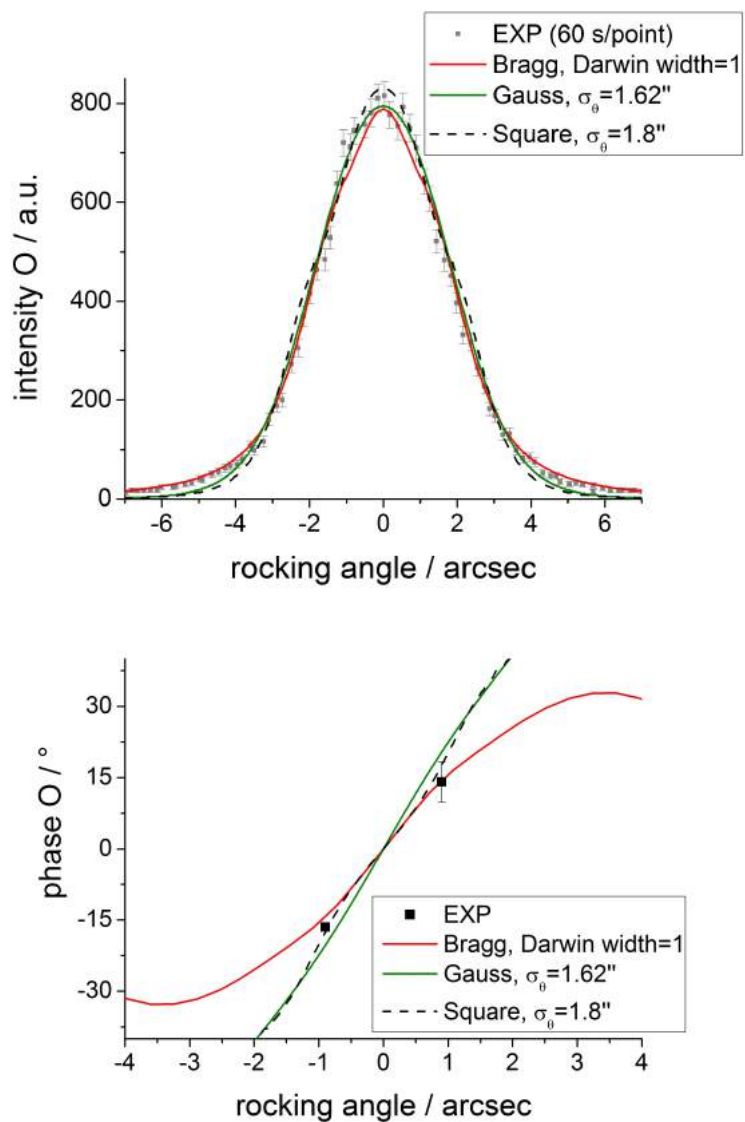


Figure 2.28.: Calculation of the intensity (top) and phase (bottom) vs. the rocking angle for three monochromator functions.

2.4.4. Beam divergence

The neutron beam in our calculation consists of a superposition of plane wave components as illustrated in fig. 2.29. Its divergence σ_θ is mainly determined by the crystal monochromator.

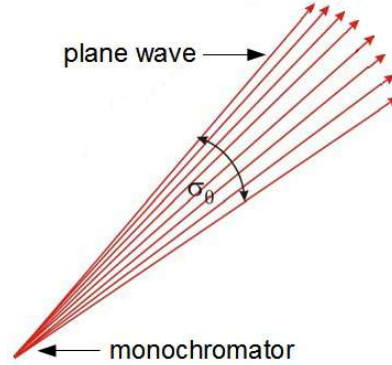


Figure 2.29.: The neutron beam with divergence σ_θ is described as a coherent superposition of plane waves with a distribution of wavevector directions σ_θ centered around a mean value.

As a first step, we calculate rocking curves³⁰ with several different values of σ_θ . Fig. 2.30 shows these calculations for the intensity and the phase. The (left) diagram reveals that the full width at half maximum (FWHM) of the rocking curve changes strongly. In particular for large σ_θ ($36''$), the width of the rocking curve is so large that the intensity remains constant in the center. In the limit of small σ_θ (plane wave, [21]) the intensity becomes double peaked for smaller values than $\sigma_\theta = 0.72''$ (Square), $\sigma_\theta = 0.86''$ (Gauss) and Darwin width = 0.593 (Bragg). Additionally, in the (right) diagram one can see that the rocking phase slope decreases with increasing σ_θ .

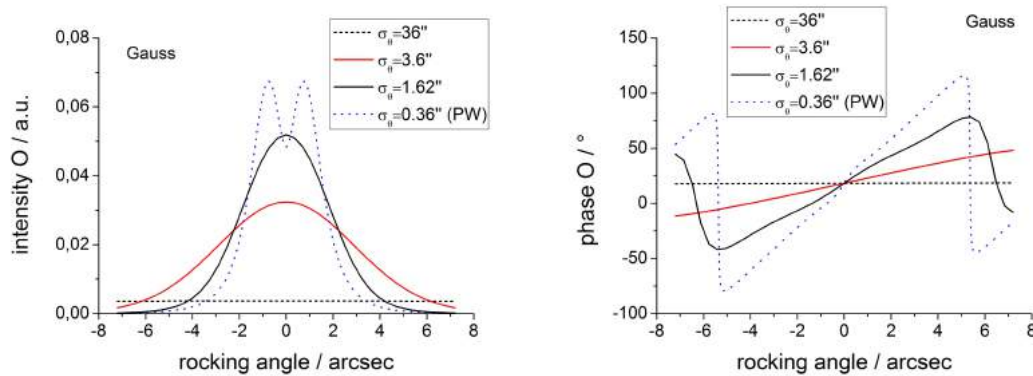


Figure 2.30.: Rocking intensity (left) and phase (right) with different beam divergences. The intensity peak broadens and the rocking phase slope decreases with increasing beam divergence. Parameters: (220) case, real I geometry, Gauss monochromator; PW... plane wave.

³⁰The rocking angle is illustrated in fig. 2.34.

The question arises how the beam divergence can be manipulated in the experiment. A possibility is the tilt of the interferometer's lattice planes relative to the monochromator. This increases the FWHM of the rocking curve and, thus, the effective mosaicity. This tilt-angle is the ρ -axis angle, it is illustrated in fig. A.11. A comparison of the experimental values for two different ρ -axis angles, with a calculation is given in fig. 2.31.

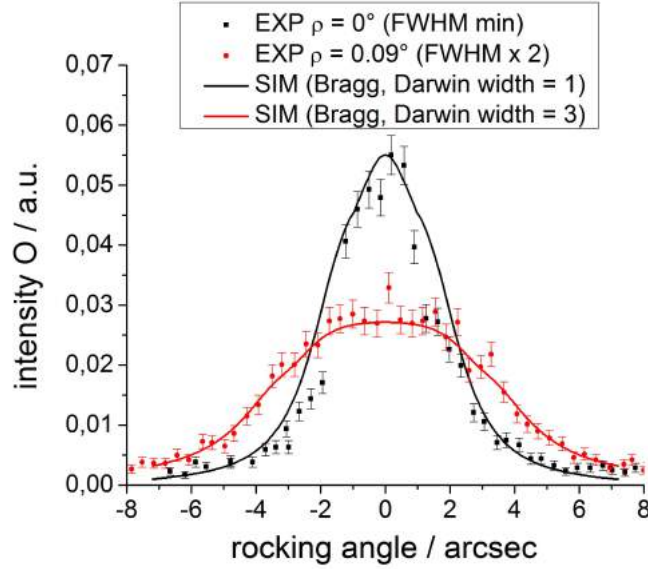


Figure 2.31.: Rocking curves, measurements (10 s/point) at $\rho = 0^\circ$, $\rho = 0.09^\circ$ and calculations with different Darwin widths, (220) reflection, real I geometry.

As the rocking curve depends on the beam divergence, we can use the measured rocking curves to determine the σ_θ values. These values are listed in tab. 2.6, the diagrams can be found in chap. A.6. The calculated rocking curves have a certain FWHM and area, which are summarized in tab. 2.7 (for $\rho = 0^\circ$ only).

Table 2.6.: Beam divergences determined from rocking curves in chap. A.6.

monochromator function	$\rho = 0^\circ$	$\rho = 0.09^\circ$
Gauss	$\sigma_\theta = 1.62(18)''$	$\sigma_\theta = 4.14(54)''$
Square	$\sigma_\theta = 1.80(18)''$	$\sigma_\theta = 4.14(54)''$
Bragg	Darwin width=1.0(2)	Darwin width= 3.0(2)

Table 2.7.: Rocking curve at $\rho = 0^\circ$: FWHM and area (determined via a Gauss fit).

rocking curve	FWHM	area
Gauss, $\sigma_\theta = 1.62''$	4.2''	0.237 a.u.
Square, $\sigma_\theta = 1.80''$	4.17''	0.237 a.u.
Bragg, Darwin width=1	4.04''	0.251 a.u.

If all of the FWHM values of this rocking curves are drawn as a function of σ_θ /Darwin width one obtains fig. 2.32. Note that the values are normalized to the $\rho = 0^\circ$ value of tab. 2.7. The rocking curve areas are used in chap. A.6 to scale the height of the experimental values. Now we change from the rocking curve investigation to the

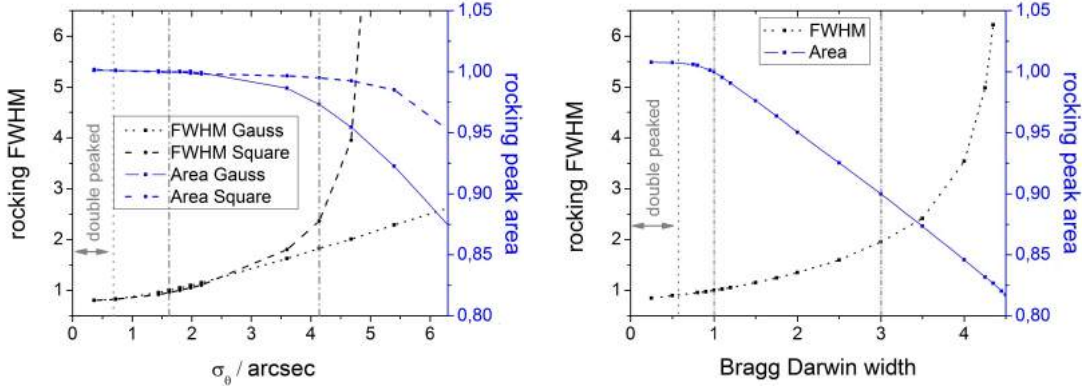


Figure 2.32.: Comparison of the beam divergence (left) with the Darwin width (right), regarding the FWHM and area of the rocking curve for the (220) case. (The 2 gray dash dotted lines mark the σ_θ /Darwin width values where the measurements are taken, fig. 2.31).

influence of the beam divergence on the Laue phase. Fig. 2.33 compares the Laue phase measurements for two different Darwin widths. It can clearly demonstrate a large influence of the beam divergence on the measured as well as calculated Laue phase. The measured values at $\rho = 0.09^\circ$ represent an average of about 3...9 single measurements. The slope of the phase around $\delta\theta = 0''$ decreases with increasing Darwin width and approaches $4.3^\circ/0.001$ arcsec at a Darwin width > 3 . A larger Darwin width means that parts of the beam are further away from the exact Bragg condition of the interferometer crystal, where they contribute less and less to an average phase. This leads to a constant phase for Darwin width > 3 at each $\delta\theta$ and therefore a constant phase slope. This would be the case for a mosaic-crystal monochromator at NIST. The difference in the phase values is remarkable, the evaluation is listed in tab. 2.8. Regarding chap. 2.3, the corresponding contrast and intensity of the $\rho = 0.09^\circ$ measurements do not show a $\delta\theta$ -shift compared to $\rho = 0^\circ$.

Table 2.8.: Laue phase O change at different Darwin widths. This phases are evaluated for the (220) case and 'real I' interferometer geometry at specific $\delta\theta$ values (1st and 2nd plateaus).

Darwin width	phase change 1 st plateaus	phase change 2 nd plateaus
1	0°	0°
1.2	6°	30°
3	36°	70°
6	36°	70°

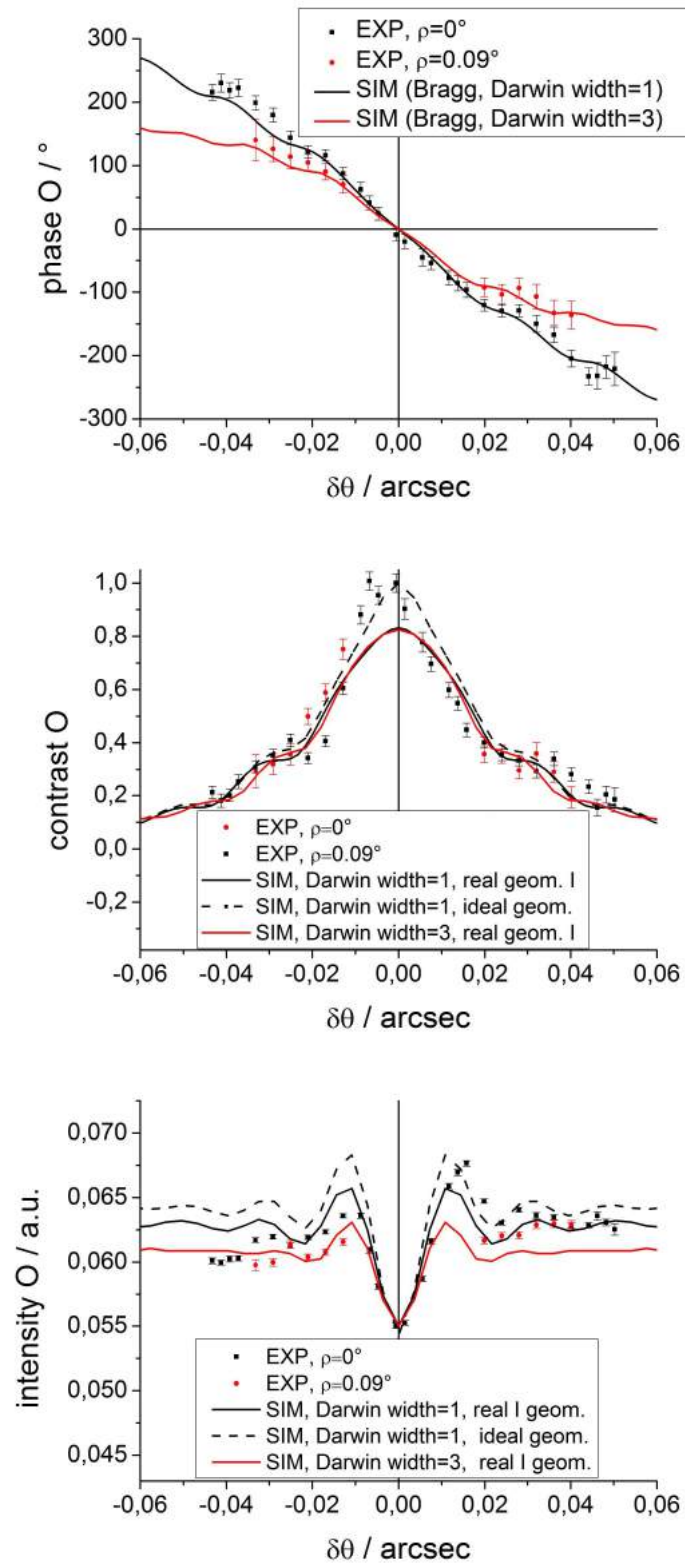


Figure 2.33.: (top) Laue phase, contrast (middle) and intensity (bottom) at $\rho = 0^\circ$ and $\rho = 0.09^\circ$, respectively. All experimental values are shifted by $\delta\theta = 0.0035''$ according to chap. 2.3.

2.4.5. Rocking position

The rocking angle is defined in fig. 2.34, due to experimental conditions, this angle between the interferometer and the neutron beam can slightly change.

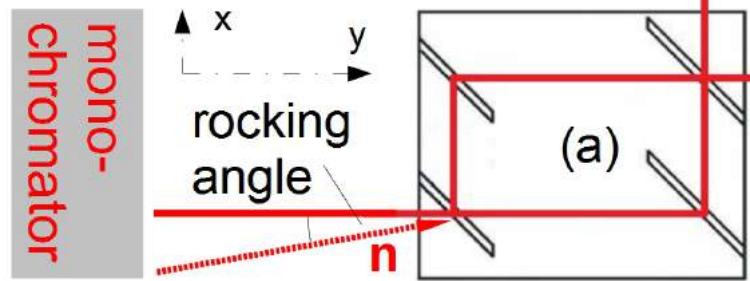


Figure 2.34.: Rocking angle: the interferometer (a) is rotated in the x-y plane with a piezo device to perform a rocking curve, while the monochromator is fixed.

The reason for such rocking drifts are mainly temperature changes within the setup (monochromator-interferometer-optical bench), see chap. 2.4.2; as well as drifts of the 'piezo' rotation device. Note that the ρ -axis and the IFM support can change this position as well. To compensate larger drifts we perform rocking curves and correct for this position. The positions of the rocking curve peak within 8 days are shown in fig. 2.35 (left). The (220) rocking FWHM is about $3.6''$, drifts of > 1 arcsec are visible, therefore this position has to be corrected very often during the phase measurement.

In this chapter the effect of the angular drift will be studied by considering different rocking positions for the phase measurements. In fig. 2.35 (right) the investigated positions on the rocking curve are indicated. These positions have been used to demonstrate the change in the Laue phase. The position 0 is at the peak maximum (rocking angle = $0''$) and the positions $\pm B$ are where the intensity has its half value at $\pm 1.8''$ ($\pm 0.0005^\circ$). Further positions between this values are defined as well: pos. $\pm A$ at $\pm 0.9''$ ($\pm 0.00025^\circ$).

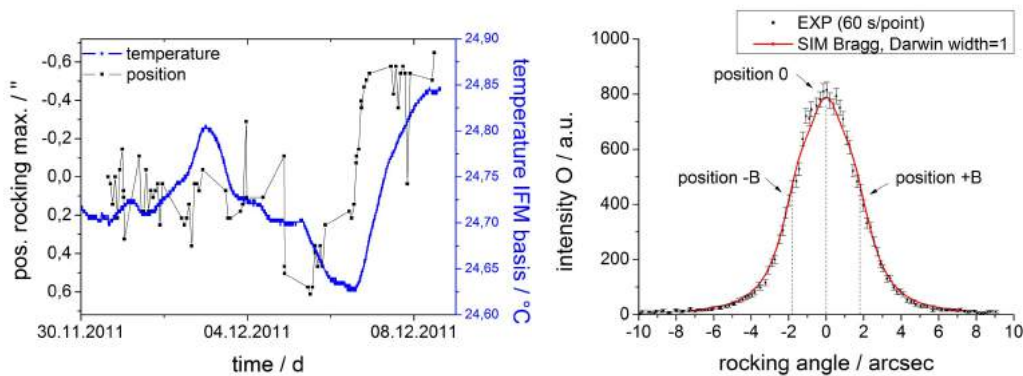


Figure 2.35.: (left) Peak maximum position of the rocking curve vs. time; the temperature of the IFM basis is given as well. (right) Definition of the rocking positions. Pos. 0: rocking angle = $0''$, pos. $\pm B$: $\pm 1.8''$. (220) Bragg peak.

One can now perform several Laue phase measurements, each with a different rocking angle alignment. The results are shown in fig. 2.36 with the measured and calculated phases at the defined rocking positions³¹. The measured values in pos. $\pm B$ representing an average of about 5...8 single measurements. The slope of the phase around $\delta\theta = 0''$ decreases from $5.5^\circ / 0.001$ arcsec at pos. 0 to $3^\circ / 0.001$ arcsec at pos. $\pm B$. The phase change with the rocking-angle variation can be understood with the different phase averaging if the rocking position changes. At this $1.8''$ separated rocking positions one can demonstrate that the difference in the phase values is very large ($50...75^\circ$); however in order to yield the Laue phase uncertainty regarding our rocking angle device, we repeat the above phase measurement at the rocking position $0.18''$. The Laue phase changes at additionally rocking positions are summarized in tab. 2.9 as well; the listed phase changes are evaluated relative to the rocking position 0. We see that our rocking angle rotation device yields an error of up to 6 degrees in the Laue phase. Also the interferometer's geometry has an influence which increases with larger $\delta\theta$.

The corresponding contrast curves are given in fig. 2.37. Note that its peak maximum is not at $\delta\theta = 0''$, a Gauss fit close to the peak maximum gives a $\delta\theta$ -shift of about $\pm 0.0059''$. The intensity is shifted as well, as depicted in fig. 2.38. This results from the combination of the rocking deviation and the defocusing due to the different thick blades in the real interferometer geometry. This can be seen in the intensity diagram, where this situation is also calculated for the ideal geometry. In our measurement in chap. 2.3 the rocking position is corrected several times yielding only a small contribution to the $\delta\theta$ -shift discussed in chap. 2.3.3.

Further influences like the beam divergence and monochromator function on the contrast, as well as a calculation of the phase slope for every rocking position can be found in chap. A.7.

Table 2.9.: Laue phase ϕ change from different rocking positions with respect to pos. 0. Evaluated for the 'real I' interferometer geometry at specific $\delta\theta$ values (1^{st} and 2^{nd} plateaus).

rocking position	phase change 1^{st} plateaus	phase change 2^{nd} plateaus
pos. 0 (220)	0°	0°
$\pm 0.18''$ (220)	1°	6°
pos. $\pm A$ (220)	30°	65°
pos. $\pm B$ (220)	50°	75°
pos. 0 (440)	0°	0°
$\pm 0.18''$ (440)	$15 \dots 30^\circ$	$30 \dots 40^\circ$

³¹The rocking sign of the piezo in the experiment is inversely (consistently with fig. 2.21).

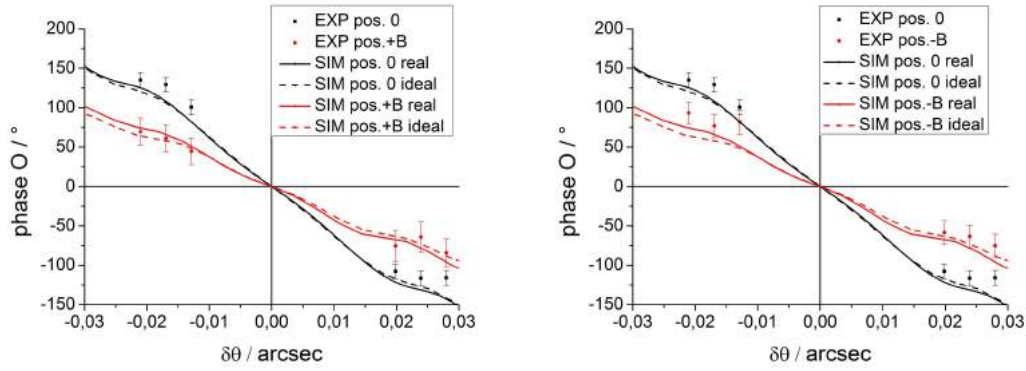


Figure 2.36.: Laue phase at different rocking positions. Measured values (EXP) are compared with calculations (SIM): (left) pos. +B and pos. 0, (right) pos. -B and pos. 0. The slope is strongly depending on the rocking angle. Parameters: (220) Bragg peak, all experimental values are shifted by $\delta\theta = 0.0035''$ according to chap. 2.3.

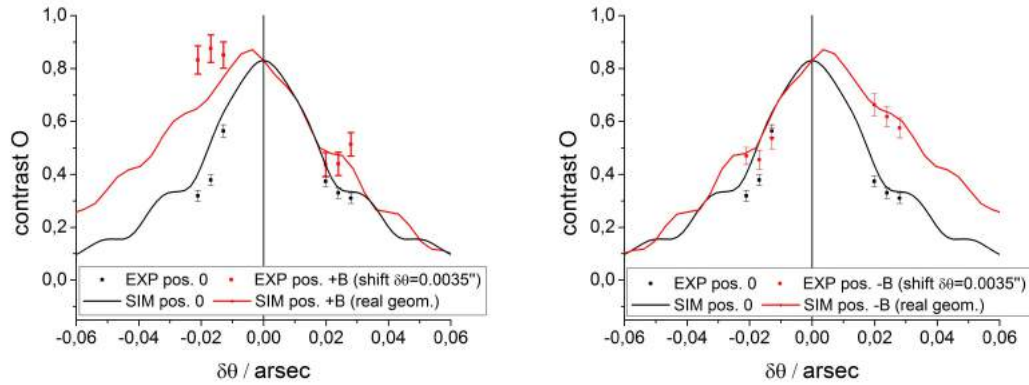


Figure 2.37.: Contrast behavior at different rocking positions. (left) Pos. +B is compared to pos. 0, (right) pos. -B and pos. 0. The calculated contrast maximum position is located at $\delta\theta = \pm 0.0059''$ and depends on the rocking angle.

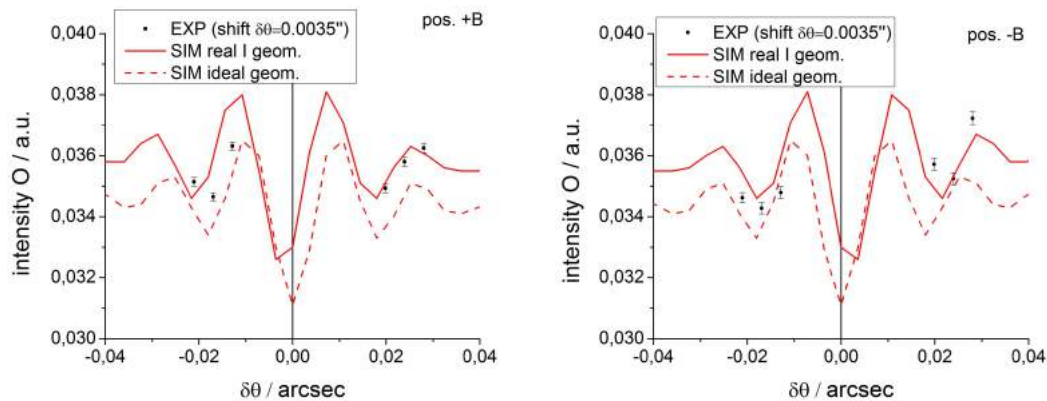


Figure 2.38.: Intensity behavior at different rocking positions. (left) Pos. +B, (right) pos. -B. A $\delta\theta$ -shift of $\pm 0.0021''$ is visible only for the real I geometry.

2.4.6. Al prisms

The Laue phase is measured very close to the Bragg condition, this small angle $\delta\theta$ constitutes a technical challenge for the sample rotation, therefore the neutron beam in front of the blade is deviated with an Al prism. This small beam deviation study can also be interesting for a split perfect crystal interferometer, which does not exist for neutrons so far [30], [34].

For the compensation of the interferometer's defocusing and the resulting phase shift, two prism pairs are used in our experiment. This four prisms are mounted together on a prism holding device to make a rotation in the x-z plane possible (fig. 2.11).

Basic parameters like the used material, prism alignment and pair design are discussed in [30], here we extended IFMSIM for the calculation with prisms. Several parameters will be investigated for a possible influence on the Laue phase, intensity, and contrast³². But first we have to show that the prism α -rotation is equivalent to the blade rotation (eq. 2.26). Our calculations with IFMSIM show in fig. 2.39 that this is indeed identical. Also the contrast and intensity behavior is the same.

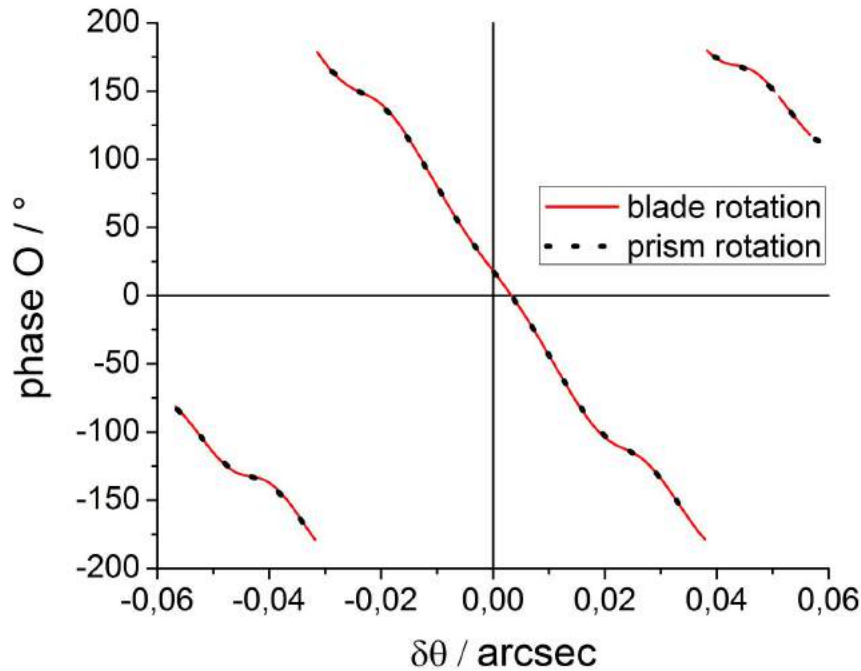


Figure 2.39.: Equivalence of blade and prism rotation for the Laue phase ((220) Bragg peak, Darwin width=1, real I geometry).

Also to mention is that the sign of $\delta\theta$ changes if the first prism points downwards instead of upwards (fig. 2.40), or blade 4 instead of blade 3 rotates.

³²We will also look for additional contributions to the $\delta\theta$ -shift mentioned in chap. 2.3.3.

The prism holding device

The rotation of all four prisms together is performed with the help of the prism holding device. Here we will investigate if a change of the collectively mounted prisms has a significant influence on the Laue phase.

Forward tilt of the prism holding device $slope_{phd}$: fig. 2.40 defines the tilt angle of both prism pairs in the neutron beam direction.

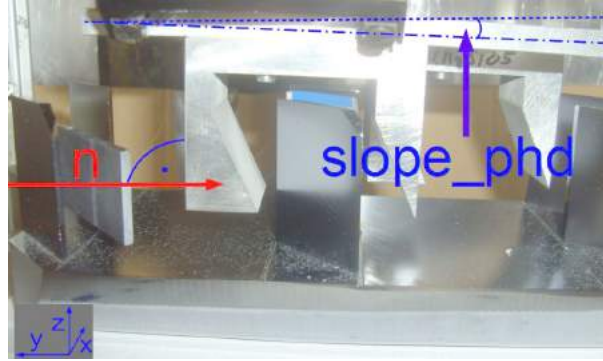


Figure 2.40.: Definition of the $slope_{phd}$ angle. Both prism pairs are tilted in the y-z plane.

The measurements at $slope_{phd} = 0^\circ$ and 0.5° do not show a difference on the Laue phase within the error bars (fig. 2.41). Also the contrast and intensity behavior do not change. The difference between the calculation at $slope_{phd} = 0^\circ$ and 0.5° is given in fig. 2.41, the Laue phase changes up to 1° . Hence, for a precise Laue phase measurement ($< 0.1^\circ$) the $slope_{phd}$ angle must be known within 0.01° , with our prism holding device this can not be realized, therefore a maximal phase error of 1° arises here.

Rotation of the prism holding device r_{phd} : the mounting of the prism holding device with a rotation offset in the x-y plane is depicted in fig. 2.42. Measurements at $r_{phd} = 0^\circ$ and 1° do not show a difference on the Laue phase within the error bars (fig. 2.43). Also the contrast and intensity behavior do not change. In fig. 2.43 the difference between the calculation for $r_{phd} = 0^\circ$ and 1° is given. Hence, the r_{phd} angle must be known within 0.01° for an exact Laue phase measurement ($< 0.1^\circ$). This is not possible either, therefore a maximal phase error of 1° arises here as well.

Pivot of the prism holding device for the α -rotation: due to the use of a different prism holding device compared to [4], the pivot of the prism α -rotation has been changed. This point of rotation is the same for all four prisms (fig. 2.44). Therefore IFMSIM was extended to make a pivot change possible. If there would be just one prism in the interferometer (prism 1), then a change of the x and z-component of the pivot leads to a change of the Laue phase, but this is compensated by the following prism (prism 2) behind the sample blade (both prisms have the same pivot). Hence, the calculation does not show an influence on the Laue phase, intensity, and contrast for four prisms if the point of rotation is changed in x, y or z direction.

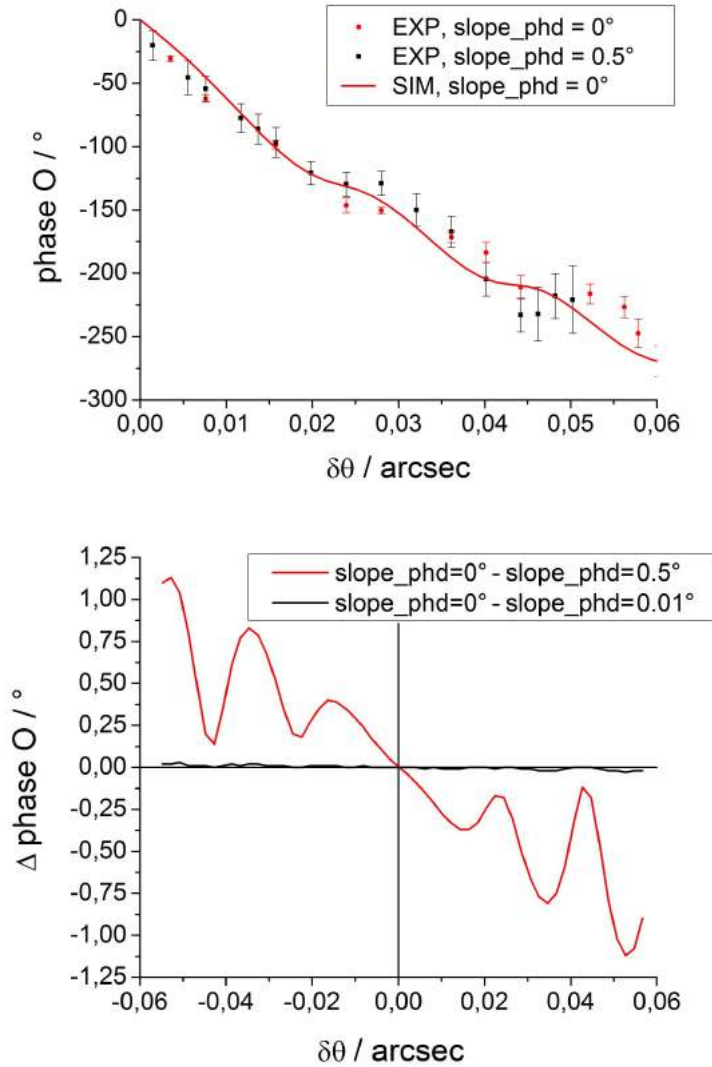


Figure 2.41.: (top) Laue phase measurement with a tilted prism holding device (measurement at $\text{slope}_{phd} = 0^\circ$ and 0.5° , the calculation is given only for 0°). The difference between the phases at the 2 angles is within the error (about $\pm(5\dots 10)^\circ$). (bottom) Laue phase calculation at $\text{slope}_{phd} = 0.01^\circ$ and 0.5° , the difference to $\text{slope}_{phd} = 0^\circ$ is shown. Therefore the prisms have to be aligned to 0.01° . Parameters: (220) Bragg peak, Darwin width=1, real I geometry, EXP are shifted by $\delta\theta = 0.0035''$ according to chap. 2.3.

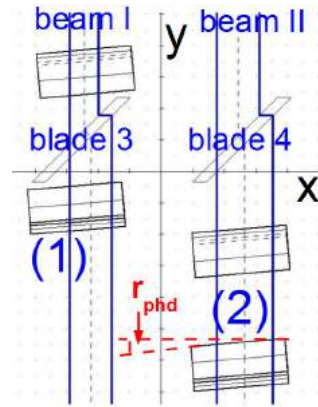


Figure 2.42.: r_{phd} angle: both prism pairs (1) and (2) are rotated in the x-y plane.

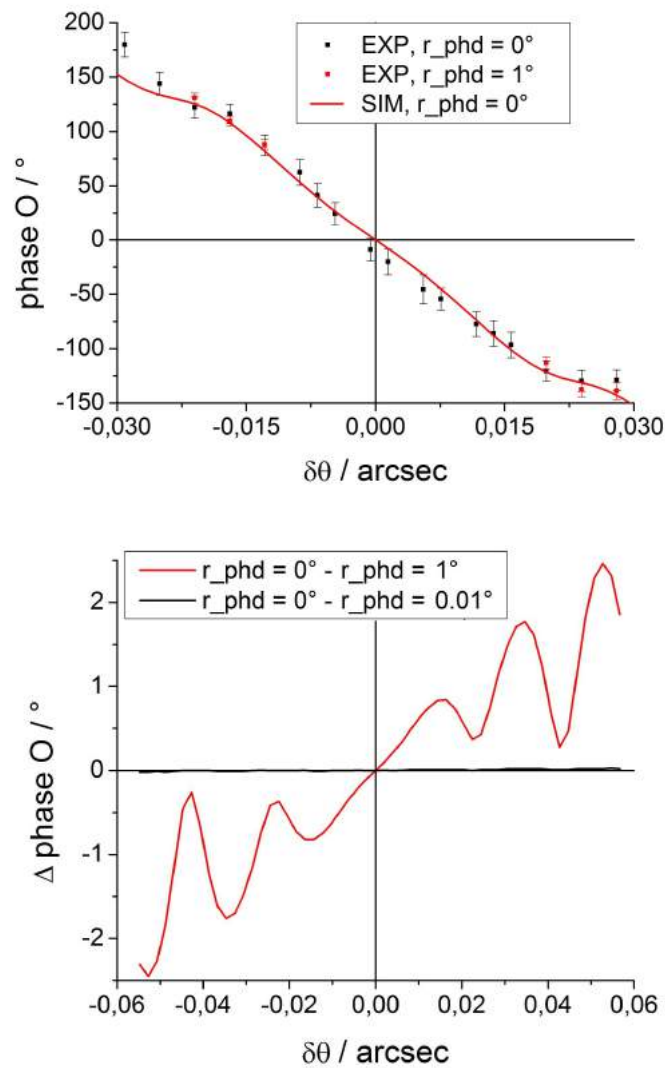


Figure 2.43.: (top) Laue phase measurement with a prism rotation offset at $r_{phd} = 0^\circ$ and 1° . The difference between the phases at the 2 angles is within the error (about $\pm 5^\circ$). (bottom) Laue phase calculation at $r_{phd} = 0^\circ$ and 1° . The difference is up to 2° , therefore the prisms have to be aligned within 0.01° . Same Parameters as in fig. 2.41.

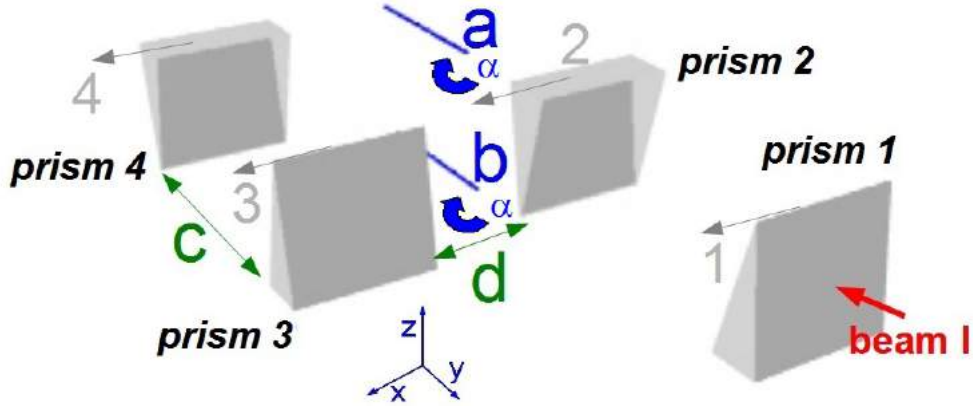


Figure 2.44.: Prism pair 1 (prism 1/2) and prism pair 2 (prism 3/4) rotate together around an axes parallel to y . This pivot (a) can be different in height z (b). (c) Length of prism pair: distance between two prisms comprising a pair, (d) distance between the pairs. (1)...(4) Shift of each prism in x -direction.

Geometry of the prisms

The last chapter dealt with a collective change of all prisms together, here we will investigate whether the geometry of the individual prisms or their mounting on the prism holding device have a significant influence on the Laue phase.

Distance between the prism pairs: the distance between the prism pairs does not change the Laue phase (fig. 2.44). A shift in x -direction³³ of only one of the four prisms (1)...(4) with the same common point of rotation shifts the Laue phase³⁴, but vanishes if the following prism of each pair (2/4) also shifts in x -direction.

Distance between two prisms comprising a prism pair: the length of the pairs is also marked in fig. 2.44, as calculations are restricted to two dimensions in IFMSIM, no influence on the length of the prism pair in beam I or II is visible, but in the experiment the prism pairs have to be the same length due to defocusing of the interferometer. If there would be only one prism in the interferometer (prism 1), its y -position has an influence on the shape and slope of the phase, but this is compensated by the following prism (prism 2).

Prism apex angle β : the influence on the Laue phase by a deviation $\Delta\beta$ of only one prism angle from the nominal angle $\beta = 25^\circ$ is given in fig. 2.45 for $\Delta\beta = 0.01^\circ$ and 0.001° . The front prisms (prism 1 or 3 or its combination) show a decreasing phase in positive $\delta\theta$ direction, while the back prisms (prism 2 or 4 or its combination) invert the sign of the slope. Furthermore, if both prisms in pair 1 deviate simultaneously by $\Delta\beta = 0.01^\circ/0.1^\circ$ the Laue phase changes by $\Delta\phi_{Laue} = 0.1^\circ/1^\circ$. Other combinations (prism 2 and 3 or 1 and 4) of simultaneous prisms apex angle changes, results in an asymmetric phase behavior (fig. 2.45). On the other hand, a simultaneous change of all prism angles together of $\beta = 0.01^\circ$ changes the Laue phase only up to 0.1° .

³³Note the IFMSIM parameter 'beam.center=1' can causes a x -deviation.

³⁴This shift is irrelevant for the used 'IN-OUT measurement'.

The conclusion is that the prism fabrication has an important influence on the Laue phase, each of the angles has to be accurate by at least 0.0005° for an exact Laue phase measurement ($< 0.1^\circ$). A prism geometry measurement in Ref. [30] shows that the apex angle's accuracy is around 0.01° for each prism. Therefore a phase error of maximal 4° arises here. The intensity and contrast show an influence for deviations larger than $\Delta\beta = 1^\circ$ (fig. 2.46).

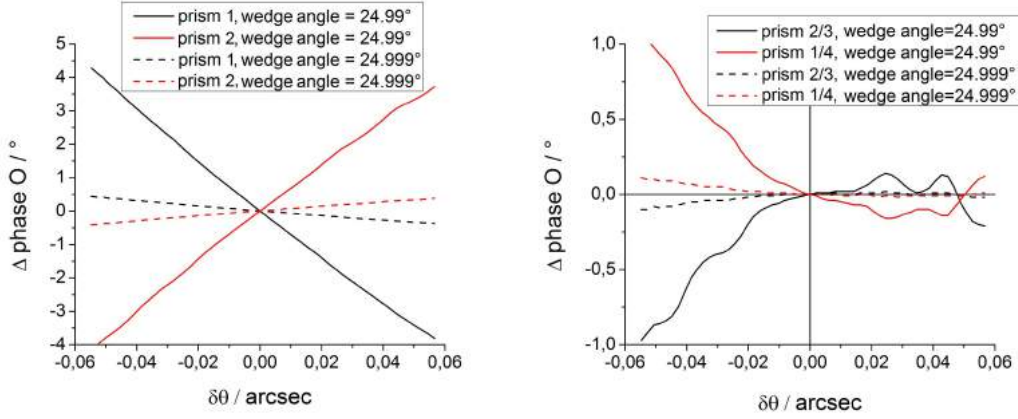


Figure 2.45.: Laue phase calculations with different prism apex angles. The phase difference with respect to the Laue phase for the case where all prisms are 25° is shown. (left) Only one of the 4 prisms has 24.99° (or 24.999°). (right) Only 2 prisms at diagonal positions have 24.99° (or 24.999°).

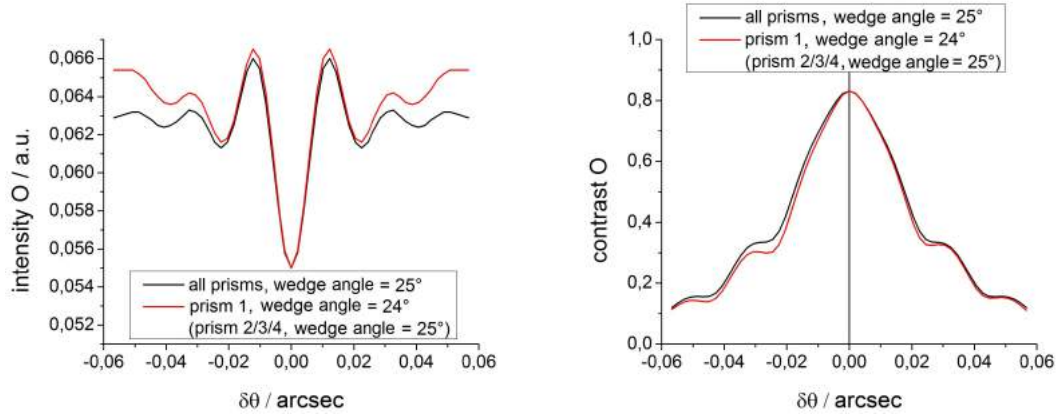


Figure 2.46.: Intensity (left) and contrast (right) calculations with different prism angles. The prism angles are 25° except for a single one which then has 24° .

Prism pairs not parallel, rotation around y-axis: this prism misalignment addresses a mounting of one of the prism pairs with an α -offset. The Laue phase, contrast and intensity curve will be shifted by a certain $\delta\theta$ value (fig. 2.47). If pair 1 has an offset of $0.1^\circ/1^\circ$, the Laue phase changes up to $2^\circ/20^\circ$. Each prism pair is cut from a single piece of Al, but if it is twisted (only one prism would be rotated against the others³⁵) this changes the Laue phase according to fig. 2.48. The prism rotation offsets of individual prisms (left) and combinations of prisms results in an asymmetric phase

³⁵The pairs are mounted on the prism holding device with a screw, where strains are possible.

change (right). To match with the $\delta\theta$ centered Laue phase the pairs have to be parallel within $< 0.01^\circ$ and the individual prisms $< 0.001^\circ$.

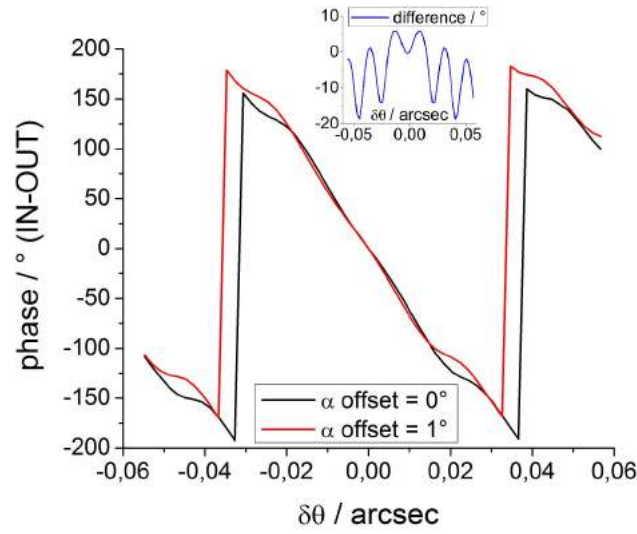


Figure 2.47.: Influence on the Laue phase due to an α -offset of 1° between the prism pairs. The inset shows the difference to the exact mounting (α -offset=0).

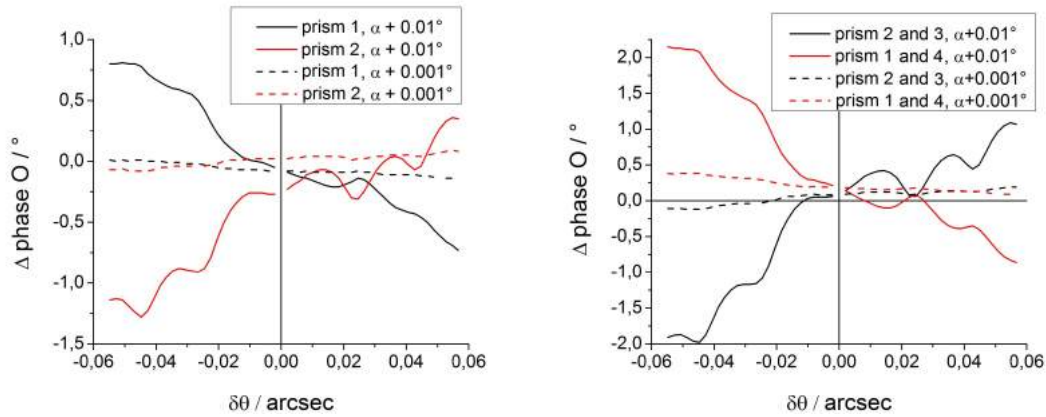


Figure 2.48.: Laue phase with different additional α -rotation offsets. (left) Only prism 1 or 2 have an offset. (right) Only prism 1 and 4 (or 2 and 3) have an offset.

The intensity and contrast do not deviate at this offset values, but fig. 2.49 shows the asymmetric intensity and contrast for a large offset. This diagrams are interesting regarding the $\delta\theta$ -shift from chap. 2.3, in particular the curve shape resembles the measured curves in fig. 2.12 (smaller contrast width, difference in intensity peak heights left and right from $\delta\theta = 0''$); however such a large geometry error does not occur in our prism pairs.

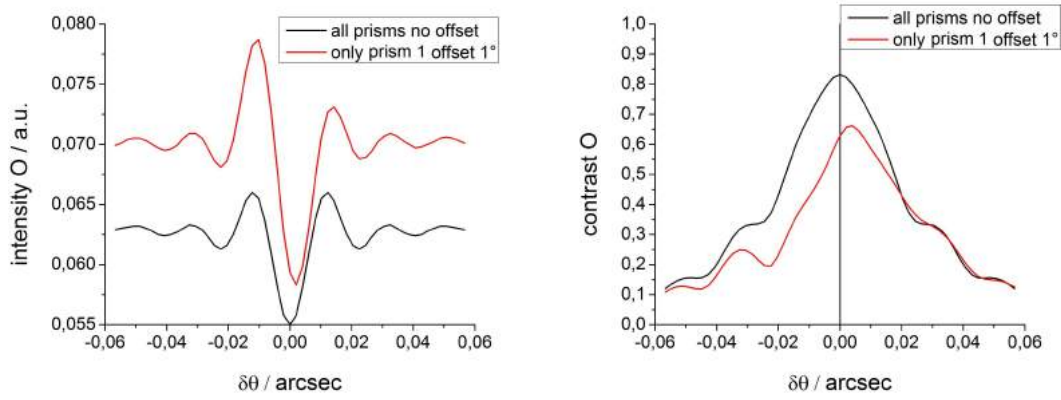


Figure 2.49.: Intensity (left) and contrast (right) calculations for an additional α -rotation offset of only prism 1.

Prism misalignment, rotation around the x-axis: similar to the $slope_{phd}$ angle for all prisms, here the individual³⁶ prisms are tilted (fig. 2.40). The influence of a change of only one prism slope from the nominal angle (0°) of all other prisms on the Laue phase is given in fig. 2.50. The front prisms (only prism 1 or 3 or its combination) shows a decreasing phase in positive $\delta\theta$ direction, while the back prisms (prism 2 or 4 or its combination) invert the sign of the slope. If both prism slopes in pair 1 change by $1^\circ/0.1^\circ$, the Laue phase then changes by $\phi_{Laue} = 2^\circ/0.2^\circ$. In our case the alignment accuracy between the two prism pairs is less than 0.1° , which is sufficient for a Laue phase measurement accuracy less than 0.1° . Other combinations of prisms (prism 2 and 3 or 1 and 4) result in an asymmetric phase behavior as shown in fig. 2.50.

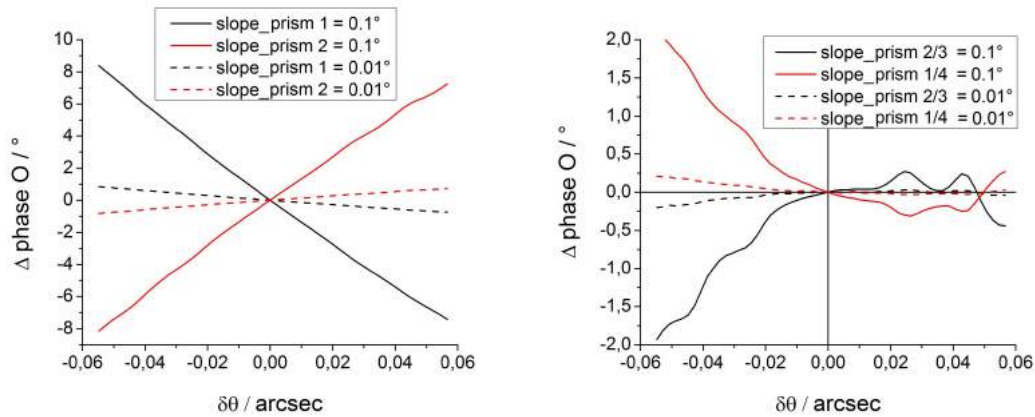


Figure 2.50.: Laue phase calculation with different prism slope angles. The difference with respect to the Laue phase for the case where all slopes are 0° is shown. (left) Only one prism (prism 1 or 2) has a different slope angle alignment. (right) Only prisms at diagonal positions have simultaneously a different slope angle.

³⁶Each prism pair is cut from one single Al piece, only a deformation due to the mounting screw can change this angle.

Hence, the prism alignment has an important influence on the Laue phase. The intensity and contrast curve only show an influence at large (5°) individual prism slope deviations.

Prism misalignment, rotation around the z-axis: similar to the r_{phd} angle for all prisms (fig. 2.42), here the individual³⁷ prisms are rotated. If both prisms in pair 1 are rotated by $1^\circ/0.1^\circ$ the Laue phase changes by $2^\circ/0.2^\circ$. Fig. 2.51 shows the Laue phase if only one prism would be rotated. If this rotation is performed by one of the front prisms (prism 1 or 3) then an increasing slope in positive direction arises, while the back prisms (prism 2 or 4) invert the sign of the slope. Other combinations of prisms (prism 2 and 3 or 1 and 4) result in an asymmetric phase behavior. For an accurate Laue phase measurement ($< 0.1^\circ$), the prism pairs have to be parallel within 0.05° . In the experiment a phase error arises here of about 1° . The intensity and contrast show an influence at large deviations of around 5° .

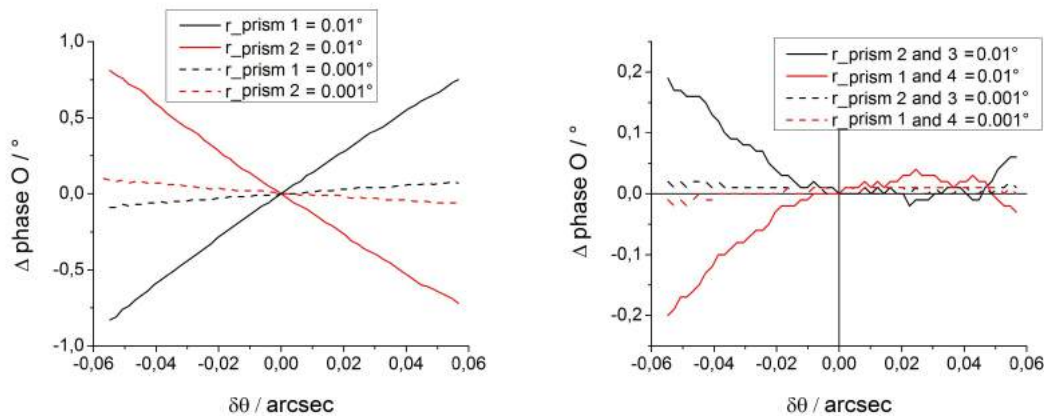


Figure 2.51.: Laue phase calculations with individually rotated prisms (similar to r_{phd}). The difference with respect to the Laue phase for the case where all prisms have 0° is shown. (left) Only a single prism (prism 1 or 2) is rotated. (right) Only prisms at diagonal positions are rotated.

Summary

In this chapter the following prism parameters were investigated for a possible influence on the Laue phase, intensity, and contrast:

- a tilt of the prism holding device in forward direction ($slope_{phd}$, fig. 2.40)
- a rotation of the prism holding device in the x-y plane (r_{phd} , fig. 2.42)
- the pivot of all prisms for the ' α -rotation' (fig. 2.44)
- the geometry of the individual prisms

Tab. 2.10 lists prism parameters with an influence on the Laue phase. This phase change is evaluated at the Pendelloesung plateaus. For an accurate Laue phase measurement ($\Delta\phi_{Laue} < 0.1^\circ$) with this setup, the prism holding device (phd) angles must be known

³⁷The two prism pairs are mounted separately on the prism holding device.

with an accuracy of around 0.01° , which is not possible in our setup and a phase error of approximately 1 degree arises for this *phd-angles*. In our experiment two individual prisms (prism n) are cut from a single Al block, therefore an alignment has to be performed only between the prism pairs, within about $r_{pair} = 0.05^\circ$. As in the experiment this angle is $r_{pair} = 0.1 \dots 0.5$ degrees, a phase error of about $\Delta\phi_{Laue} = 1^\circ$ results.

Table 2.10.: Due to the change of prism parameters, the Laue phase varies at specific $\delta\theta$ values (1st and 2nd plateau); phd... prism holding device (all prisms), prism n... individual prisms.

parameter	mismatch	1 st plateaus	2 nd plateaus
$slope_{phd}$	0.5°	0.75°	1°
$slope_{prism\ n}$	0.01°	0.4°	0.7°
r_{phd}	1°	1°	2°
$r_{prism\ n}$	0.01°	0.4°	0.7°
$apex\ angle_{prism\ n}$	0.001°	0.2°	0.4°

2.4.7. Wavelength

Next we investigate the influence of the wavelength on the Laue phase. Changes between different Bragg peaks as well as wavelength changes within one Bragg peak are considered. The wavelength is selected with a monochromator and six silicon prisms, as explained in chap. 2.2.1. Note that a new monochromator adjustment changes the wavelength slightly: $\theta_B = (45 \pm 0.25)^\circ$. This uncertainty in the Bragg angle is equal to a wavelength of $\Delta\lambda_{adjust} = \pm 0.012 \text{ \AA}$ for the (220) case and $\Delta\lambda_{adjust} = \pm 0.006 \text{ \AA}$ for the (440) case. The wavelength distribution at S18 is of the order $\Delta\lambda_{distr}/\lambda \approx 10^{-3} \dots 10^{-2}$.

Measurement of the wavelength

For general information concerning the wavelength measurement in neutron interferometry see [37]. There, the angle between dispersive (lattice planes of two crystals are not parallel) and non-dispersive (lattice planes parallel) interferometer positions is measured, which is twice the Bragg angle. Here we will test diffraction gratings in front of the interferometer. The gratings are just mounted on the aperture, therefore this method is very simple to handle. Two diffraction gratings with $16 \mu\text{m}$ and $17 \mu\text{m}$ spacing, respectively, have been used (fig. 2.52).



Figure 2.52.: Photography of the used phase diffraction grating with $g=16 \mu\text{m}$ spacing (left) and the absorption diffraction grating with $g=17 \mu\text{m}$ spacing (right).

In order to measure the diffraction peaks produced by this gratings, the interferometer is rotated around the Bragg condition (rocking curve, fig. 2.34). A comparison of the rocking curve without and with the grating is given in fig. 2.53 (left). For both Bragg reflections (220) and (440) the first order diffraction peaks produced by the grating are visible. To obtain narrow peaks for the determination of their maximum positions, the transmitted beam after blade 1 is blocked.

The measurements are repeated with the $17 \mu\text{m}$ grating and a longer counting time per point. The result is given in fig. 2.53 (right). Only in the (440) case the diffraction peaks are visible.

The positions of the individual intensity peaks are determined by 5 Gauss-curve fits as shown in fig. 2.54. The *rocking angle* $= 0''$ is now centered where the (440) peak maximum without the grating is located. From the peak-positions one can determine

the wavelengths with the equation [38]:

$$\lambda = g \frac{\sin \phi_{n'}}{n'} \quad (2.30)$$

The new diffraction maxima due to the presence of the grating, are located now at the angles $\phi_{n'}$, where n' represents the diffraction order.

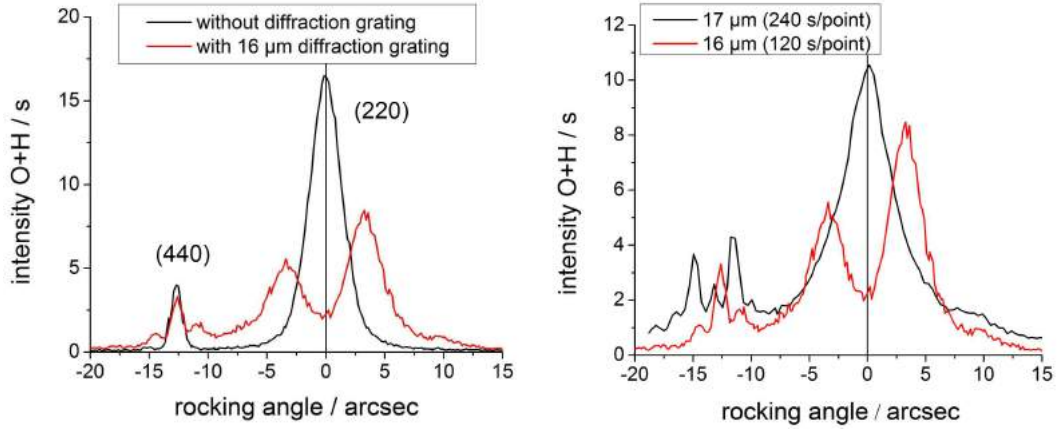


Figure 2.53.: Rocking curve without and with 16 μm diffraction grating in front of the IFM (left). Rocking curve with 16 μm and 17 μm grating (right).

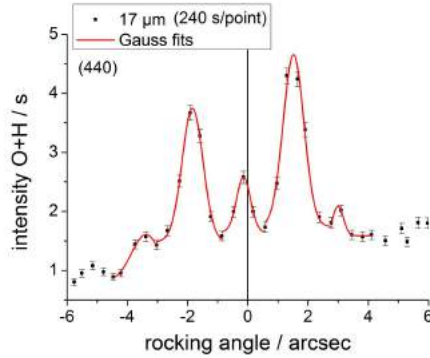


Figure 2.54.: Detail of the (440) Bragg peak from fig. 2.53 (right) with fits to a Gaussian (to determine the peak-positions).

The result is $(1.35 \pm 0.04) \text{ \AA}$ for (440). This value can be used to calculate the wavelengths of the other reflections: 2.71 \AA for (220), 0.90 \AA for (660), and 0.68 \AA for (880).

Laue phase

The Laue phase changes its behavior with the wavelength or order of reflection, according to eq. 2.13. A direct comparison of the phase, calculated with the (220) to (660) Bragg peaks is shown in fig. 2.55, the different phase slopes are visible. The positions of the plateaus move closer to $\delta\theta = 0''$, their positions are listed in tab. 2.11 and scale with the order of reflection³⁸.

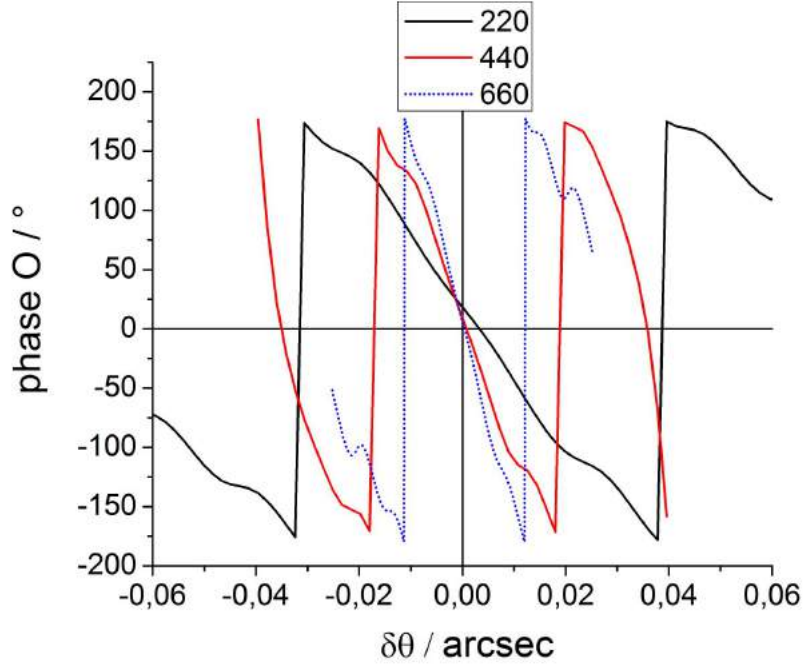


Figure 2.55.: Laue phase for different Bragg peaks. Calculated with the Bragg monochromator function, Darwin width = 1 and real I geometry.

Table 2.11.: Pendelloesung plateau positions in arcsec for several Bragg peaks.

Bragg peak	calculated $\lambda / \text{\AA}$	1 st plateaus	2 nd plateaus
(220)	2.72	$\pm (0.02 \dots 0.03)$	$\pm (0.04 \dots 0.05)$
(440)	1.36	$\pm (0.01 \dots 0.015)$	$\pm (0.02 \dots 0.025)$
(660)	0.91	$\pm (0.006 \dots 0.009)$	$\pm (0.013 \dots 0.016)$
(880)	0.68	$\pm (0.0045 \dots 0.008)$	$\pm (0.013 \dots 0.016)$

The Laue phase is calculated for different wavelengths. The corresponding values at the first and second Pendelloesung plateaus are summarized in tab. 2.12. $\Delta\lambda = 0.03 \text{ \AA}$ is approximately the accuracy of the wavelength determination from the diffraction grating measurement. Additionally, calculations with $\Delta\lambda = 0.00001 \text{ \AA}$ are listed as well. With the diffraction grating measurement accuracy, it yields a change of the phase of

³⁸For our prism setup two (220) / one (440) pairs of plateaus at each side of $\delta\theta = 0''$ are visible.

2. Laue phase

about 1° for the 1^{st} and 6° for the 2^{nd} plateaus (220). Hence, for an exact Laue phase measurement with our setup, the wavelength has to be known very accurately.

Table 2.12.: Laue phase ϕ change due to a wavelength uncertainty of 0.03 \AA and 0.00001 \AA for several Bragg peaks. Those phases are evaluated for 'real I' geometry (Darwin width = 1) at specific $\delta\theta$ values (1^{st} and 2^{nd} plateaus).

Bragg peak	$\lambda / \text{\AA}$	1^{st} plateaus	2^{nd} plateaus
(220)	2.71551	0°	0°
	-0.03	1°	6°
	-0.00001	0.02°	0.05°
(440)	1.35776	0°	0°
	-0.03	9°	36°
	-0.00001	0.05°	0.05°
(660)	0.90517	0°	0°
	-0.03	5.2°	20.5°
	-0.00001	0.03°	0.11°
(880)	0.67888	0°	0°
	-0.03	19.4°	277°
	-0.00001	0.16°	2.14°

2.4.8. Scattering length

The neutron is assumed to be electrically neutral, but has an internal charge structure because it consists of quarks. This results in an electrical influence on neutron-scattering experiments, an overview of this and further interactions are given in [39]. The scattering length b is of fundamental interest in areas like astro and nuclear physics. It describes the interaction of the neutron with an atom. In this chapter we study the influence of the scattering length on the Laue phase. The main question concerns the possibility of extracting fundamental quantities such as the neutron-electron scattering length [2], [5], [36], [40]. For this purpose, it is necessary to consider all systematic phase effects from the last sections.

Eq. 2.31³⁹ shows the atomic scattering length in detail, with the precisely known nuclear scattering length b_{nuc} and the momentum-dependent electrostatic neutron-electron scattering contribution [5],

$$b_{atom} = b_{nuc} + Z \cdot (1 - f(\vec{q})) \cdot b_{ne} \quad (2.31)$$

where the proton number is $Z = 14$ for Si and $f(\vec{q}) = 1/\sqrt{1 + 3(\vec{q}/q_0)^2}$ is the atomic form factor, \vec{q} is the momentum transfer of the scattered neutron $\vec{q} = 2\vec{k} \cdot \sin \theta_B$, and $q_0 = 0.19 \cdot Z^{1/3}$ nm, tab. 2.13.

Table 2.13.: Bragg peak, wavelength, momentum, atomic form factor.

Bragg peak	$\lambda/\text{\AA}$	$q/\text{\AA}^{-1}$	$f(q)$
(220)	2.7155	3.2722	0.6285
(440)	1.3578	6.5445	0.3746
(660)	0.9052	9.8167	0.2601
(880)	0.6789	13.0889	0.1980

While the nuclear part $b_{nuc} = 4.1507(2)$ fm is well known [50], for the neutron-electron part different measured values exist:

- Garching/Argonne: $b_{ne} = -0.00131(3)$ fm
- Dubna: $b_{ne} = -0.00159(4)$ fm

For the input in IFMSIM, the ratio b_{ne}/b_{nuc} is needed:

- Garching/Argonne: $b_{ne}/b_{nuc} = -0.000316$
- Dubna: $b_{ne}/b_{nuc} = -0.000383$

References are summarized in [40]. The total scattering length eq. 2.31 with these two b_{ne} values is depicted in fig. 2.56 as a function of the wavelength. In the inset, the difference between these two curves is shown, which increases with smaller λ .

³⁹Note the sign after b_{nuc} , - in [40].

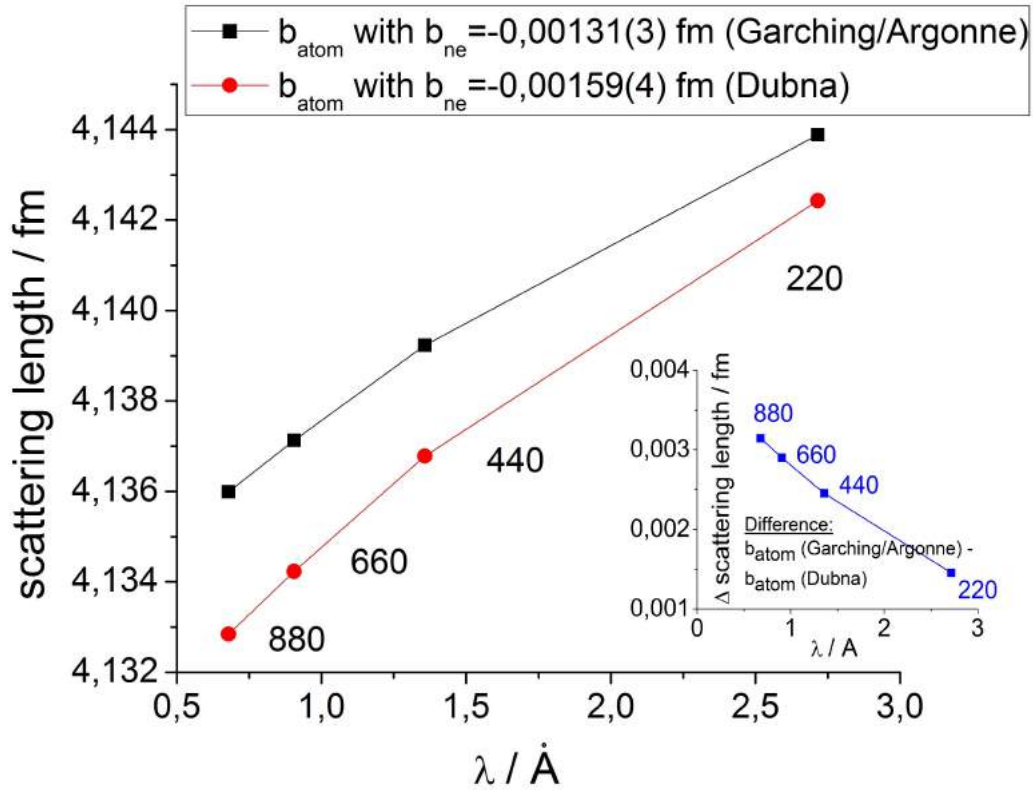


Figure 2.56.: Atomic scattering length with 2 different values of b_{ne} . The inset shows the difference, which is increasing with the order of reflection.

As the scattering length is part of the Laue phase formula eq. 2.13, the influence of b on the Laue phase is investigated in this chapter. In the following, calculations are performed with the rounded Garching/Argonne and Dubna ratios $b_{ne}/b_{nuc} = -0.0003$ and -0.0004 . With each of these values a Laue phase is calculated. The difference of the Laue phases $\Delta\phi$ results therefore from the two different b_{ne} values. In fig. 2.57 $\Delta\phi$ is given for the ideal interferometer as a function of the sample thickness (blade 3 and 4). The sample thickness change, relative to 3 mm is depicted. One can see that with a sample thickness of about $3 \text{ mm} \pm 20 \mu\text{m}$ the phase sensitivity can be doubled.

The results for the interferometer with the 'real' geometry are listed in tab. A.6... A.11. The calculations are performed for different Bragg peaks and for all Pendelloesung plateaus (prism rotation up to $\alpha = 90^\circ$). In comparison to the reached phase accuracy from the different parameters in the last sections, one can say conclusively that this effect is too small for this method, even if the contrast in the measurements reaches the theoretical maximal value.

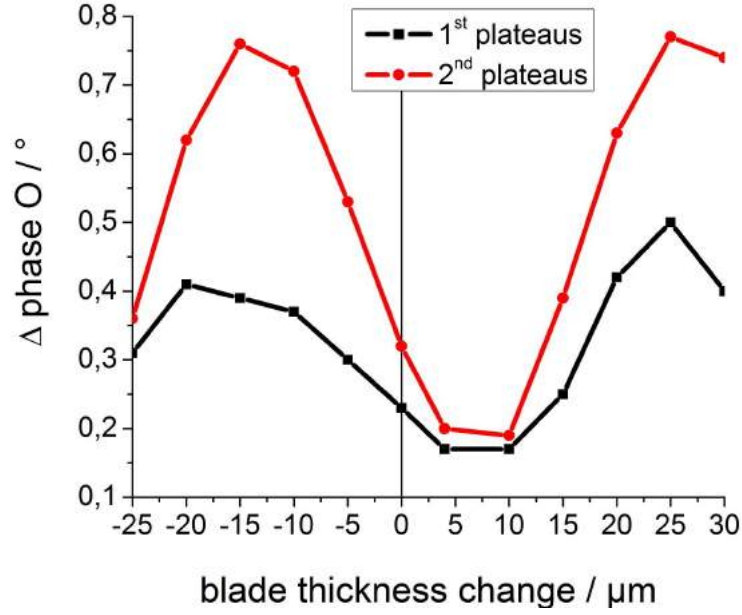


Figure 2.57.: Scattering length b_{ne} influence on the Laue phase. The sample thickness varies from the 3 mm ideal interferometer, Bragg peak (220). Evaluated at the 1st and 2nd plateaus.

Scattering length b_G

A proposal by Greene [6] extends eq. 2.31 with an additional short range gravity term $f_G(\vec{q}) \cdot b_G$, whereas $f_G(\vec{q}) = 1/(1 + (\vec{q}\lambda_G)^2)$, and λ_G is the effective range of gravitational interactions. Important is the different wavelength behavior, to distinguish between the two contributions from b_{ne} and b_G . However the influence on the Laue phase would be expected smaller than that of b_{ne} .

Debye-Waller factor

Another influence on the scattering length is caused by the temperature T, described by the Debye-Waller factor: $b_{atom} \cdot \exp^{-\vec{q}^2 \cdot k_B T / M \omega^2}$, where a harmonic oscillation of the atoms with mass M and frequency ω is assumed, $k_B = 1.3806488(13) \cdot 10^{-23}$ J/K. The uncertainty of the Laue phase created by the Debye-Waller factor is about two times larger than that from b_{ne} , and increases with the order of reflection [30].

2.5. Relative Laue method

The disadvantage of the Laue phase measurement-method in the last chapter is the fast decrease of the contrast with increasing beam deflection. To maintain the contrast, another method is investigated here [4]. Fig. 2.58 gives an idea⁴⁰ of this 'relative Laue phase', where the phase is obtained from a rotation of blade 3 followed by an independent rotation of blade 4. However the relative Laue phase is a result of a simultaneous blade rotation (one blade rotates with an additional offset angle relative to the other blade). The rotation of the second blade should compensate some of the arising phase change due to the other blade rotation, which causes the contrast reduction. Therefore a larger $\delta\theta$ range is in principle possible.

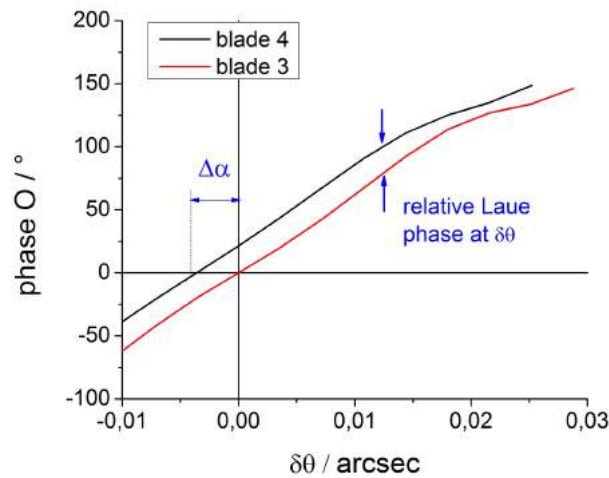


Figure 2.58.: Relative Laue phase measurement principle. Calculation of the Laue phase for blade 3 rotation only and blade 4 rotation only. The blade 4 rotation is shifted with a constant offset $\Delta\alpha$. The arrow shows the difference at a specific $\delta\theta$ – the relative Laue phase in principle.

As the blade rotation is equal to the beam deflection with prisms, the necessary setup modification is shown in fig. 2.59, both prisms are now deflecting the beam in front of the blades 3 and 4 respectively (one prism pair rotates with $\alpha + \Delta\alpha$).

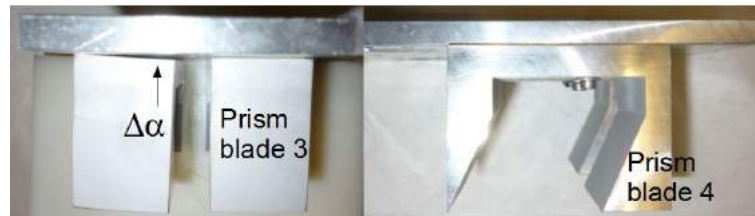


Figure 2.59.: Both prism pairs are mounted over the blades 3 and 4. The blade 4 rotation has a constant offset $\Delta\alpha$.

⁴⁰Note that the phase difference here is different from the relative Laue phase, due to a changing geometry when the other sample rotates simultaneously.

Offset value $\Delta\alpha$: the question arises, which optimal offset value should be selected. In fig. 2.60 the influence on different offset angles is given. One can see the phase for $\Delta\alpha = 1^\circ, 2^\circ$, and zero offset. For a better comparison, for each phase value the corresponding value at $\delta\theta = 0''$ is subtracted. The phase change is stronger with increasing offset, however the corresponding contrast decreases with increasing $\Delta\alpha$ (about 50 % for $\Delta\alpha = 5^\circ$). Because the second rotating blade compensate less and less of the arising phase distribution. So for the measurement, an optimal $\Delta\alpha$ value of about 1° has been used. Note that with this relative Laue method, the contrast remains over the $\delta\theta$ range except of the small asymmetry in $\delta\theta$, which is caused by the imperfect IFM geometry.

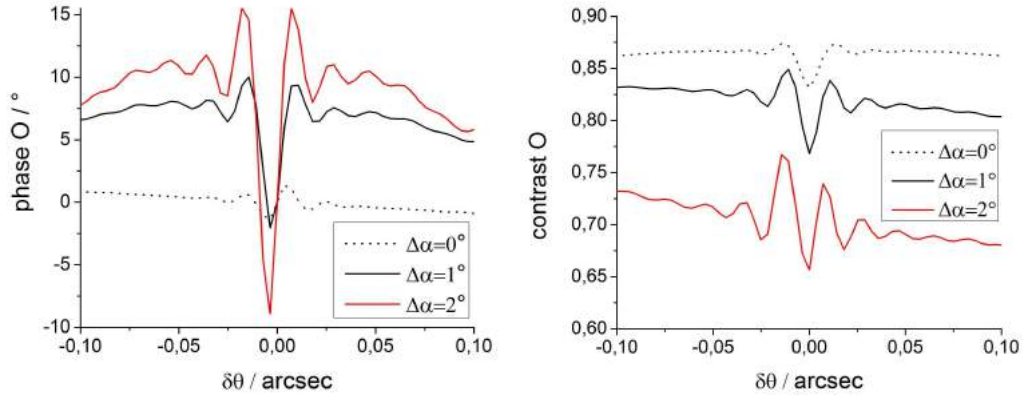


Figure 2.60.: Different offset values $\Delta\alpha$. (left) Calculated relative Laue phase (minus phase at $\delta\theta = 0''$) and contrast (right). The increasing phase change with increasing offset, faces a decreasing contrast. Parameters: (220) Bragg peak, real I geometry.

Monochromator and beam divergence: fig. 2.61 depicts the relative Laue phase with different monochromator functions and beam divergences. The influence is smaller than in the last method (chap. 2.4.3: Bragg minus Gauss monochromator function: the phase difference is about 0.4° ; chap. 2.4.4: Darwin width 1 minus 3: up to $\Delta\phi_{Laue} = 1.2^\circ$).

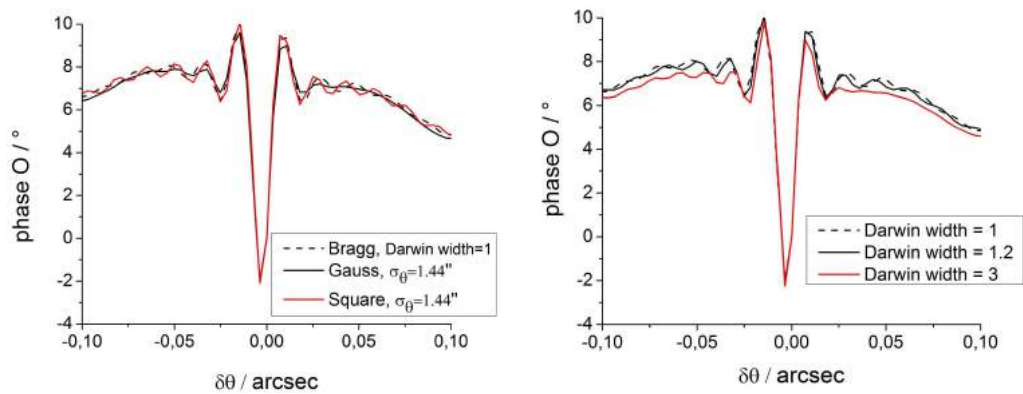


Figure 2.61.: Influence of the monochromator (left) and beam divergence (right) on the relative Laue phase. Same parameters as in fig. 2.60 and $\Delta\alpha = 1^\circ$.

The influence of the interferometer's geometry on this phase is given in fig. 2.64 and 2.65.

2.5.1. Scattering length

The influence of the scattering length on the relative Laue phase is shown for different interferometer geometries in fig. 2.62, and for different offset angles in fig. 2.63. The phase difference between $b_{ne}/b_{nuc} = -0.0003$ and -0.0004 yields about 0.1° . The geometry and $\Delta\alpha$ do not significantly change this value. The monochromator function and beam divergence have a negligible influence on this difference, too. Concerning the scattering length, this method does not show a better sensitivity than in chap. 2.4.8.

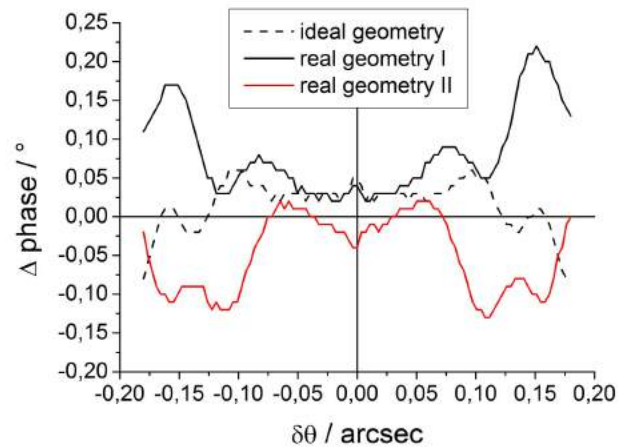


Figure 2.62.: Calculation of the influence of the interferometer's geometry on the 'relative Laue phase difference'. The phase difference occurring for assumed values $b_{ne}/b_{nuc} = -0.0003$ and -0.0004 is shown. Note the larger $\delta\theta$ range. Parameters: (220) Bragg, Darwin width 1, blade 4 plus 1 degree offset.

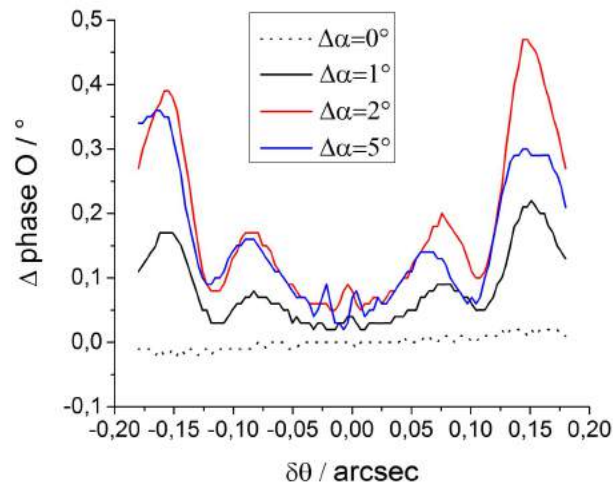


Figure 2.63.: Influence of the offset angle on the 'relative Laue phase difference'. Same parameters as in fig. 2.62 and real I interferometer geometry.

2.5.2. Measurement with the relative Laue method

(220) case

In fig. 2.64 the calculated phase, contrast and intensity of this setup is compared with the measurements for the (220) Bragg peak. The measured values are averages of about 3 to 14 interferograms (and 40 at $\delta\theta = 0.03667''$). The measurement of the phase (IN-OUT⁴¹) does not show a good agreement with the calculations, a remeasurement was not possible due to limited time. The monochromator and beam divergence modify the phase but can not explain this large deviation (fig. 2.61). The influence of the different interferometer geometries is also shown in the graphs, which can not explain the deviation. Note also that the $\delta\theta$ axis is not shifted here as in chap. 2.3. An important observation is that the contrast indeed does not decrease with $\delta\theta$.

(440) case

In fig. 2.65 the calculated phase, contrast and intensity of this setup is compared with measurements for the (440) Bragg peak. The measured values are averages of about 5 to 8 interferograms. Note that the $\Delta\alpha = 1.1^\circ$ offset is the same as in the (220) case, therefore the $\delta\theta$ beam deviation is different. Here for the (440) Bragg peak it is also demonstrated, that the contrast is not decreasing with increasing beam deflection.

Summary

With this method [30] it was possible to show that the contrast remains, while in the method in chap. 2.3 the contrast decreases with increasing beam deflection. Unfortunately, the influence of the scattering length is smaller than in chap. 2.4.8. In general the sensitivity to parameters like monochromator function and beam divergence is lower. A more accurate measurement of the relative Laue phase, needs more time due to challenging contrast conditions, for large interferometers on the S18 instrument.

⁴¹Phase at each α (IN) minus phase at $\alpha = 0^\circ$ (OUT).

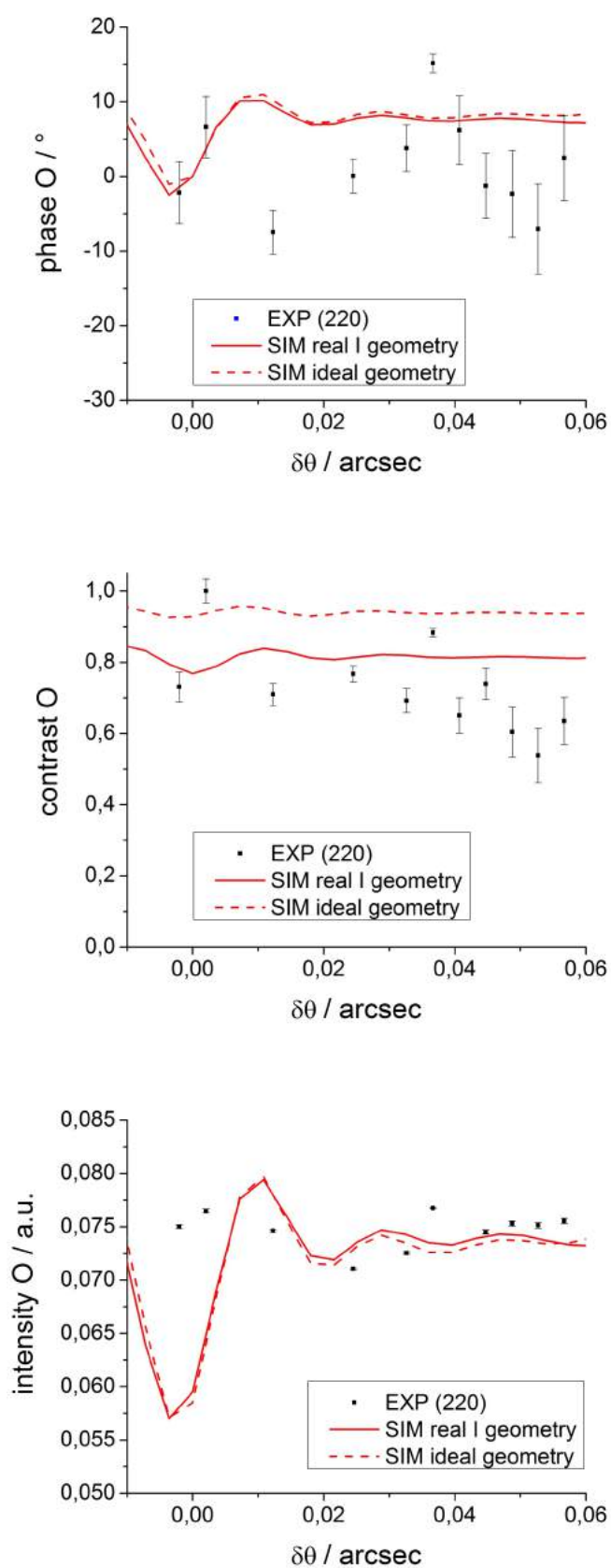


Figure 2.64.: Relative Laue phase, contrast, and intensity for the (220) Bragg peak ($\Delta\alpha = 1.1^\circ$).

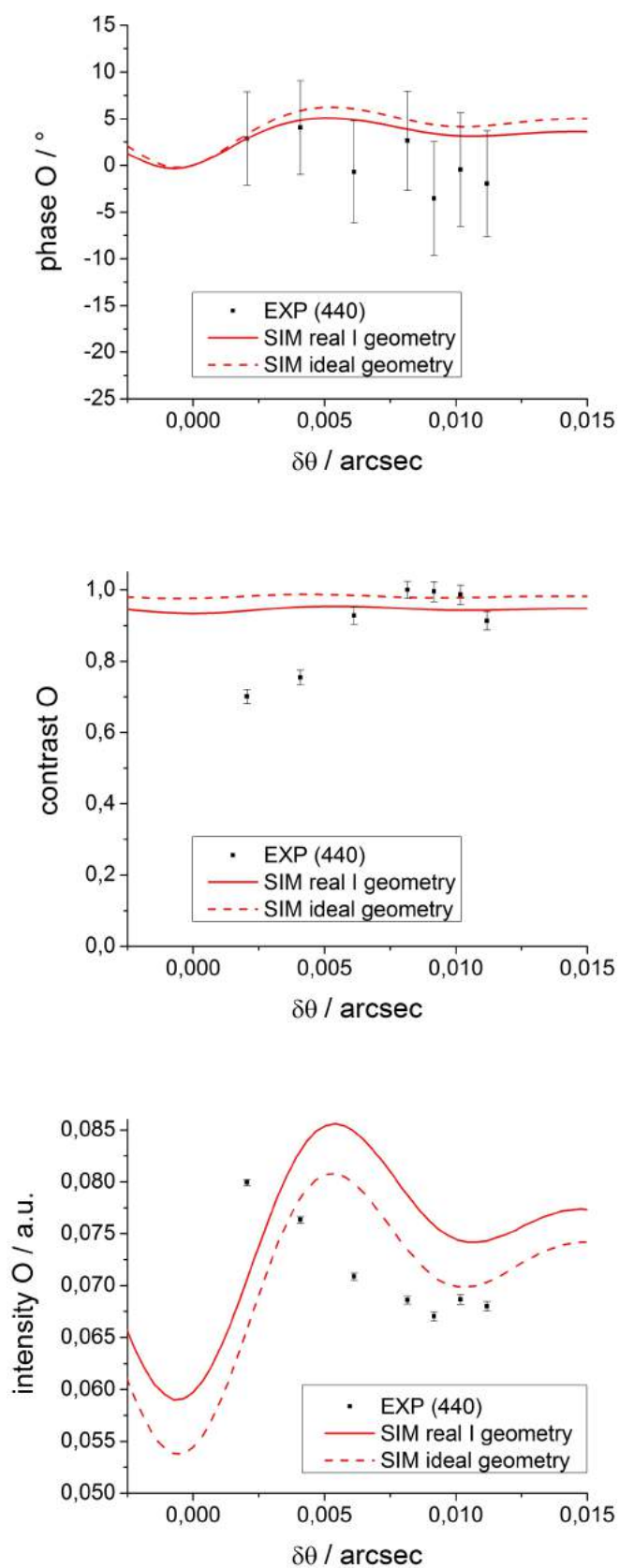


Figure 2.65.: Relative Laue phase, contrast, and intensity for the (440) Bragg peak ($\Delta\alpha = 1.1^\circ$).

3. Preparation of a new interferometer

Our further planed neutron-experiments require a larger area enclosed by the interfering beams and a different sample blade, than the interferometer used so far in the last chapter. Moreover, the perturbations due to crystal bending could be reduced with a thicker basis. Therefore, within this work a new neutron interferometer is fabricated with our co-operation partner at the 'Physikalisch- Technische- Bundesanstalt' (PTB)¹. The non-trivial preparation steps of the world's largest perfect-crystal interferometer are documented in this chapter. The possible applications, where the large area of the enclosed interfering beams can be of great value, are e.g. measurements of gravity induced phase effects (COW) and high angular resolution experiments. For this, a thicker sample is necessary to enhance the Laue phase slope.

3.1. Dimensions and key parameters

Fig. 3.1 shows the planed dimensions for this new interferometer. A minimum space is required for the phase shifter and the rotation range of the prisms, in particular the full length of our prism pairs, must fit into the second loop. The width of the IFM and therefore the beam separation, is limited by the ingot diameter (6 inch). The path length, beam separation and enclosed beam area are exceeding the dimensions of hitherto prepared interferometer crystals.

The key parameters are:

- very large dimensions: length 30 cm, path length 30 cm, largest interferometer
- large beam separation 6 cm: smaller tilt for COW experiments (reduce crystal bending)
- thick basis² 3.5 cm: to reduce disturbances
- small bottom contact surface 1.5 x 30 cm²: to reduce contact strains
- large areas of the enclosed interfering beams: 3 different loops (50 cm², 100 cm², 150 cm²) for COW measurements
- thick middle blades 1.5 cm: for high angular resolution experiments

The height of the lamellas is 2 cm, in the original version 4 cm.

¹U.Kuetgens et al., Bundesalle 100, 38116 Braunschweig, Div. 4.33 x-ray Optics

²In the original version 5.1 cm, see chap. 3.3.

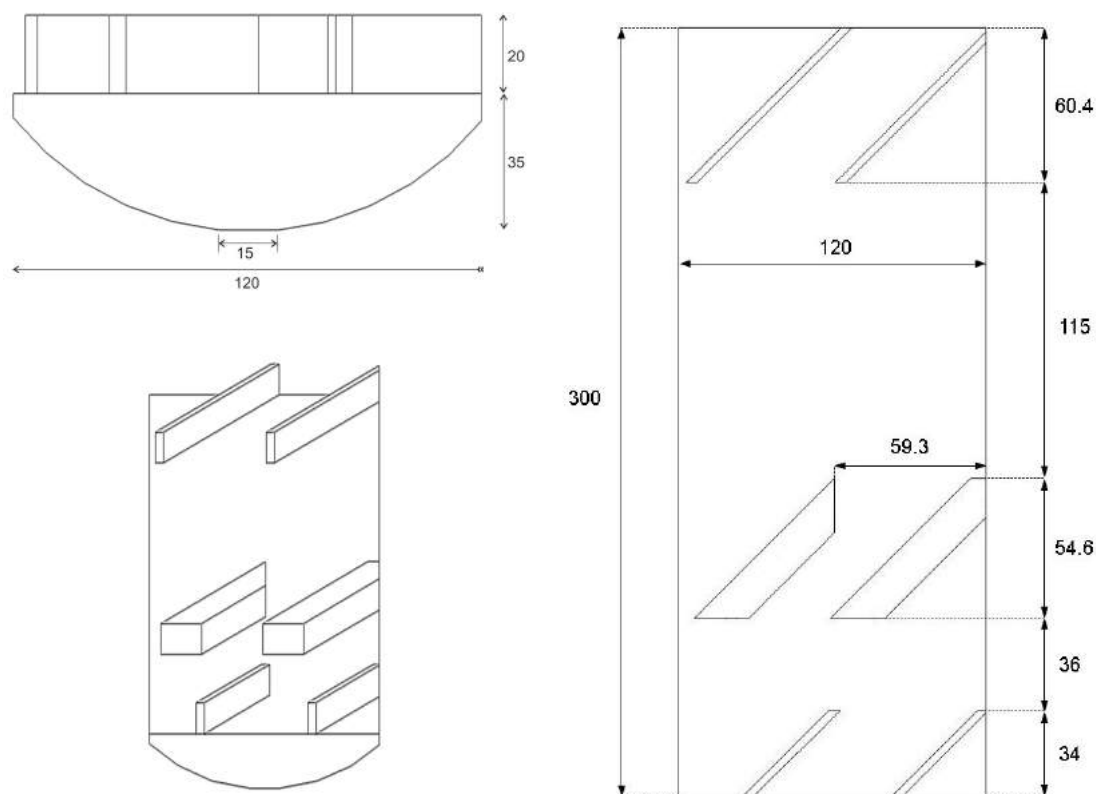


Figure 3.1.: Dimensions of the new interferometer (in mm). The lamella thickness is 3 mm and 15 mm. The design is optimized for the measurement purpose, space for the used prisms and phase shifter.

3.2. Preparation steps

The different stages of the machining of this crystal interferometer are presented in the following. Especially important is an accurate crystal orientation to the symmetric Laue-case as well as correct blade distances and thicknesses to yield a focused IFM. Furthermore, the damaged surface of the perfect-crystal during the cutting has to be removed with acid. Additionally a model of the interferometer has been produced³.

3.2.1. Silicon perfect crystal ingot

A crystal with less carbon and oxygen impurities and a lattice orientation, where the neutrons can travel along the ingot axis, is necessary. The parameters⁴ of the chosen 6 inch Si ingot (fig. 3.2) are listed in tab. 3.1.

³The IFM model is made of wood by Harald Huber (2013).

⁴According to Silchem Handelsgesellschaft mbH, Himmelfahrtsgasse 41, D-09599 Freiberg



Figure 3.2.: Silicon perfect crystal ingot before cutting at PTB.

Table 3.1.: Parameters of the Float-zone grown Si ingot (type n/phosphorus).

diameter	15.4 cm	orientation	(100)
length	40.8 cm	carbon concentration	$< 2 \cdot 10^{16} \text{ At/cm}^2$
weight	17.81 kg	oxygen concentration	$< 1 \cdot 10^{16} \text{ At/cm}^2$
resistivity	$> 2000 \text{ Ohm cm}$	costs	14796 €

3.2.2. Cutting

We start the work on the Si ingot at the PTB with the length reduction from 40.8 cm to the interferometer length plus additional 3 mm, which is removed afterwards by an oriented grinding. The mounting of the crystal in the cutting-, grinding and orientation-machines is performed with a metal support, where the crystal sticks with a brown glue (Crystal band 590 from KAGER GmbH). The gluing and ungluing process is done in an oven at 150°C for 4 hours. In fig. 3.3 the further stages of the cutting are presented. A cut along the ingot axis removes the material above the lamellas (fig. 3.3(a)). Then a small basis area on the other side is created, the left and right ingot curve is removed as well. After four parallel cuts (fig. 3.3(b)), the wire saw removes the material between the lamella pairs (fig. 3.3(c)). Then, the lamellas are cut out with an additional thickness of 2 mm (fig. 3.3(d)), which is removed afterwards by the grinding process. The not-used material between these cuts is removed again with the wire saw. The cutting of the ingot is done with machines from 'Meyer Burger', with an 1.5 mm thick bronze bonded diamond wheel (D126, 1500 r/min, forward speed 5 mm/min) and a 0.3 mm thick diamond coated wire saw (wire tension 20 N, forward speed 0.381 mm/min). For the cooling and removing of the Si dust during the cutting process, water with 5% Grindex 10 (Blasa) oil is used.

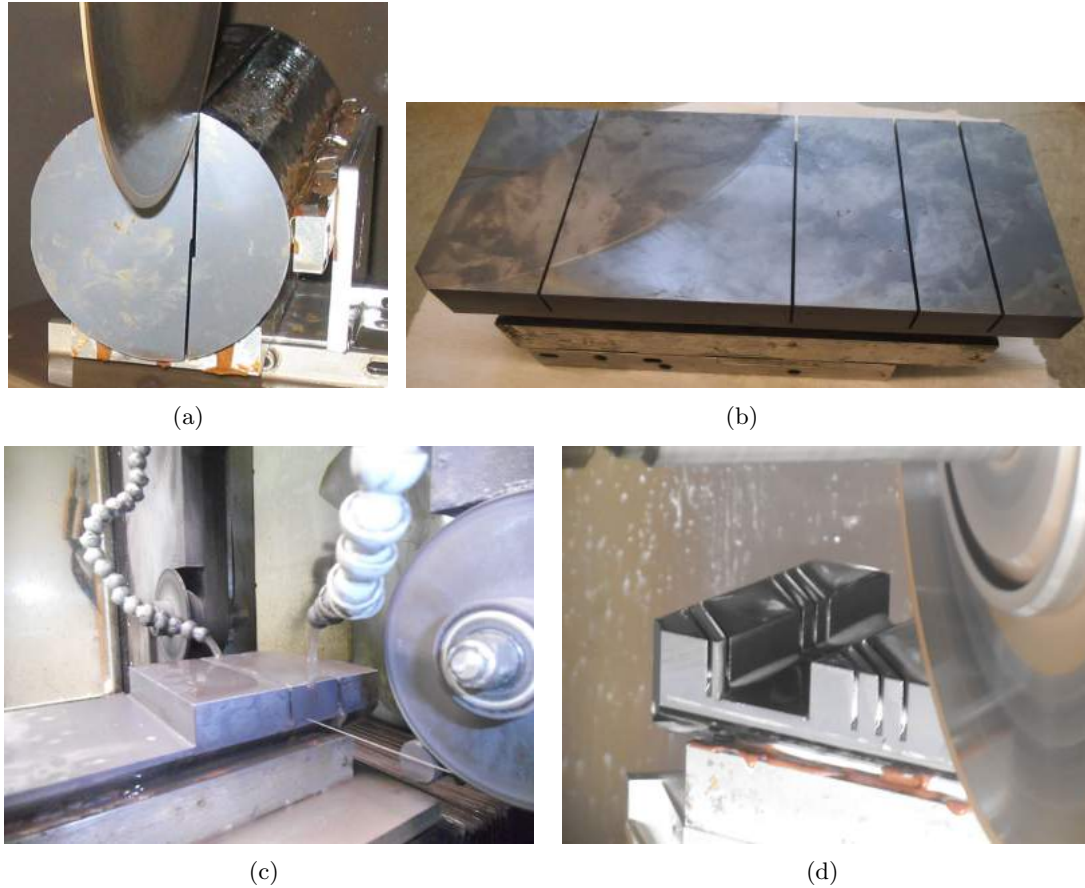


Figure 3.3.: Cutting stages of the new interferometer. (a) Lengthwise cut of the ingot, (b) lamella pair (c) diamond coated wire saw, (d) lamella cutting.

3.2.3. Orientation

The lamella surfaces have to be perpendicular to the lattice planes within about 30 arc-sec (symmetric Laue case, fig. 2.1), in order to yield a Laue phase accuracy of about 1° for $\delta\theta > 0.1''$ [30]. The correct orientation of the cutting and grinding process at every preparation step is performed with a x-ray diffractometer and an autocollimator (NIKON 6BLED), as depicted in fig. 3.4. The interferometer is placed on a rotatable table with a special metal holder. The radiation which comes from a silver source ($1 \times 1 \text{ mm}^2$, $\theta_B = 16.9378^\circ$, (440) Bragg peak), is detected at 4 positions of the interferometer (every 90°), if it is exactly orientated⁵. The second step is the mounting of an auxiliary mirror. It is aligned parallel to the cutting surface with an autocollimator. A similar autocollimator is at the cutting machine, where the interferometer can be aligned with the auxiliary mirror.

⁵The table has to be adjusted that the peak does not vanish during the rotation (fix detector position).

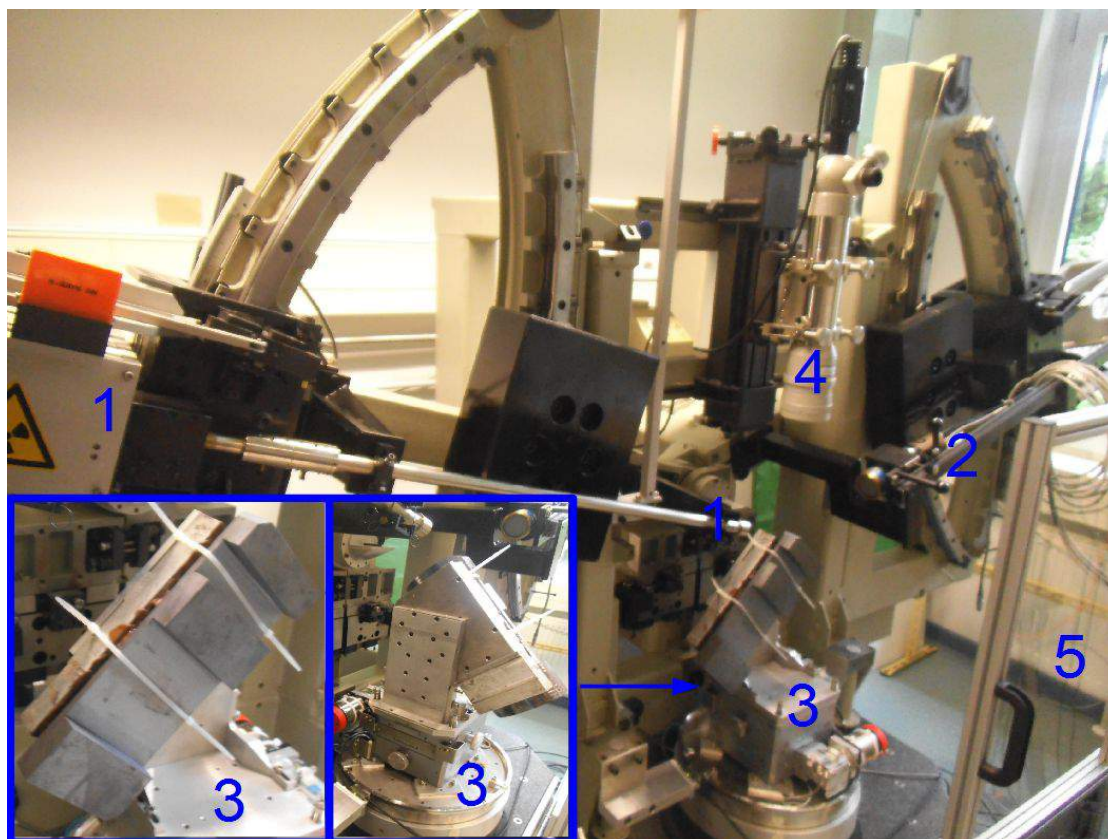


Figure 3.4.: Orientation of the crystal with a x-ray diffractometer at PTB. (1) Ag x-ray source, (2) detector, (3) rotatable table with the interferometer, the insets show a magnification of 3 as well as an additional rotation of 3 to 90° . (4) Autocollimator, optical method to determine the lattice plane surface angle. (5) Leaded glass for radiation protection. Accuracy of the diffractometer: $\pm 0.2''$, autocollimator: $\pm 1''$.

3.2.4. Grinding

The final blade thickness is obtained by the grinding process after the cutting. Also the surface-quality of the lamellas improved. The grinding is performed with the same machine from 'Meyer Burger', with a 9 mm thick bronze bonded diamond wheel (D126, 1500 r/min, forward speed 5 mm/min). First, only one surface of each blade is grinded. After the thickness-control, the second surface of the blades is grinded. The deviation of surface to lattice planes is $53.07''$ (compare chap. 3.2.3), measured with a non-contact sensor 'MG70 Mikro-Epsilon optoNCDT 2401'. Fig. 3.5 compares the surface of the cutted and the grinded blade 5 (neutron exiting side).

After grinding the metal support is separated from the interferometer in the oven as described above. The remainings of the glue can be removed with methanol⁶, afterwards the quality of the geometry was measured in Vienna. Tab. A.12 lists the blade thicknesses, measured at Rauch company. Due to this large thickness differences, this interferometer would be defocused (e.g. $29.5 \mu\text{m}$ between blade 2 and 6, at position 4).

⁶ CH_4O is toxic, documentation of the used amount is required.

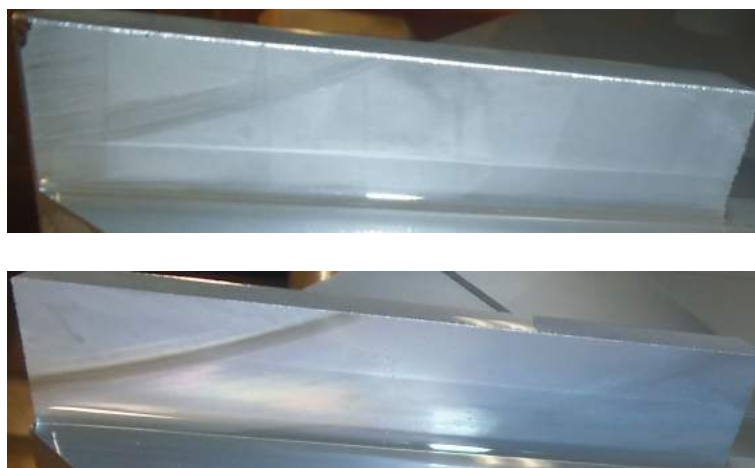


Figure 3.5.: Surface of the cutted (top) and grinded (bottom) interferometer lamella.

A fine-grinding at Rauch company was performed⁷. For this process, the interferometer is clued with 'Vinnapas(R)B 60' (at 145°C for 4 hours) at a glas plate mounded at a steel plate (fig. 3.6). This clue can easily be removed with acetone.

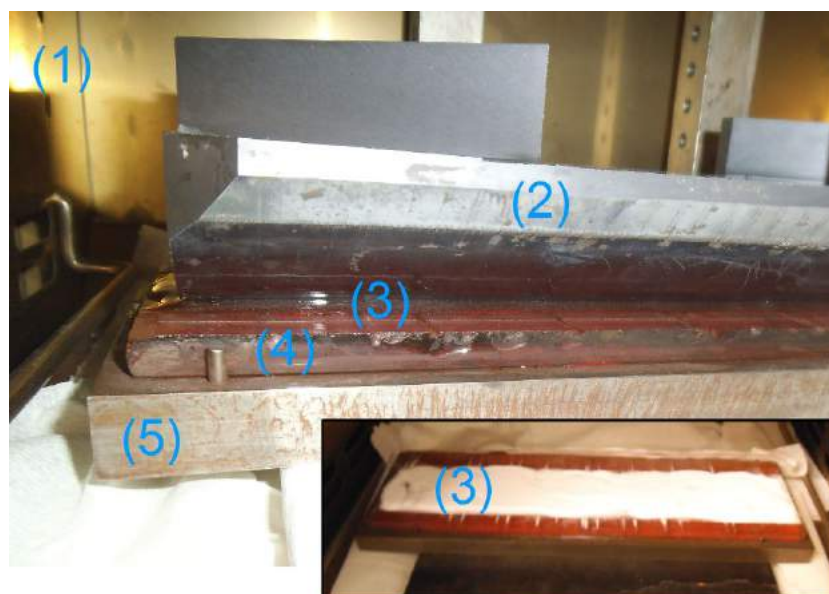


Figure 3.6.: Interferometer cluing. (1) Oven, (2) IFM, (3) clue after heating, (4) glas plate, (5) steel plate. The inset shows the clue powder before heating.

The subsequent geometrical measurement gives a better result, as listed in tab. A.13 (blade thicknesses) and tab. A.14 (blade distances). Input of this geometry values in IFMSIM results in a maximal visibility of about 70%.

⁷Only 18 mm (from the top) of the 20 mm blades are grinded.

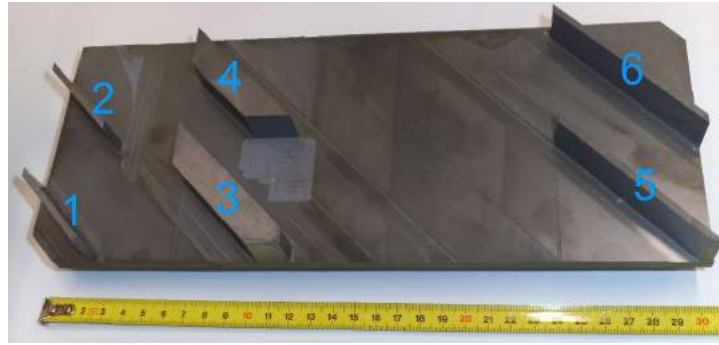
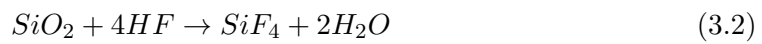
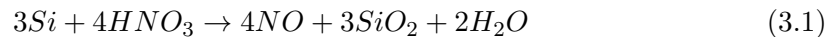


Figure 3.7.: Interferometer after grinding, with blade numbers.

3.2.5. Etching

The etching of the interferometer is done by our own, at the Institute of Atomic and Subatomic Physics in Vienna. With hydrofluoric and nitric acid (1:60⁸ of HF 40% and HNO₃ 65%⁹) the damaged perfect crystal structure (due to cutting and grinding) is removed. The etching depth is 20...30 μm depending on the grinding process. Equation 3.1 describes the oxidation of the silicon surface by the nitric acid. This is removed with the hydrofluoric acid:



Preparation of the laboratory, interferometer and the laboratory worker:

For the etching process a clean¹⁰ lab with an acid fume cupboard is required, fig. 3.10. Fig. 3.10(b) shows the etching reservoirs within a water vessel for cooling and a vessel with distilled water for the interferometer after etching. Furthermore, graduated jugs for mixing the acids and an additional acid supply during etching is needed. A fleece for acid accidents is prepared as well.

The cleaning of the lamella surface influences the etching process significantly. It is performed with a cosmetic tissue soaked in distilled water first, then in acetone. Afterwards, the interferometer is placed in an acetone bad for some hours. Before and after etching, the interferometer has to be weighed with a precision balance, to determine the mass loss Δm . The remove of the acetone before weighing is done with nitrogen (fig. 3.10(a)). Cloth gloves are used every time the interferometer is touched.

For the worker acid-resistant gloves and apron, face protection, lab coat, proper shoes, and an assistant is necessary. The first aid kit¹¹ contains Hexafluorine (skin and eye rinsing solution) and Calciumgluconat 10% 10 ml ampulla (fig. 3.10(c)). The vapor of

⁸The relative concentration is an empirical value from our institute.

⁹p. A. (pro analysi), the degree of purity is very high.

¹⁰For cleaning of the lab and vessels Extran neutral or Dekon neutral is used.

¹¹First aid: remove contaminated clothing (gloves!). Eye/skin acid contact: within 60 sec. flush with Hexafluorine (or water until then). Emergency shower is in the lab. Austria: call 144 or 112.

the acids is not allowed to be inhaled (pulmonary oedema).

Etching time:

Based on intended 25 μm etching depth and an etching rate of $v = 0.3 \mu\text{m}/\text{min}$ ¹², it takes $t = \Delta D/v = 83 \text{ min}$ for etching. The calculated mass loss is with the interferometer surface of 873 cm^2 $\Delta m = \Delta D \cdot O \cdot \rho = 5.1 \text{ g}$. Where the Si density is $\rho = 2.336 \text{ g}/\text{cm}^3$. The mass of the interferometer before etching is 2247.24 g. During the etching the interferometer has to be moved, this is necessary to bring fresh acid to the interferometer's surface, as well as to reduce bubbles in the acid which can disturb the etching process. HF has to be added about every 10 minutes (according to the removed Si mass). The calculation of the amount is given by:

$$\Delta HF \approx 20 \text{ ml/g} \cdot \Delta m(\text{g}) \tag{3.3}$$

The weight after etching (26.11.2014) is 2242.06 g ($\Delta m = 5.18 \text{ g}$) and the true etching depth yields very accurate:

$$\Delta D = \frac{\Delta m}{\rho \cdot O} = 25.4 \mu\text{m} \tag{3.4}$$

The true etching rate is therefore with 86 min etching time: $v = 0.295 \mu\text{m}/\text{min}$. 10 liters of HNO_3 and 170 ml HF acid, as well as 100 ml HF every 10 min have been used. The etched surface is depicted in 3.8.



Figure 3.8.: Surface of the etched interferometer lamella from fig. 3.5.

3.2.6. Final geometry

Finally, after the 25.4 μm etching, the geometry is calculated from tab. A.13. The results are presented in fig.3.9.

¹²The etching rate is about $v = 0.30 \dots 0.34 \mu\text{m}/\text{min}$ depending on the amount of acid bubbles on the surface and the IFM moving (every several min).

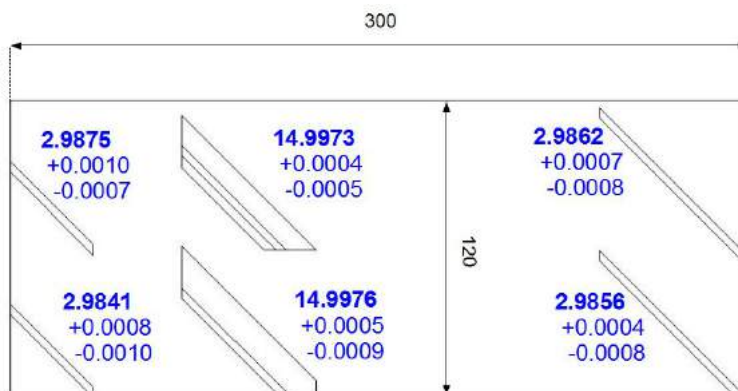


Figure 3.9.: Final blade thicknesses after 25.4 μm etching of the new interferometer (in mm). The blade no. are shown in fig. 3.7.

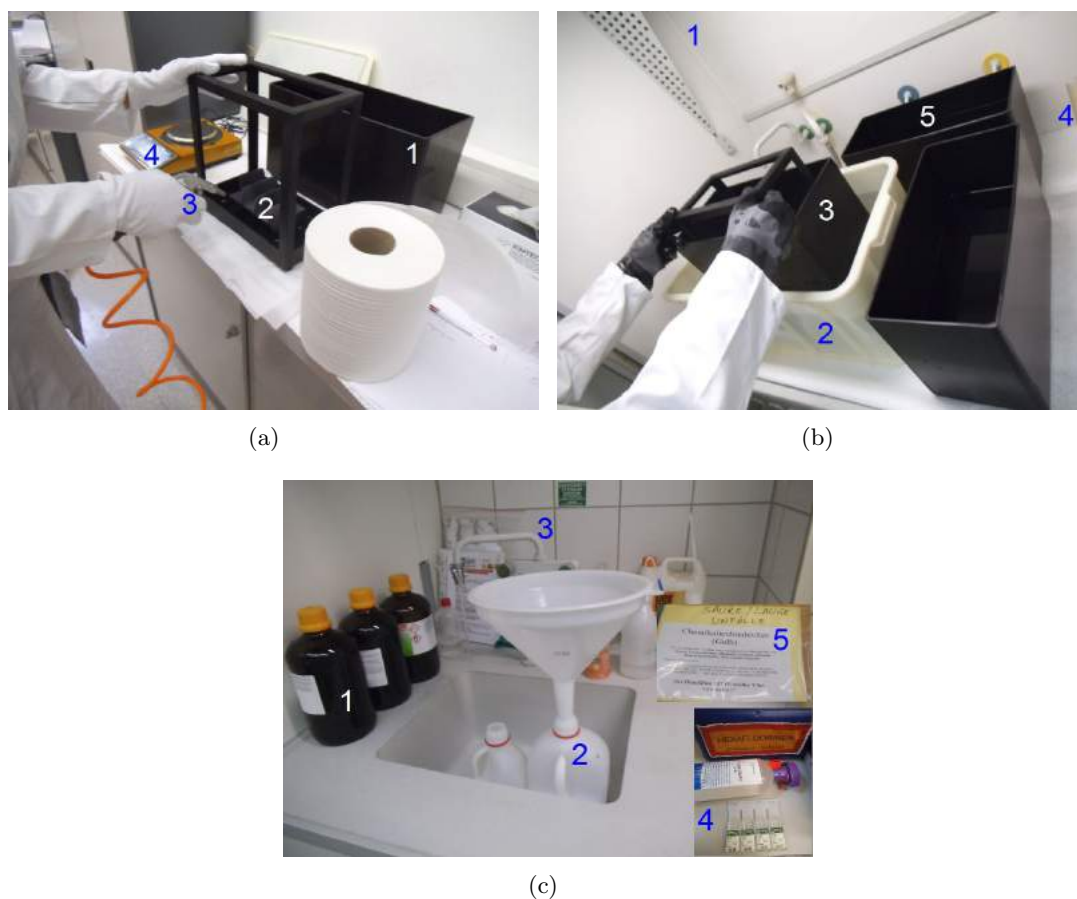


Figure 3.10.: Interferometer etching. (a): (1) Vessel with acetone for IFM cleaning ($39 \times 17 \times 24 \text{ cm}^3$), (2) holder to remove the IFM from the vessels, (3) nitrogen to dry the IFM before weighing, (4) mg balance. (b): (1) Fume cupboard, (2) cooling vessel with water for (3) PE etching vessel, (4) 100 ml cup for additional acid, (5) vessel filled with distilled water, before/after etching. (c): (1) HNO_3 , (2) bottles for the acid after etching, (3) water is on during the process, (4) first aid kit, (5) acid absorption fleece.

3.3. Original version

In the original planned version of the interferometer, there are two additional features. A thicker basis to reduce disturbances and step like cut middle blades for high angular resolution experiments as well as three loops for COW measurements (15 mm and 3 mm thick lamellas, see fig. 3.11).

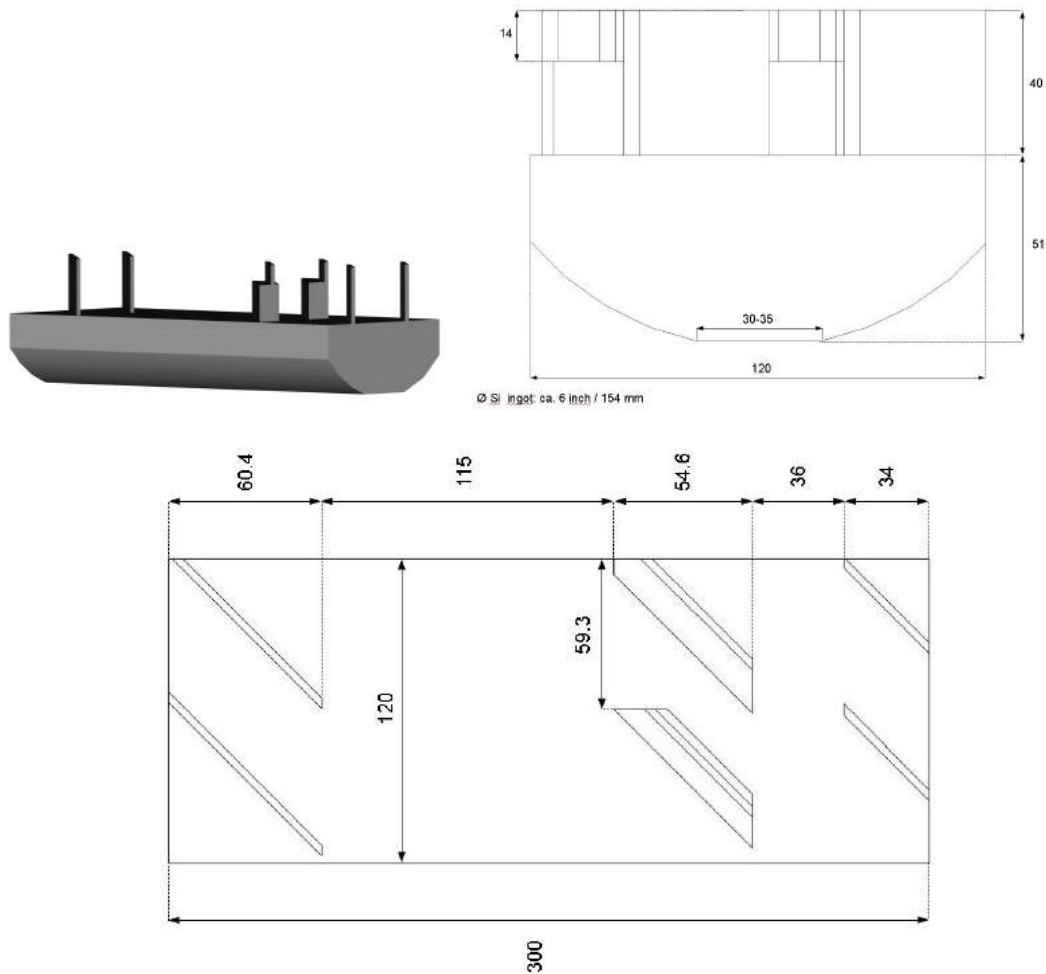
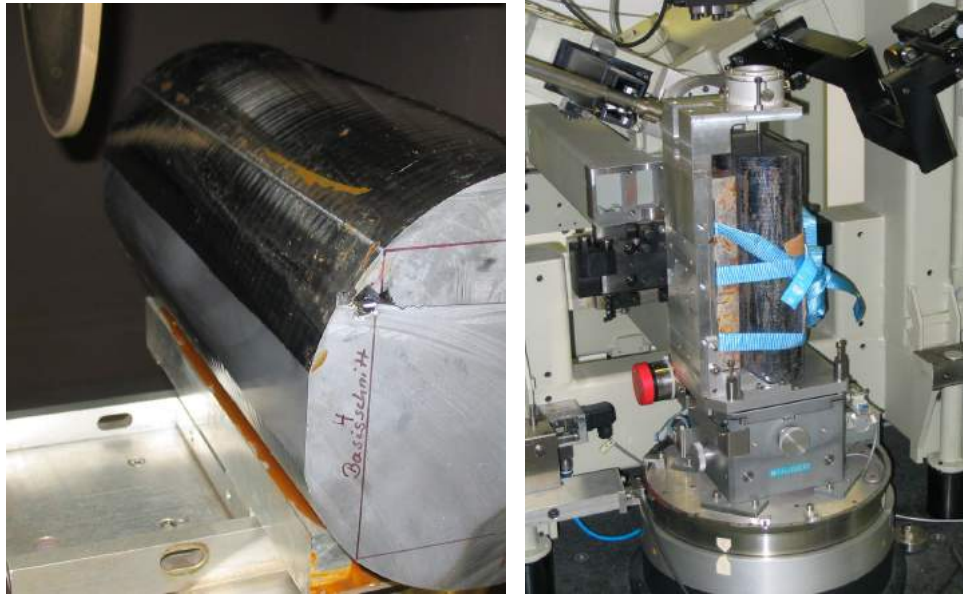


Figure 3.11.: Dimensions of the new interferometer, original version with thicker basis and step like middle blades.

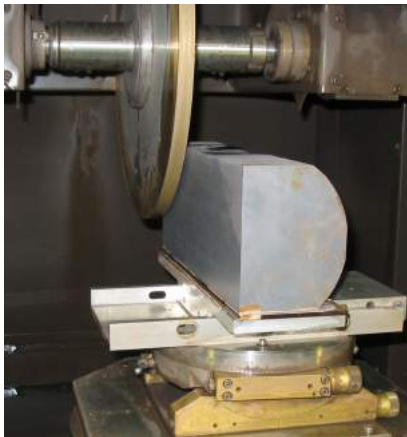
Unfortunately, during the preparation one of the blades is broken due to a programming mistake in the cutting machine at PTB (fig. 3.12). That is the reason for the use of the smaller part of the Si ingot for the interferometer. The remaining Si pieces can be used to cut a single-loop interferometer with a thick basis or a two-loop IFM with a thin basis¹³ and a long phase shifter ($12 \times 2 \times 0.3 \text{ cm}^3$) from the block between the lamella pairs (only one cut is needed).

¹³Depending on the test measurement of the produced IFM.

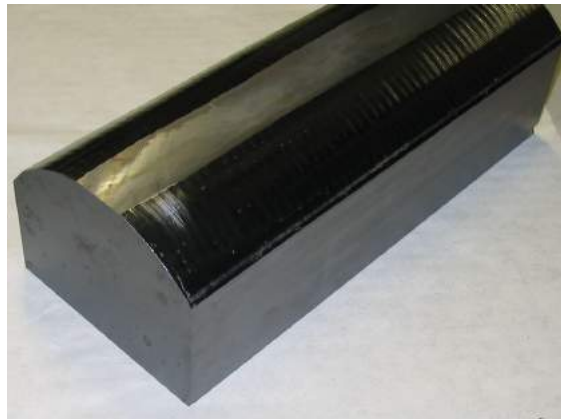


(a)

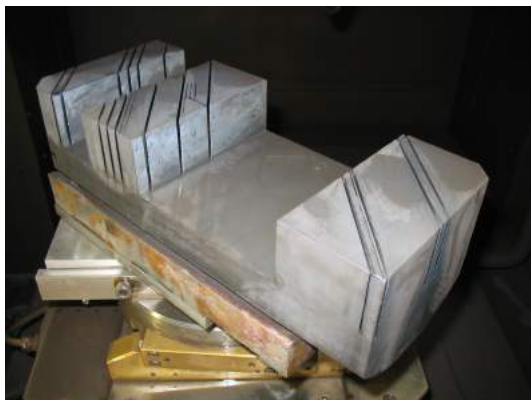
(b)



(c)



(d)



(e)



(f)

Figure 3.12.: Cutting of the new interferometer at PTB (original version). (a) Basis cut 3 mm, (b) orientation process, (c) grinding of the top surface, (d)(e) from this block the parallel interferometer lamellas are cutted. (f) Destroyed first loop, the new IFM is now cut from the other part of the Si ingot (fig. 3.3(a)).

3.4. Testing the new interferometer

With our new prepared interferometer, test measurements have been performed at ILL S18 in Grenoble. Before we measure the fringe visibility in order to demonstrate that an interference is possible with such a large IFM, rocking curves have been performed to give information about the crystal.

Rocking curves

The O and H-beam rocking curves are depicted in fig. 3.13. The aperture is $2 \times 1 \text{ cm}^2$ and two 140° Si prisms for the (220) and (440) Bragg peak separation have been used. This Si prisms are mounted in a way that their apex points to left or right in neutron direction. No phase shifter is placed in the beams and only the beam between blade 3 and 4 is blocked with Cd. The following results are obtained:

- The Si ingot is of sufficient quality: the (220) FWHM for the O-beam yields a good result of about $2.7''$ ($3.6''$ for the IFM in chap. A.4)¹⁴; the H-beam is wider: $3.6''$.
- The separation between the (220) and (440) Bragg peak amounts to $4.5''$ (right) and $3.3''$ (left) (eq. 2.22).
- The measured intensity ratio of the peaks (220):(440) is 1:0.32 (O-beam, prisms pointing right).

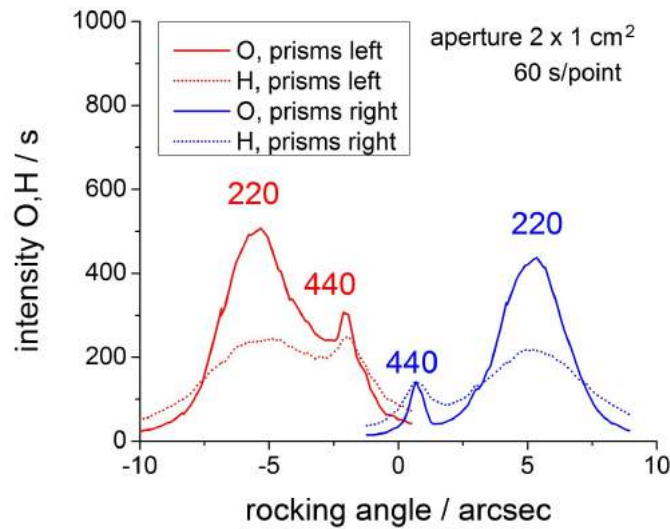


Figure 3.13.: Rocking curve of the new interferometer (O and H detector signal). With two 140° Si prisms, pointing in n-direction left or right. The (220) and (440) Bragg peaks are larger separated with the prisms pointing right.

¹⁴The ρ -axis is optimized in both cases, to the smallest FWHM, chap. A.5.

The rocking curve measurement has been repeated with a higher measurement time, where the transmitted beam after blade 1 is now blocked with Cd. The result is depicted in fig. 3.14 for the (220) Bragg peak. Compared to the calculation, the H-peak maximum is shifted relative to the O-peak, which indicates crystal strains.

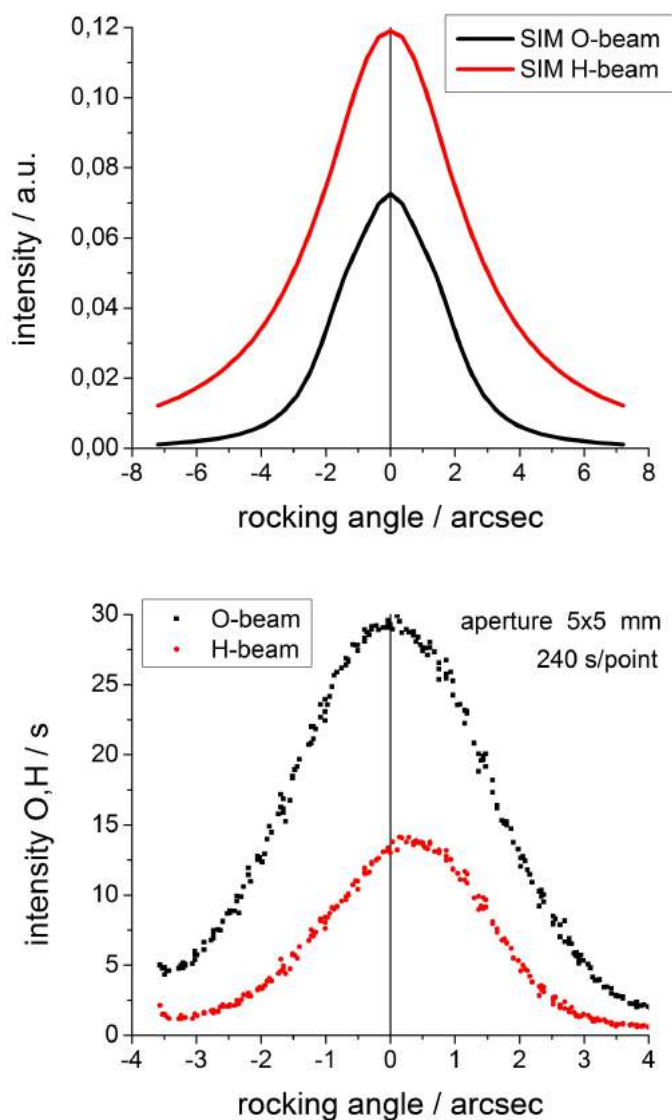


Figure 3.14.: Rocking curve of the new interferometer, for the (220) case. (top) Calculation and (bottom) experiment: FWHM: 3.6'' (O-beam), 2.9'' (H-beam), the H beam is smaller and shifted right compared to the calculation.

Visibility measurements

For the contrast measurements different supports have been tested, the highest observed contrast is 5%. Fig. 3.15 shows the intensity versus the thickness difference in the two beam path (interferogram), which is due to a rotating 5 mm thick aluminum phase shifter. The measurement time is 20 s/point, 24 points with a step size of about 0.03° have been used. The reason for this low contrast is probably due to the reduced basis thickness and contact strains from the crystal support. Therefore, a perfect-crystal interferometer of this size needs a thicker basis than 3.5 cm. However, due to limited measurement time, the crystal needs further tests with better temperature conditions and further different supports should be tested. Especially, the whole crystal can float in a high-density liquid like Natrium-polywolframat¹⁵. Also, a position-dependent neutron camera can be used, giving information about strains in the crystal (Moire patterns).

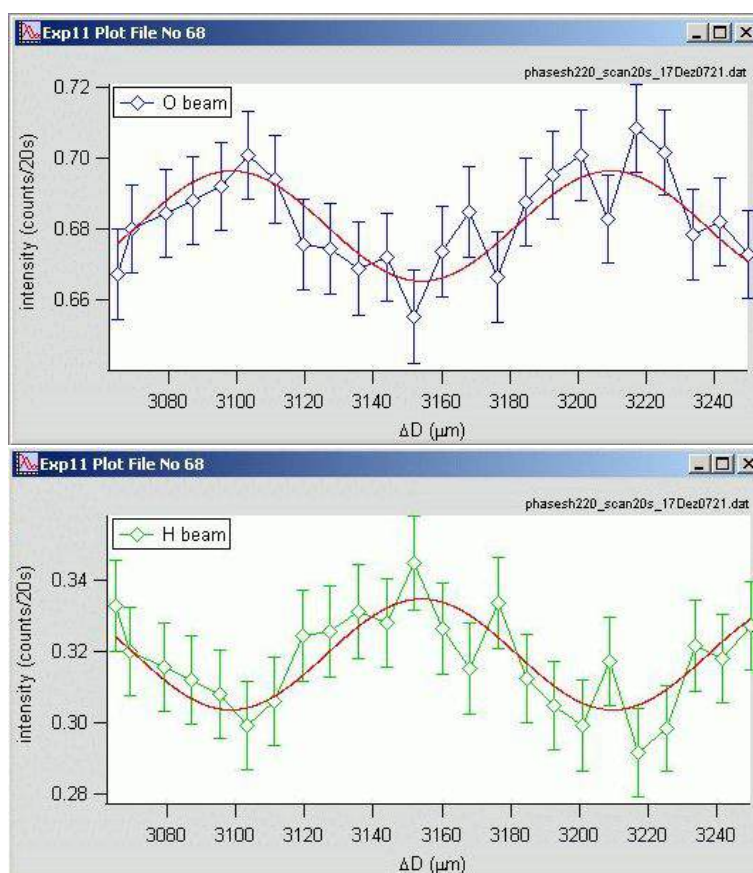


Figure 3.15.: Interferogram of the new IFM. (top) O-beam with 3% and (bottom) H-beam with 5% fringe visibility. The intensity in O is larger than in H, this indicates crystal strains.

¹⁵Can be removed completely from the silicon.

4. Chameleons

Another new and very promising application for large-crystal neutron interferometry with slow neutrons was recently proposed in [17]. With this method we search for phase shifts associated with the so called 'chameleons', these hypothetical particles are a prominent candidate for the dark energy. Chameleons describe the accelerating expansion of the universe with a particular dynamical dark energy model instead of Einstein's cosmological constant. Dark energy is of special interest, because it represents the largest energy contribution in the universe (68.3%), while the rest is dark matter (26.8%) and ordinary matter (4.9%) [18].

4.1. Theoretical

Khoury and Weltman [41] were the first who proposed the chameleon model. A detailed introduction to the chameleon model with associated preliminaries is given e.g. in the master thesis of H. A. Winther [42] and in [43]. The chameleon field couples to matter and generates a fifth-force with an effective range inversely proportional to its effective mass. This mass is similar to the color change of the chameleon reptile, the particles are able to adjust their mass to its environment. In dense environments the force of the chameleon field is screened, but free non-relativistic neutrons are not subject to the chameleon screening mechanism. Therefore, neutron interferometry can be used to measure phase shifts arising from chameleons. The density of the environment can be controlled with a vacuum chamber, which is placed as a sample in the interferometer. The chameleon potential $V_{eff}(\varphi)$ can be given by a Ratra-Peebles model, the first two terms in eq. 4.1 [44] describe the self interaction, the last term is the coupling to matter with density ρ (β is a dimensionless coupling constant).

$$V_{eff}(\varphi) = \Lambda^4 + \frac{\Lambda^{4+n}}{\varphi^n} + \frac{\beta \cdot \varphi \cdot \rho \hbar^3 c^3}{M_{Pl}} \quad (4.1)$$

$\Lambda \approx 2.4 \cdot 10^{-12}$ GeV is the dark energy value, $n > 0$ is the Ratra-Peebles index, $M_{Pl} = \sqrt{c/(8\pi G)} = 4.341 \cdot 10^{-9}$ kg the reduced Planck mass. The second derivative (by φ) of the potential correlates to the mentioned density-dependent mass M :

$$M(\rho)^2 = V''_{eff}(\varphi(\rho)) = n(n+1) \frac{\Lambda^{4+n}}{\varphi^{n+2}(\rho)} \quad (4.2)$$

The chameleon field φ for vacuum is written in eq. 4.3 [47]. This is the field between one pair of parallel chamber walls with infinite length (1D chameleon field), separated by the distance $2R$; x is the normal distance of a point away from the cell wall ($-R > x > R$).

$$\varphi(x) = \Lambda(R\Lambda)^{2/(n+2)} \left(\frac{n+2}{2\sqrt{2}} (1 - (x/R)^2) \right)^{2/(n+2)} \quad (4.3)$$

Note that the field profile is independent from β , it is illustrated in fig. 4.1 for several wall distances $2R$.

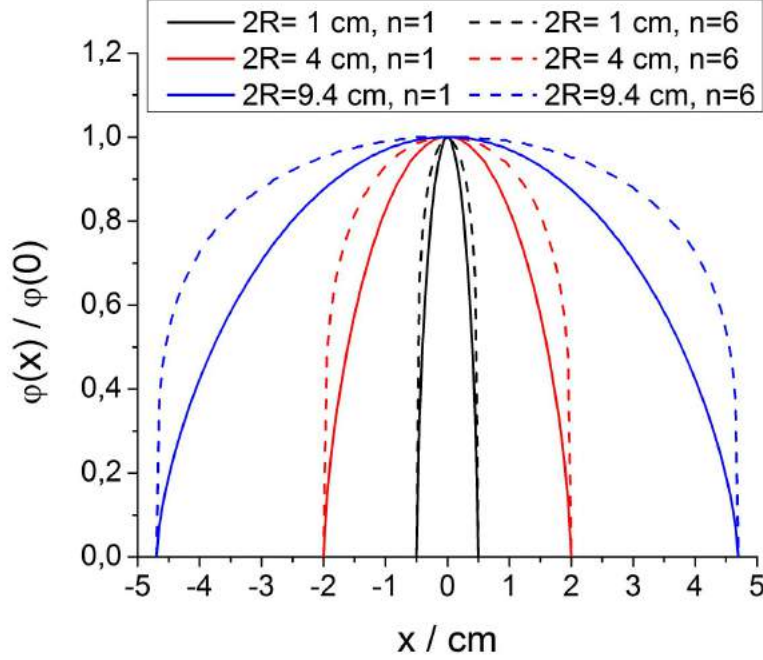


Figure 4.1.: Chameleon profile in a vacuum between 2 walls. Calculated for several wall distances $2R=1, 4,$ and 9.4 cm ($-R > x > R$), with $n=1$ and 6 , according to eq. 4.3.

In our neutron interferometry method, this chameleon field inside a vacuum chamber causes in the middle of the chamber a larger phase shift than on the edge (near matter). This phase shift is given by eq. 4.4¹ with $k = 2\pi/\lambda$, and the potential due to the chameleon field for the neutron is $\beta\varphi m_n/M_{Pl}$.

$$\phi = -\frac{m_n^2\beta}{k\hbar^2 M_{Pl}} \int_{-R}^R \varphi(x) dx \quad (4.4)$$

If the pressure in the chamber rises, the phase will decrease at a specific pressure for each β , according to eq. 4.5 for He [17].

$$\phi = \frac{m_n^2\beta}{k\hbar^2 M_{Pl}} \sqrt{2} (\varphi_0/\Lambda)^{n/2+2} K_n \left(\frac{\beta\rho}{M_{Pl}\Lambda^3} (\varphi_0/\Lambda)^{(n+1)/n} \right) \quad (4.5)$$

¹Note that we use SI units here, in 'natural units', c , \hbar and ϵ_0 are set to 1.

with

$$K_n(\alpha') = \int_0^1 \frac{u^{1+n/2}}{\sqrt{1 - u^n + n\alpha' u^n(u - 1)}} du$$

$$\frac{\beta\rho}{M_{Pl}\Lambda^3} = 23 \cdot 10^{-9} \beta \frac{P}{1 \text{ mbar}}$$

With our vacuum chamber geometry (see chap. 4.2) an approximation of the chameleon phase for different β and n is depicted in fig. 4.3 (personal communication G. Pignol)². The phase will decrease at a pressure around $10^{-4} \dots 10^{-2}$ mbar, a measurement of the phase in a sufficient pressure range can therefore exclude a certain β and n . The chameleon to matter coupling is excluded so far with a different method to $\beta > 10^{10}$ [45] and recently to $\beta > 5.8 \cdot 10^8$ [46]. According to [17], with neutron interferometry it would be possible to exclude $\beta = 10^7 \dots 10^9$, depending on the chamber size and the measured phase accuracy. This exclusions are plotted together with n in fig. 4.2. The dashed lines are calculated in [16], also the fifth-forth limit is shown in the plot, taken from [17].

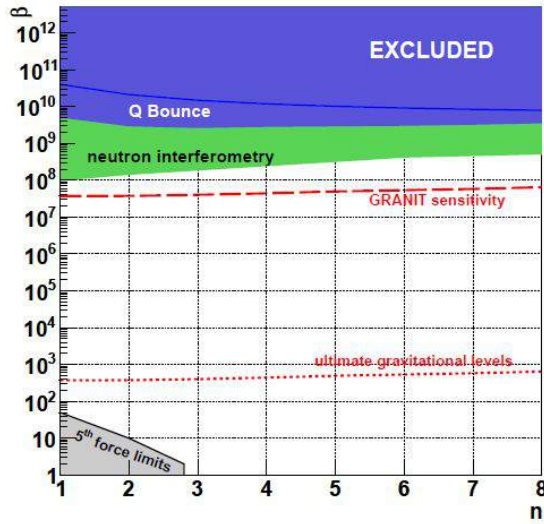


Figure 4.2.: β - n exclusion plot. From [45] $\beta > 10^{10}$ is excluded. The zone below, down to about $\beta > 10^8$ is expected to be excluded via neutron interferometry. The dashed lines are sensitivities calculated in [16]. Picture from [17].

²The correct numerical calculation with the used beam width and its positions are in chap. 4.3.

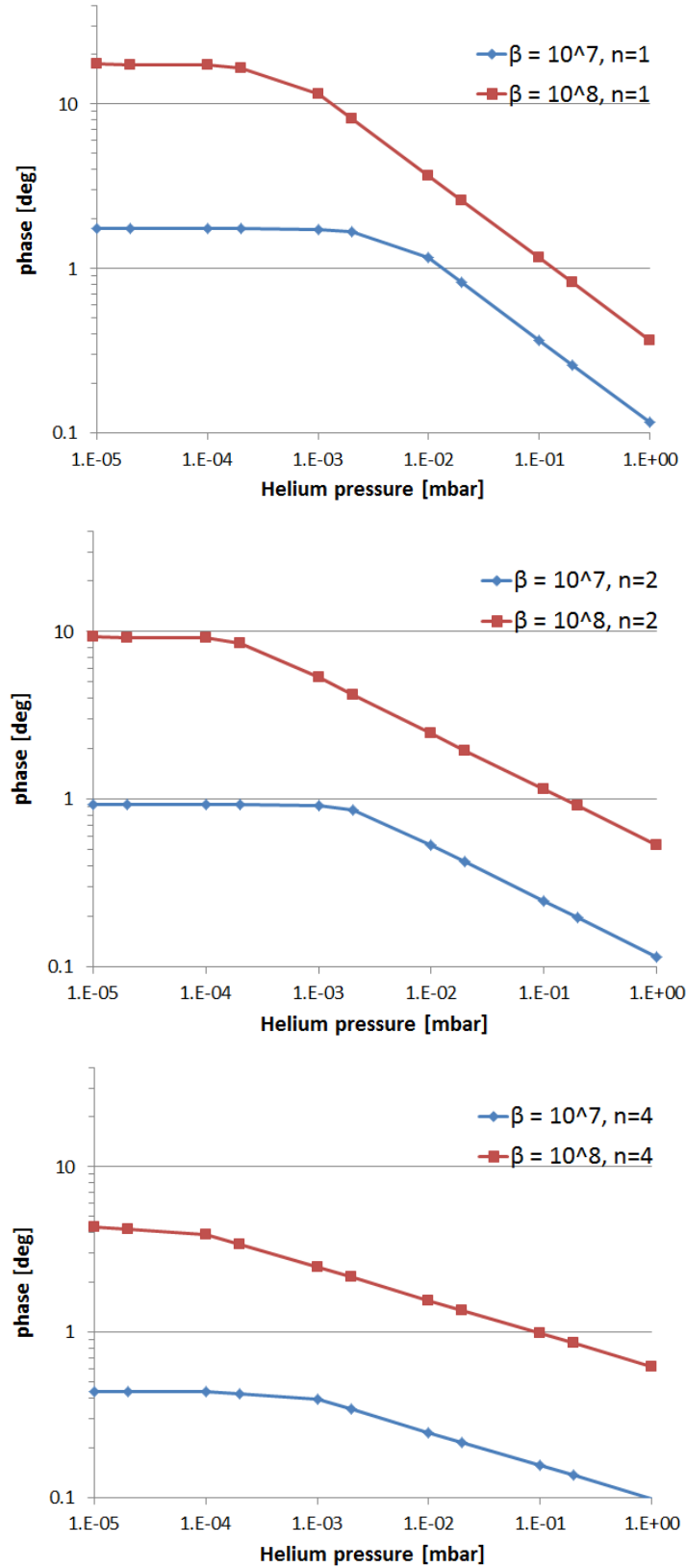


Figure 4.3.: Chameleon phase (approximation) for the chamber in fig. 4.6 with $\beta = 10^7$ and $\beta = 10^8$ for $n = 1, 2, 4$ (picture: personal communication G. Pignol).

4.2. Experimental

The main part in this experiment is a large-crystal neutron interferometer, where a vacuum sample fits in. The challenges are to move the vacuum chamber within the IFM, to evacuate it and to fill it with helium (He).

An overview of the whole experimental setup is depicted in fig. 4.4. The vacuum system (1)...(4), evacuates the chamber (5). The Si-crystal interferometer (6) is discussed below. In front of the aperture (4 mm wide and 6 mm high) are two 140° Si prisms for the 2.72 \AA wavelength selection (7). To reduce vibrations, the interferometer and monochromator is mounted on the optical bench (A). To move the chamber within the interferometer, a robot (B) is used, because of vibrations it is not connected to (A). Also the frame (C) where the pump (3) and a temperature shielding (D) is mounted, is not connected to (A). The neutron detectors are (O) and (H); the Bragg angle is $(45 \pm 0.25)^\circ$.

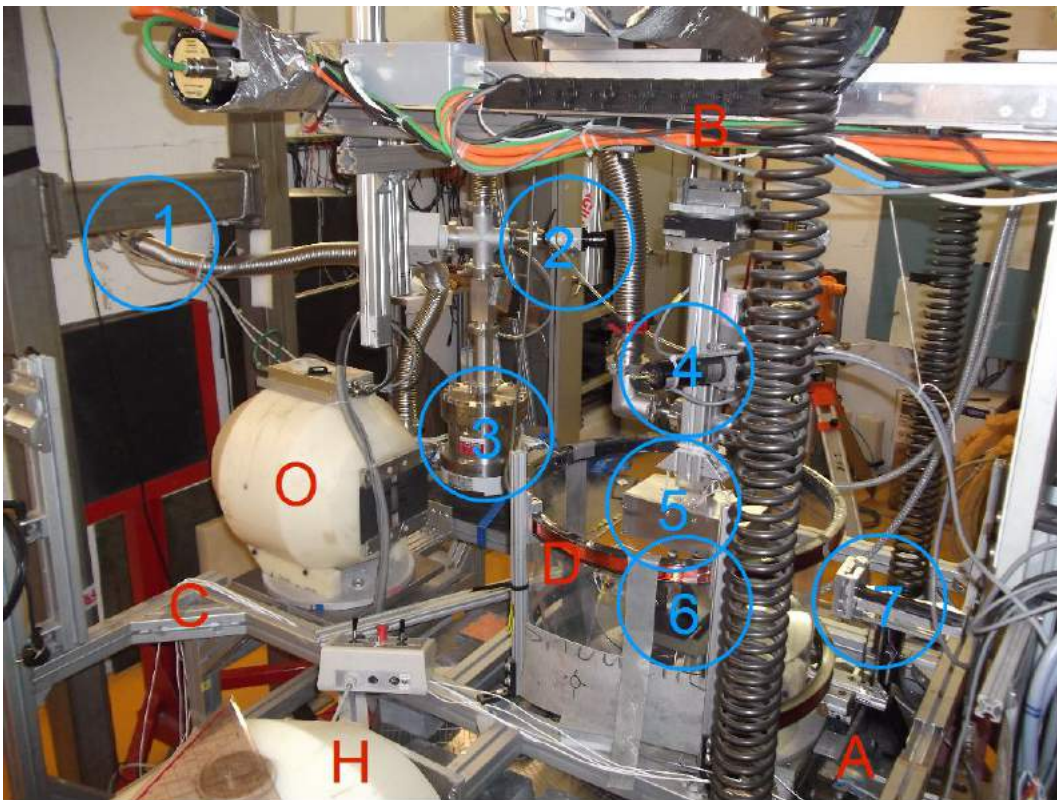


Figure 4.4.: Overview of the chameleon experiment. (1) Tube to the fore vacuum pump (outside to experimental area), (2) ventilating valve, (3) turbo molecular pump, (4) He inlet with motor, (5) chamber, (6) interferometer, (7) $4 \times 6 \text{ mm}^2$ aperture and 2 Si prisms, (A) vibration reduced bench, (B) robot to move the sample (5), (C) frame, (D) plastics for temperature shielding (no neutron influence), (O)(H) neutron detectors.

Interferometer

A picture of the used interferometer is given in fig. 4.5, it consists of 4 blades (3 mm thick) with enough space between (118 mm, beam separation: 48 mm) for the chamber (94 + 2 · 8 mm). The 4 x 6 mm² neutron beam after the aperture fall on the beam splitter (1). The interferograms are performed with a 3 mm thick phase flag of sapphire (2) or Si. For the measurements the chamber can be moved through the interferometer (X-direction) and can be evacuated and filled with He.

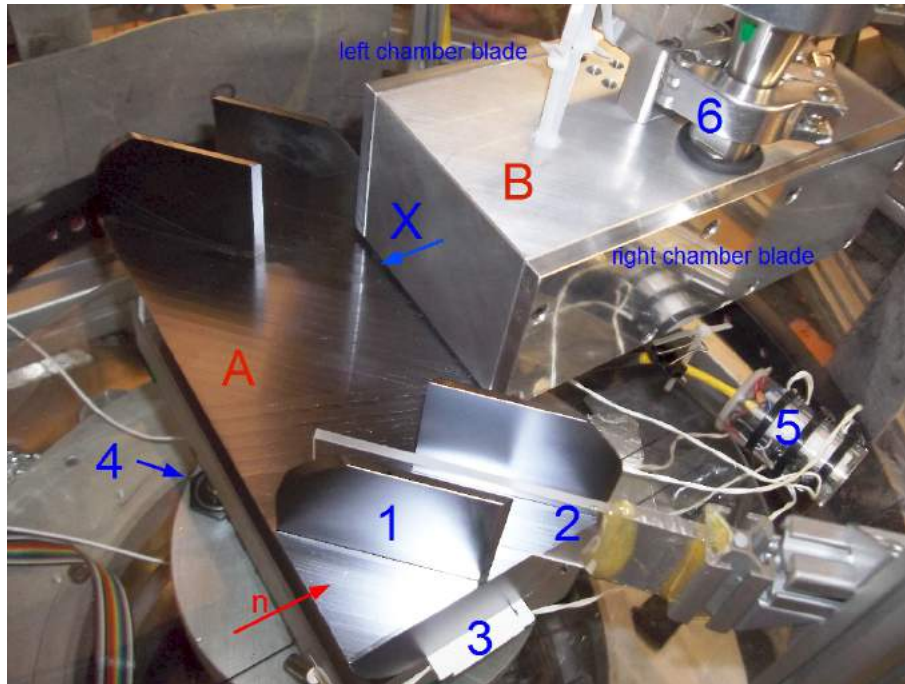


Figure 4.5.: (A) Interferometer (213 x 103 mm²), (B) chamber (210 x 110 x 70 mm³), (1) interferometer blade 1 (3 mm thick), (2) phase shifter sapphire 3 mm and Si 3 mm thick (3) small paper to optimize the contrast, (4) ρ -axis motor, tilts the IFM to the smallest rocking curve, (5) temperature sensors, (6) vacuum connection.

Chamber

The sample in the neutron interferometer is the chamber in fig. 4.6. Its dimensions are relevant for the measured chameleon phase. Part (A) and (B) are filled with air, both are connected to the environment with a hole on the top (width 65 mm, height 40 mm, depth 94 mm). Part (V) (width 40 mm, height 40 mm, depth 94 mm) with the sealing ring (1) can be evacuated and filled with He gas with the 5 mm hole (2). The figure shows the chamber from inside, in front and on the back side a 8 mm thick Al wall is mounted with screws e.g. (3), the neutrons pass through this two aluminum (Al) walls during the experiment.

In order to control the beam position relative to the chamber (X, Y and Z direction), the whole chamber is mounted on a device (robot). The exact wall positions between

the chamber parts (A), (V), (B) relative to the neutron beams are of interest, they can be determined with an intensity scan shown in fig. 4.7.



Figure 4.6.: Al chamber system without outer walls. (A)(B) Air chambers ($65 \times 94 \times 40 \text{ mm}^3$), (V) vacuum chamber ($40 \times 94 \times 40 \text{ mm}^3$, wall thickness to (A)/(B) is 8 mm). (1) Vacuum sealing ring, (2) connection to the vacuum system and He-inlet ($\text{Ø}5 \text{ mm}$ hole), (3) screw hole for mounting Al walls.

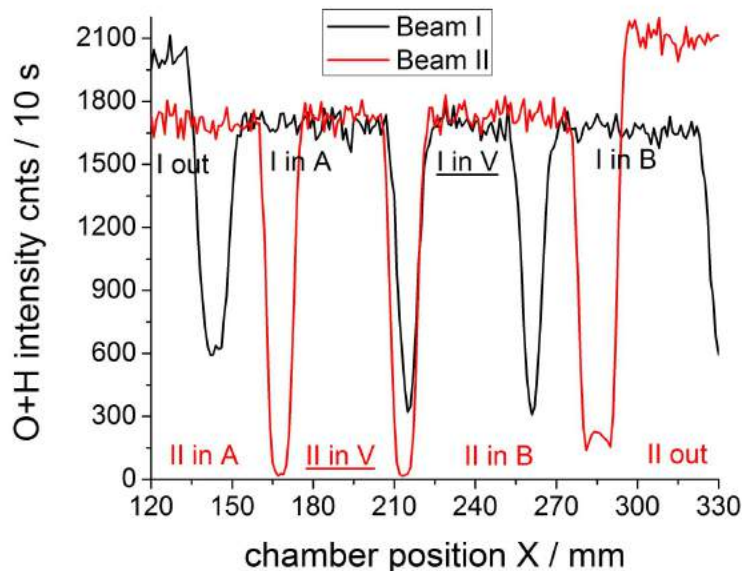


Figure 4.7.: Determination of the chamber wall positions, by moving the chamber through the IFM in X-direction. The X-positions of the chamber part (V) (left, middle, right) are: 177, 191 and 205 mm (beam II only) and 224, 238 and 252 mm (for beam I).

In detail, this is done either with the IFM beam I or II separately. The beam II is fully out of the wall (with 1 mm distance³) and inside the chamber (V) at 177 mm and 205 mm, the chamber center is then at 191 mm. The determined positions for beam I are: 224, 238 and 252 mm. An illustration of this positions, relative to the interferometer is given in fig. 4.8.

³Note that the originally 4 mm wide beam is broader behind the IFM blades.

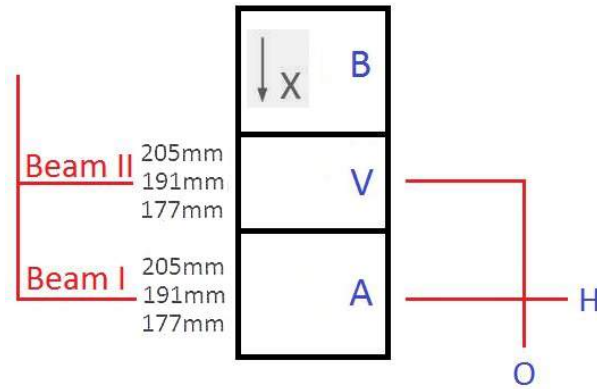


Figure 4.8.: Chamber positions relative to the interferometer beams. The chamber moves in X-direction through the interferometer, e.g. at $X = 191$ mm beam II is in the middle of (V) and beam I in the middle of (A).

Vacuum system

A sketch of the vacuum system is shown in fig. 4.9. The necessary vacuum is created by a fore vacuum pump (scroll pump, max. 10^{-2} mbar) and a turbo molecular pump (TMP, 10^{-4} mbar). Additional He can be inserted into the chamber until the maximum pressure for the TMP is reached. The value of the pressure gauge ('Pfeiffer PCR 280') needs a correction factor for the use of He instead of air (0.8).

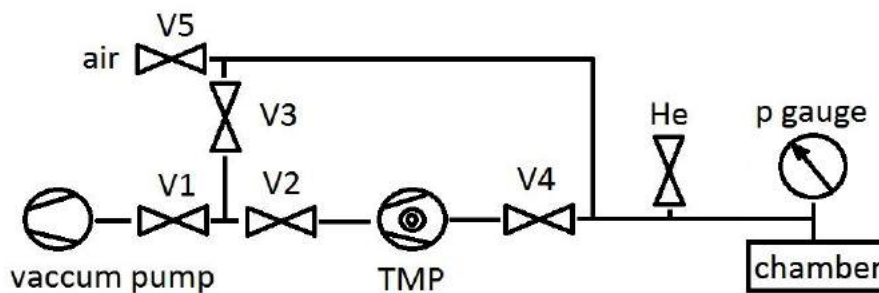


Figure 4.9.: Vacuum system. (TMP) Turbo Molecular Pump, (V1) fore vacuum pump valve, (V2)(V4) TMP valve, (V3) bypass valve (start pumping/TMP out), (V5) venting valve, (He) helium inlet, (p) pressure.

4.3. Measurement

Our experiments are based on [17], we investigate here three different methods to measure the chameleon phase. First, with a fixed position of the chamber, at different He pressure values. Secondly, the phase is determined for several chamber positions. The third method records the phase between two chamber positions, for a larger pressure range.

4.3.1. Method I: phase vs. pressure (at fixed chamber position)

The chamber is fixed at a position, where the beam II passes the middle of the vacuum chamber ($X=191$ mm, fig. 4.8). Then the phase shift is measured with an interferogram at four pressure values. The pressure is increased by filling helium into the chamber. The pressure values are (corrected for He):

- $p_1 = (2.51 \pm 0.25) \cdot 10^{-4}$ mbar
- $p_2 = (7.7 \pm 1) \cdot 10^{-4}$ mbar
- $p_3 = (30.6 \pm 5) \cdot 10^{-4}$ mbar
- $p_4 = (119.2 \pm 50) \cdot 10^{-4}$ mbar

In detail, the measurement procedure have to be corrected for an arbitrary, temperature dependent interferometer phase. Therefore, the interferograms at each pressure are not taken one after another. Instead they are performed parallel: at each position of the phase shifter, the intensity is measured simultaneously at 4 pressure values according to fig. 4.10. In the experiment 41 phase shifter positions have been used, each position corresponds to a point on the sine interferogram (compare chap. 2.2.1).

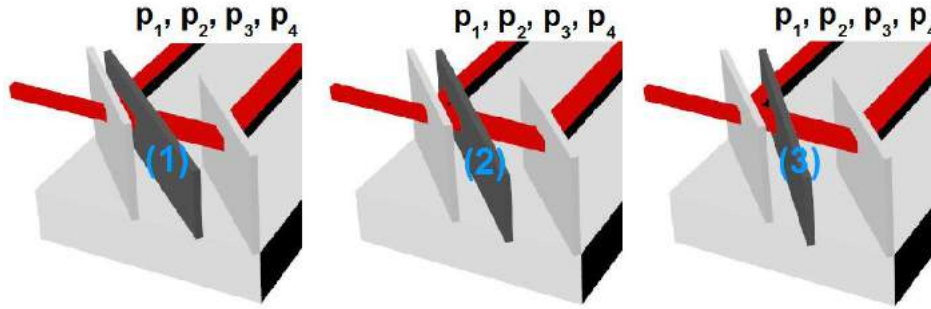


Figure 4.10.: Measurement principle of the chameleon phase with method I. At each phase shifter position (1), (2) and (3), the pressure p is changed 4 times.

These 4 phase values, each at a different pressure are comparable, but not its absolute value because of this arbitrary interferometer phase. The phase difference is given relative to the phase at the highest pressure in fig. 4.11, hence this value has no phase error bar. Additionally, the measurements are compared with theoretical values. These are numerical calculations for our specific chamber geometry and beam position; performed by G. Pignol. The chameleon field would lead to a pressure-dependent phase shift, the open parameters: coupling constant β and n can be restricted by the measurement. This

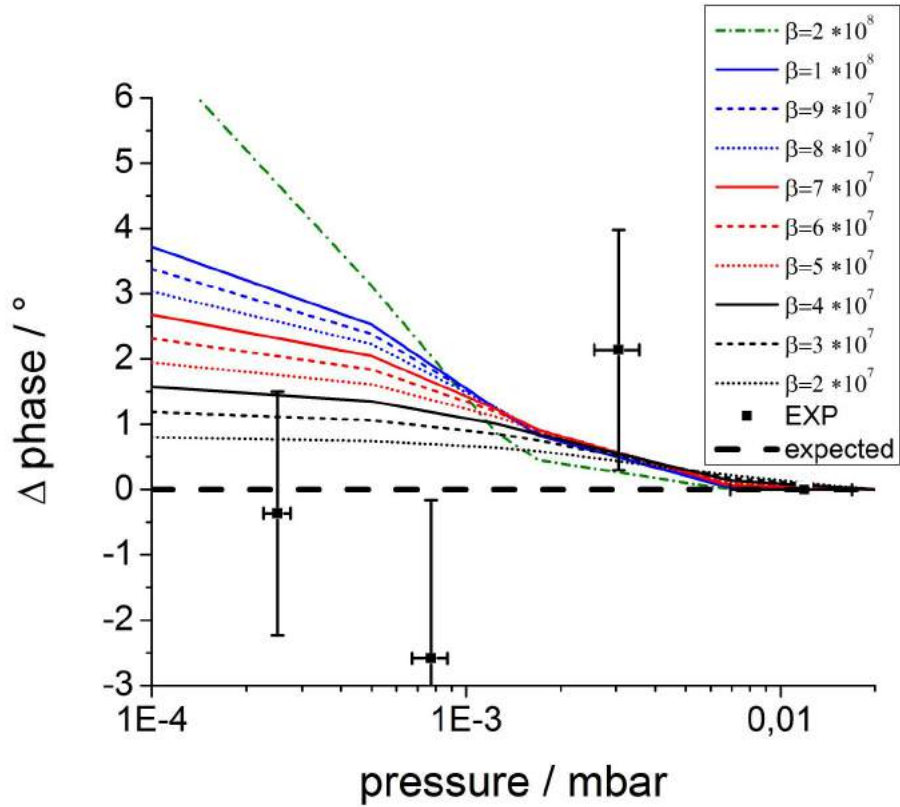


Figure 4.11.: Chameleon phase vs. He pressure. Numerical values (personal communication G. Pignol), EXP: average value of 4 single measurements, 'expected': without chameleon field.

will be done later together with method III. A rerun of the measurement with nitrogen was because of the limited time not possible.

4.3.2. Method II: phase vs. chamber position

As we see in fig. 4.1 the chameleon field depends on the distance from the chamber walls. While in method I the vacuum chamber position is fixed, we investigate here the phase for several X-positions.

This measurement procedure has to be corrected for the arbitrary phase shift as well. Therefore, parallel to the interferograms taken at a certain X-position ('IN'), always an interferogram at X=205 mm is performed ('OUT', fig. 4.8). This is sketched in fig. 4.12 for only 2 phase shifter points (out of 21), all points together constitutes an IN and an OUT interferogram.

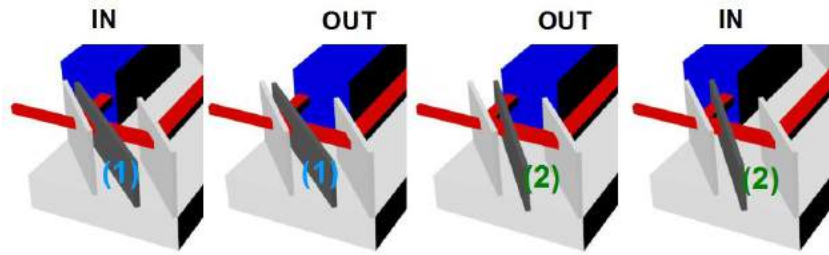


Figure 4.12.: Measurement principle of the chameleon phase with method II. At each phase shifter position (1,2), the X-position of the chamber is changed 2 times. This sequence is repeated for every X-point.

The results of the measurements are given in fig. 4.13. Surprisingly this phase difference is not zero (or symmetric along the chamber) and reaches 40° on one side of the chamber (V). A remeasurement at a higher pressure, yields the same result.

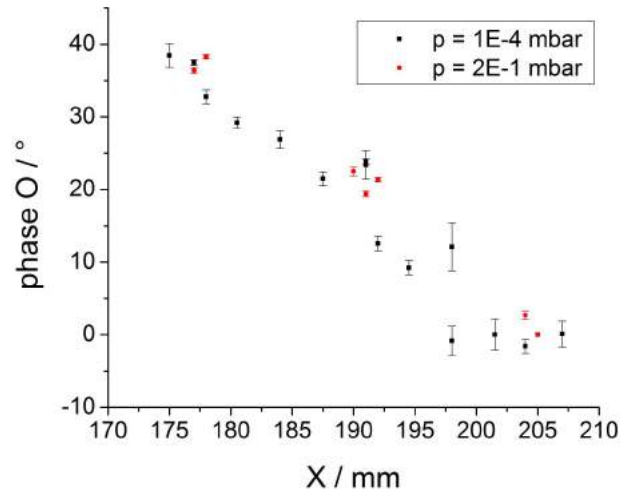


Figure 4.13.: IN minus OUT phase vs. chamber position. IN: chamber at a X-position, where beam II hits (V), OUT : X= 205 mm. Each point is an average of about 10 single measurements.

The origin of this phase is not obvious, however in chap. A.10 we found a possible explanation by measuring the chamber wall thicknesses. It reveals a special shape resulting in such a phase⁴. Note that this phase does not effect the result from method I due to the not changing chamber-position.

4.3.3. Method III: phase (between 2 chamber pos.) vs. p

The phase difference from the last method can be extended to a wide range of pressure values. The phase due to the chamber walls is assumed to be constant, a phase change with pressure would then indicate a chameleon field. The advantage compared to method I is that a larger pressure range is now available due to technical reasons⁵.

Fig. 4.14 shows the measurement principle of method III in detail, for one phase shifter point only. For the complete measurement the phase shifter position is changed 21 times, this sequence is then repeated for all pressure values.

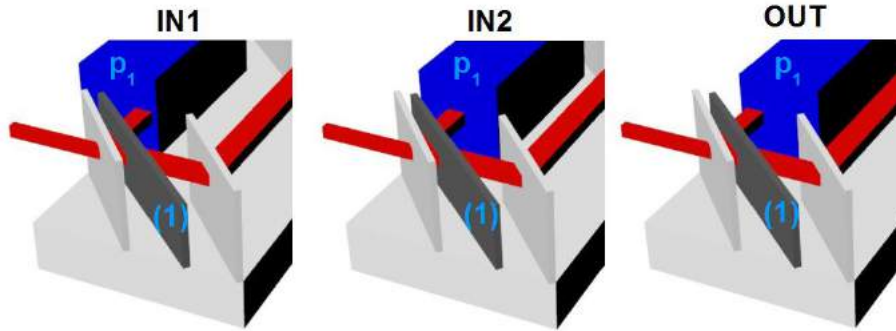


Figure 4.14.: Measurement principle of the chameleon phase with method III. The first phase shifter position is shown (1), where the pressure p is constant and the chamber position is changed 3 times (IN1, IN2, OUT). This sequence is repeated for all phase shifter points and then for all pressure values.

The results of the measurement is plotted in fig. 4.15 for the phase differences at IN1-OUT and IN2-OUT. Each point is an average of about 10 single measurements. The linear fit yields for the intercept $(17.4 \pm 0.5)^\circ$ and $(36.9 \pm 0.5)^\circ$ respectively, this is the offset phase from the chamber wall.

A comparison of the measured with the theoretical values is shown in fig. 4.16, the offset is now subtracted. The theoretical values are numerical calculations for our chamber geometry and beam position (performed by G. Pignol). Note that the He phase shift in this pressure range is negligible ($< 0.001^\circ$). The final result of method I and III together is that the chameleon field can be exclude coupling constants $\beta > 1.9 \cdot 10^7$ with $n = 1$ (at 95% C.L, personal communication Pignol⁶). For $n = 2, 3, 4$ we yield $\beta > 5.8 \cdot 10^7$, $2.0 \cdot 10^8$, and $4.8 \cdot 10^8$ respectively. Hence, the neutron interferometry is very sensitive, resulting in a new limit for β .

⁴Unfortunately, the screw holes of our walls have been drilled after the surfaces had been polished

⁵The pressure can be changed now between interferograms and not during the interferograms, in the higher pressure range the TMP must be removed, chap. 4.2.

⁶For certain values of β their probabilities $p(\beta)$ are calculated by comparing the calculated phase shifts with the measured phase shifts. The limit of β with 95% confidence level is determined by numerically solving: $\int_0^{\beta_{limit}} p(\beta)d\beta = 95\%$ [19].

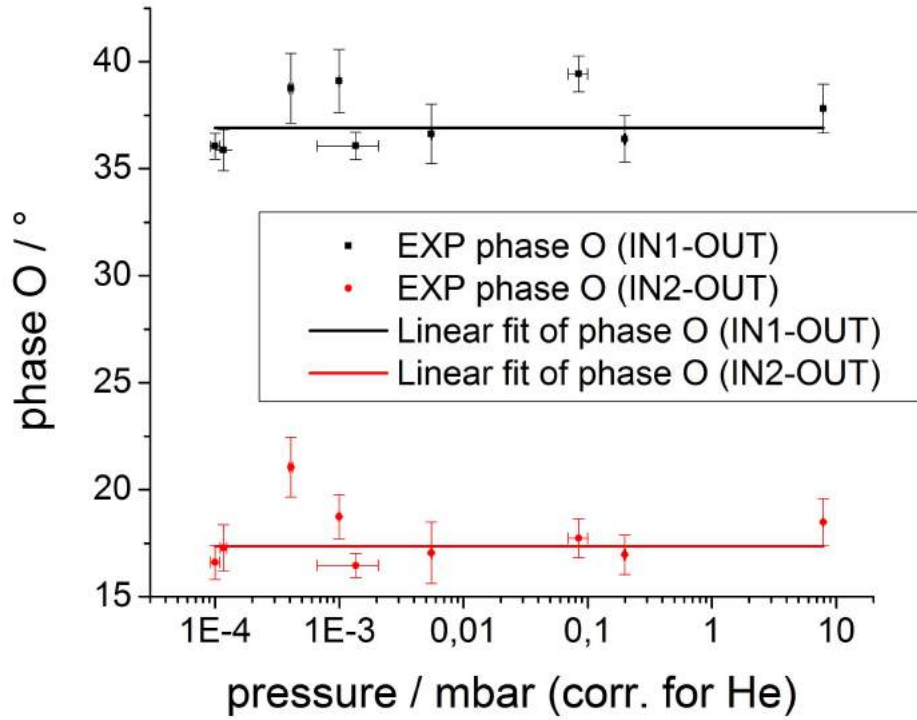


Figure 4.15.: Phase difference between two chamber positions IN-OUT, over a large pressure range. IN1 ($X = 177$ mm), IN2 ($X = 191$ mm), OUT ($X = 205$ mm).

Summary

With a large-crystal neutron interferometer we searched for phase shifts arising from hypothetical 'chameleon' particles, a prominent candidate for the dark energy. The interferometer must be large, in order to host a vacuum chamber as a sample. The phase shift depend on the beam position within a vacuum chamber as well as on the pressure. This leads to three different measurement methods, which have been performed here. Method II only addresses the phase shift versus the position, unfortunately the chamber wall thickness was not exactly homogenous. However method I and III were performed on a small and large pressure range, where we found no pressure dependence on the phase. We can therefore exclude the chameleon model down to a specific coupling constant β . If the chameleon particles exist, its β value must be smaller than $1.9 \cdot 10^7$, which is a better limit than the current value found by the qBOUNCE collaboration ($\beta > 5.8 \cdot 10^8$ in [46]).

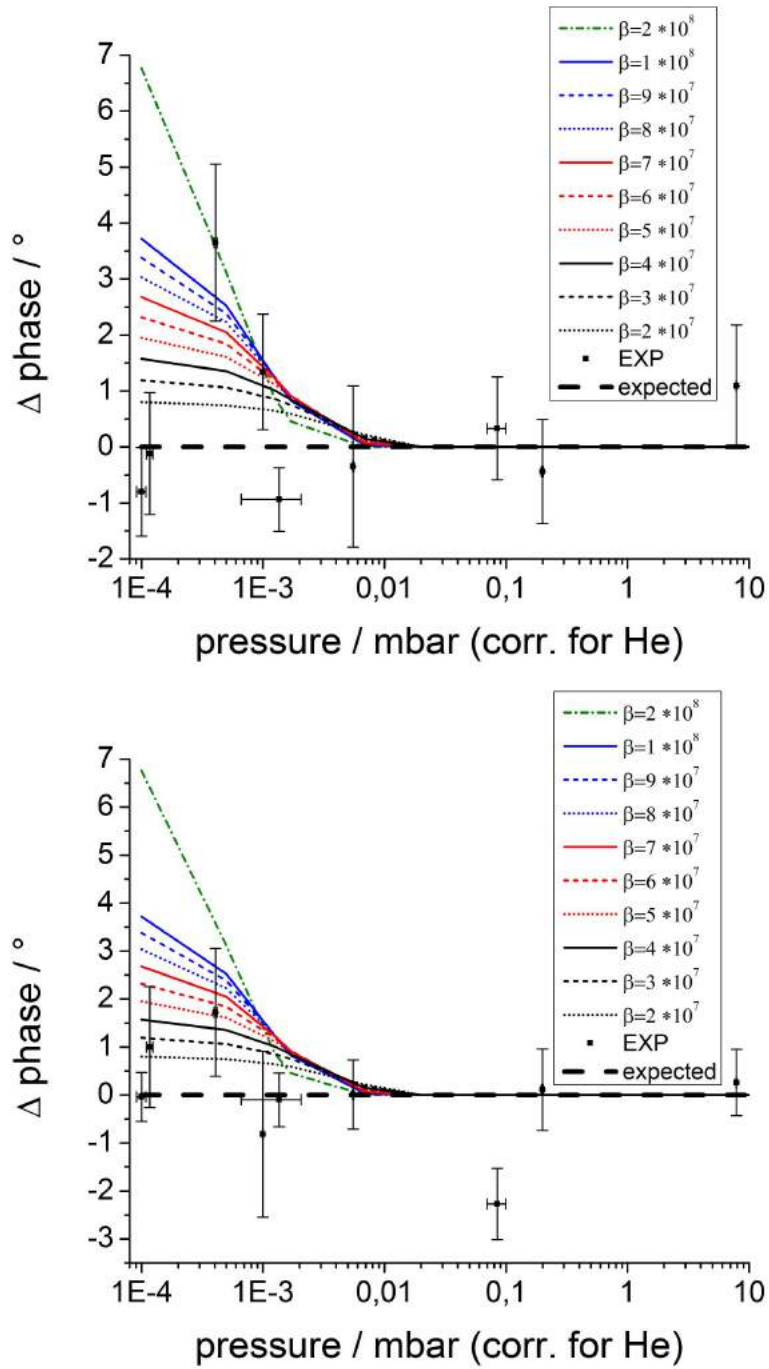


Figure 4.16.: Phase difference between 2 chamber positions vs. He pressure. Calculated for different β ($n = 1$) and without chameleon theory ('expected'). (top) Phase between IN2-OUT, (bottom) IN2-IN1.

5. Summary and conclusions

Laue Phase

In this study, a large neutron interferometer was used to measure the phase shift of a perfect silicon crystal, in the vicinity of the Bragg condition (Laue phase). The rotation range of this crystal is $\delta\theta = \pm 0.06$ arcsec for (220) and $\delta\theta = \pm 0.015$ arcsec for the (440) case. Distinct phase sensitivities of 5.5° (220) and 11.5° (440) per 0.001 arcsec deviation from the Bragg angle were achieved. Additional factors that affect this phase were identified and systematically investigated. With the setup used, two pairs of Pendellösung plateaus for the (220) case and one pair for the (440) case were identified. These plateaus are regions with increased sensitivity to fundamental parameters. The Laue phase was measured with an accuracy of $\pm 9^\circ$ (1st plateaus) and $\pm 15^\circ$ (2nd plateaus). An additional temperature shielding of the whole monochromator - interferometer setup (is currently planed at S18), as well as a more accurate rocking device would be necessary, in order to increase the phase accuracy. The parameters that affects the Laue phase in the first and second plateaus are summarized in tab. 5.1, the prisms and their alignment angles are also important. A very fundamental parameter is the neutron-electron scattering length [5], it describes the scattering interaction of the neutron with an electron. Here contradicting values exists; however we found that the experimental sensitivity of this method is not sufficient.

Table 5.1.: Change of the Laue phase at the positions of the 1st and 2nd plateau respectively, for the relevant parameter variations. Calculation for the (220) Bragg monochromator, Darwin width = 1 and real I geometry.

parameter	variation	1 st plateaus	2 nd plateaus
IFM geometry	ideal-real I	4.7°	10.9°
Monochromator	Bragg-Gauss	7°	27°
Darwin width	1/1.2	6°	30°
Rocking angle	0.18''	1.5°	6°
Wavelength	0.03 Å	1°	6°
b_{ne} (440)	0.0003 fm	0.3°	(0.6°)
b_{ne} (220)	0.0003 fm	0.2°	0.45°
prism angle β	0.001°	0.2°	0.4°
prism angle $slope_{phd}$	0.5°	0.75°	1°
prism angle r_{phd}	1°	1°	2°

To overcome the contrast reduction with increasing beam deflection, one can select a relative measurement technique at the cost of reduced phase sensitivity.

New interferometer

Within this work, the worldwide largest perfect-crystal neutron interferometer was fabricated. The additionally 15 mm thick sample blades can be used for a high angular resolution measurement. The large area of the enclosed interfering beams can be of great value for measurements of gravity induced phase effects (COW). The preparation steps of this interferometer are given. The oriented cutting was performed essential in co-operation with the Physikalisch- Technische Bundesanstalt in Braunschweig. The grinding and geometry measurement at the company 'Rauch Ges.m.b.H.' in Vienna. The interferometer was etched with hydrofluoric and nitric acid (25.4 μm) at the Institute of Atomic and Subatomic Physics in Vienna. The test measurement at the 'Institut Laue-Langevin' in Grenoble demonstrated that an interferogram can be obtained with such a large interferometer.

Chameleons

By use of the neutron interferometric technique, we investigated a candidate for dark energy, the 'chameleon' model. These hypothetical particles are able to adjust their mass to its environment, resulting in a position, as well as a pressure dependent phase shift within the vacuum chamber. This leads to different experimental methods, which are investigated here. With our measurement we did not see a hint of the existence of chameleon particles; however, the chameleon field coupling constant β can be excluded to $1.9 \cdot 10^7$, which is a better limit than the current value found by the qBOUNCE collaboration ($\beta > 5.8 \cdot 10^8$ in [46]).

A. Supplements

A.1. IFMSIM

The software IFMSIM from H. Lemmel calculates the neutron behavior within a perfect crystal interferometer with samples (phase shifters, wedges, absorbers, Laue crystals) [7]. The geometry of all interferometer blades and samples can be freely defined, also multi-loop-interferometers are possible. The incident beam can be defined by its angle, width and divergence (monoenergetic coherent wave packet). The calculation process of the wave function is given in chap. 2.1.2. In fig. A.1 the user interface of IFMSIM is depicted with the used 6 blade interferometer and the neutron path in the x-y plane. For instance a rocking curve can be performed by a rotation of the incident beam or a simultaneous rotation of all IFM blades. The commands are listed in tab. A.1.

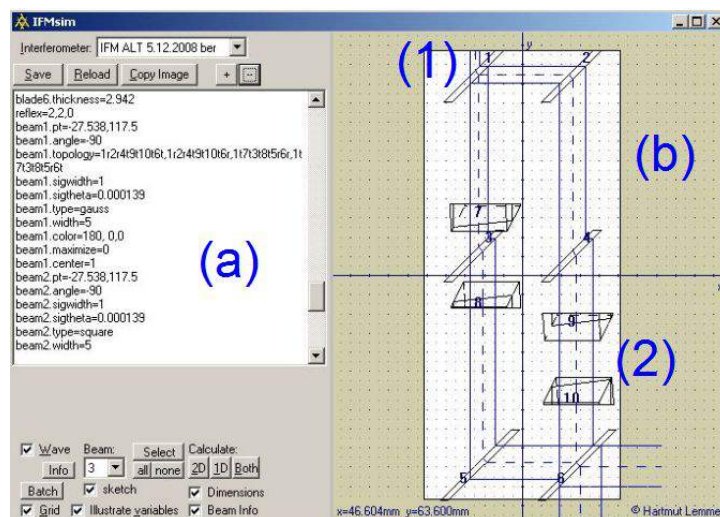


Figure A.1.: IFMSIM: (a) input of the interferometer geometry, samples and beam specification. (b) Graphical representation of the input in the x-y plane. The incident wave is split at blade (1) and passes through the blades/prisms (2).

Program extensions

IFMSIM performs the calculation with parallel front and back surface of each Laue crystal blade, lattice planes are normal to the surfaces (symmetric Laue type crystals), and no surface roughness or waviness is considered (the resulting visibility of interference is therefore an upper limit). The wavelength used in the calculations is monochromatic (in the experiment is always a certain wavelength distribution, which is coupled to the beam divergence due to Bragg reflection on the monochromator, σ_θ is here smaller than the usual value of $0.25 \dots 0.5^\circ$).

Table A.1.: IFMSIM commands; angles in degrees. Further information are given in the manual [7].

object	commands
interferometer	'blade1.thickness=3', 'bladeangle=45', 'blade1.front / back.pt', blade1.front / back.end1/2'
beam topology	'beam3.topology=1r2r4t6r,1r2r4t6t,1t3t5r6r,1t3t5r6t'
interferogram	'batch.action=ifgTTRR+RRTT'
type of monochromator	'beam1/2/3.type= gauss/square/bragg'
Bragg peak	'reflex=2,2,0'
beam divergence	'beam1/2.sigtheta= 0.00045', 'beam3.darwinwidth= 1'
wavelength	'beam.angle=-90'
rocking position e.g. pos.+B	'beam3.rotation=0.0005'
scattering length b_{ne}/b_{nuc}	'bneoverbnuc=-0.000316/-0.000383'
blade rotation	'blade3/4.rotation'
prism α -rotation	'blade7/8/9/10.rollangle'
pivot of prism α -rotation	'blade7/8/9/10.rollaxis.pt=x,y,z'
$slope_{phd}$	'blade7/8/9/10.angle' (12.5 $\hat{=}$ 90 $^{\circ}$ n-prism surface)
r_{phd}	'blade7/8/9/10.rollaxis0. angle' (90 is $r_{phd} = 0^{\circ}$)
prism apex angle β	'blade7/8/9/10.wedge angle'

Recently updates are:

- Bragg monochromator curve, eq. 2.20
- possibility to calculate additionally all 4 prisms and show the equivalence of prism rotation and blade rotation (chap. 2.4.6).
- additional rotation to change the prisms pivot (fig. A.2)
- increase the step size of the calculation loop, create a '.dat' output file to record the used parameters

Further extensions would be:

- 3D: gravity
- coriolis force
- wedge shaped and non-parallel Laue crystals
- extract the values from the beam-profile calculation in an output file, and create diagrams for the batch-processes

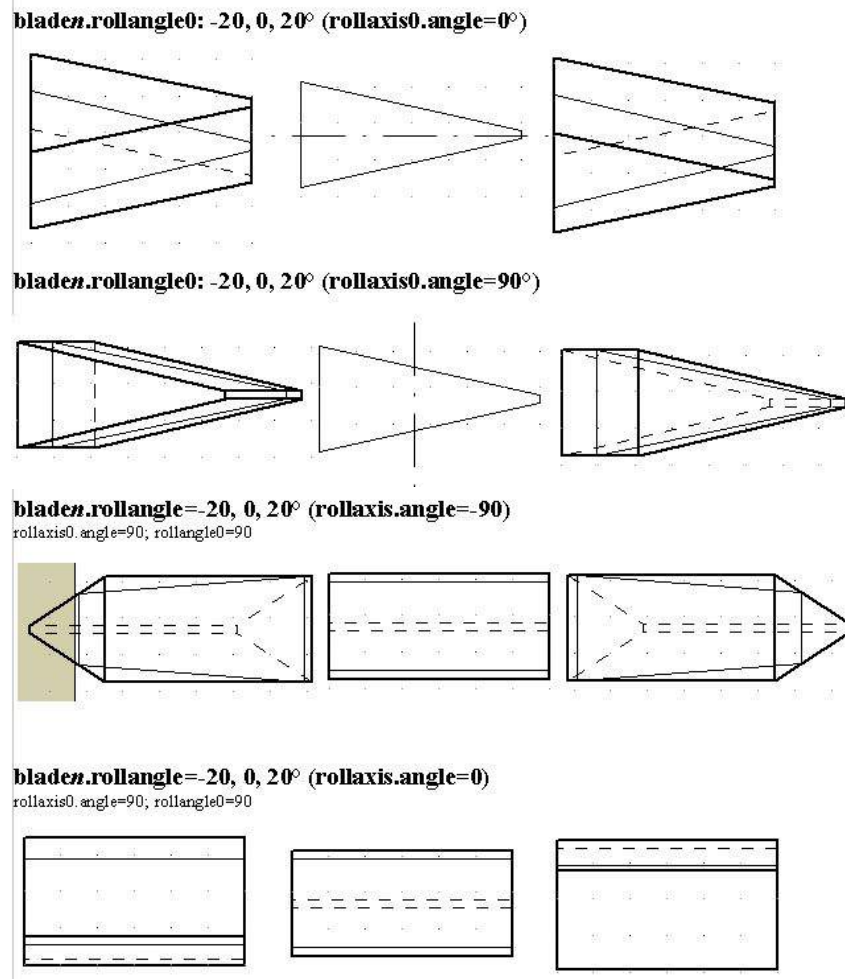


Figure A.2.: IFMSIM prism rotation 1 (top) and rotation 2 (bottom).

A.2. Data analysis script for Igor Pro

For the data treatment, the program 'Igor Pro' from 'WaveMetrics' is used. A special neutron interferometry data analysis script, written by Hartmut Lemmel is used [52], its user interface is depicted in fig. A.3.

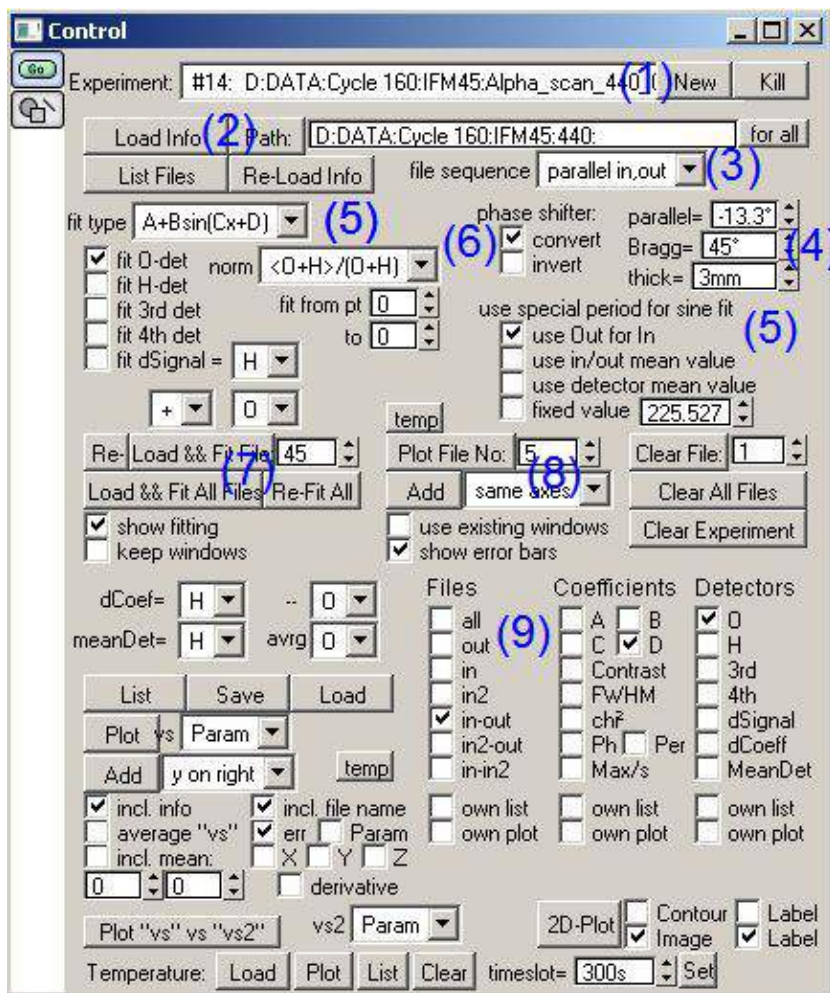


Figure A.3.: Igor panel (H. Lemmel). (1) Choose a data set, (2) load a file (.inf), which lists the data set files, (3) mark this files with IN or OUT according the measurement procedure (chap. 2.3). (4) For the calculations, input the Bragg angle, phase shifter thickness and its parallel (to IFM blade) position. (5) Sine fit function for the interferogram (chap. 2.2.1), its period can be given from another measurement; (6) defines the direction of the phase shifter and shows it in degree or converted in path length difference. (7) Load/fit individual files (.dat) from the data set, (8) plot this files (interferograms). (9) Calculate intensity, phase and contrast of different file/combinations.

A.3. Labview control program

At the instrument S18 all the motors and encoders are controlled via Labview. The program interface (main.vi) is depicted in fig. A.4.

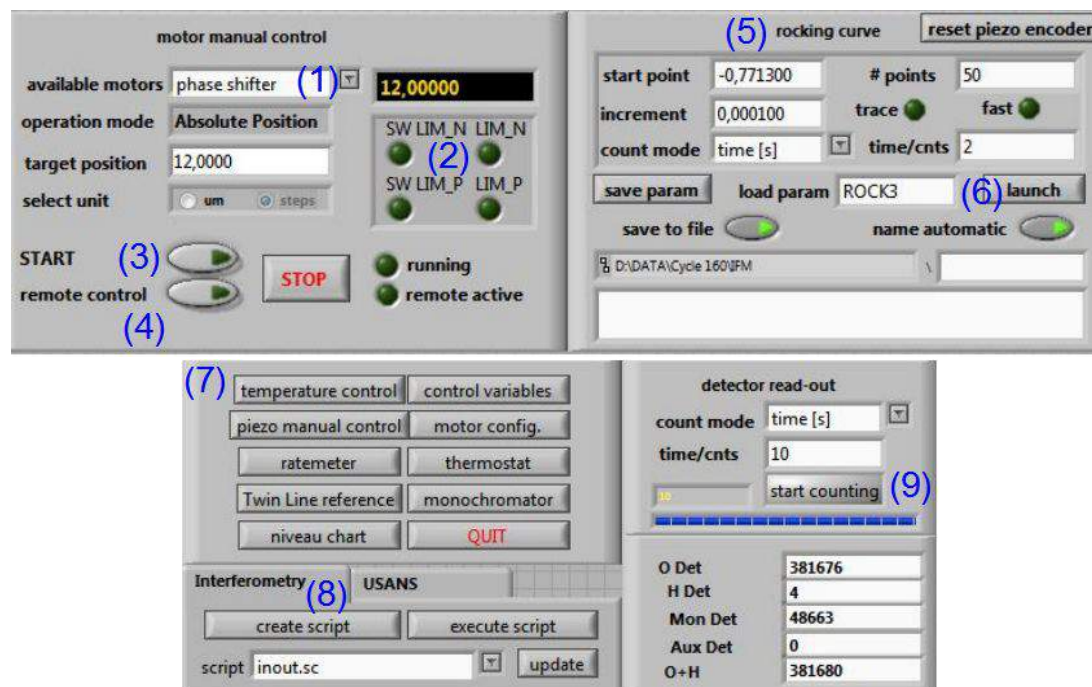


Figure A.4.: S18 Labview control program. (1) Motor selection (also to read out its position), (2) limits for motors (software and hardware), (3) activate motor to a target position or an increment, (4) activate motors with a remote control, (5) 'rocking curve' window with start value, increment, no. of points, and counting time/point, (6) starts the rocking curve, (7) subprograms, (8) automatic measurement procedure can be programmed, (9) manual neutron counts per time for all detectors.

As motor (1) one can select for instance: 'phase shifter', two 'detectors O, H', three 'robots X,Y,Z', three 'elevator left, right, central' (optical table), 'coarse rotation', and 'piezo' (chap. 2.4.5). The monochromator motors however are controlled in the password secured area 'monochromator' (7). Further subprograms e.g. are the 'piezo manual control' to adjust the Bragg angle of the interferometer or 'niveau chart' for the horizontal position of the optical bench (chap. 2.4). Not all subprograms are listed, like the 'raster scan' (chap. A.5) or the recently updated 'Temperature PID Control.vi' (chap. A.5), as well as the program to save the temperature sensor values.

A.4. Interferometer

The used three-loop neutron interferometer (IFM) with its dimensions are given in fig. A.5. The preparation steps from a 4 inch perfect Si crystal ingot are described in [30]. The length is 23.5 cm, the beam separation is 5 cm, all 6 blades are about 3 mm thick and the full enclosed beam area is 100 cm². The lamella height is 5 cm, the basis height 3.4 cm, and the bottom contact surface is 4.8 x 23.5 cm². The lattice planes are precisely oriented, perpendicular to the lamella surfaces (13.5").

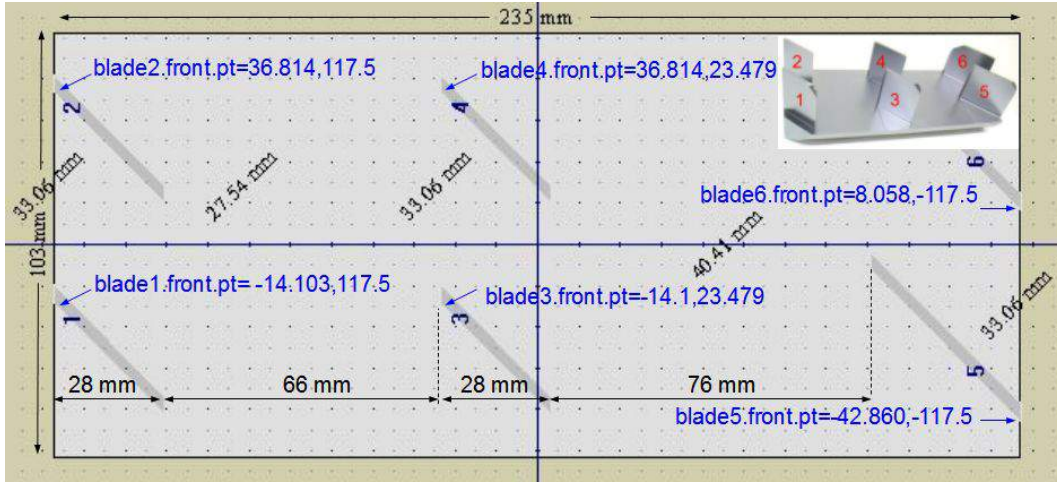


Figure A.5.: Used interferometer for the Laue phase measurement. (1)...(6) Six 0.3 cm thick blades, length 23.5 cm, path length: 25 cm, beam areas: (45 cm², 55 cm², 100 cm²). The black values without arrows are the normal distances between the blades. The blade points for the IFMSIM input are indicated as well. The inset shows the related 3D picture.

After cutting and etching the blade geometry varies a little from the planned values. Tab. A.2 gives an overview of the used geometries in the calculation program. In our case 'ideal' means that only all blade thicknesses are 3 mm, while in general an ideal interferometer is independent of the sample blade thickness.

Table A.2.: Blade thickness in mm, of different interferometer geometries used in IFM-SIM. The blade no. are shown in fig. A.5

blade no.	ideal	real I	real II
1	3	2.941	2.9371
2	3	2.938	2.9337
3	3	2.939	2.9359
4	3	2.939	2.9367
5	3	2.942	2.9379
6	3	2.942	2.9377

Calculation of the real I geometry

The real I geometry is calculated after a $10.25 \mu\text{m}$ etching process on 05.12.2008 and a geometry measurement on 19.08.2008. In this geometry the deviation of the individual blade thickness is of up to $4 \mu\text{m}$ from each other. The sample blade 3 and 4 are equal thick. The calculated values for the IFMSIM input are given in fig. A.5 (blade length: 38 mm and 52 mm). The measurements in chap. 2.4.1 of the phase versus rocking angle favors the real I geometry over real II.

Geometry measurement, real II geometry

The real II geometry is taken from a measurement with the 'MITUTOYO Strato-Apex 9106' CNC machine at 'Gerhard Rauch Ges.m.b.H.'¹ on 26.06.2013. This coordinate measuring machine has a ruby sensor sphere, which touches the surface with 10 grams, see fig. A.6 (left). The thickness of the blades are measured at several points in an area at half blade height. The points are 1.25 cm separated from each other, its positions on the blades and the incident neutron beam are depicted in fig. A.6 (right).

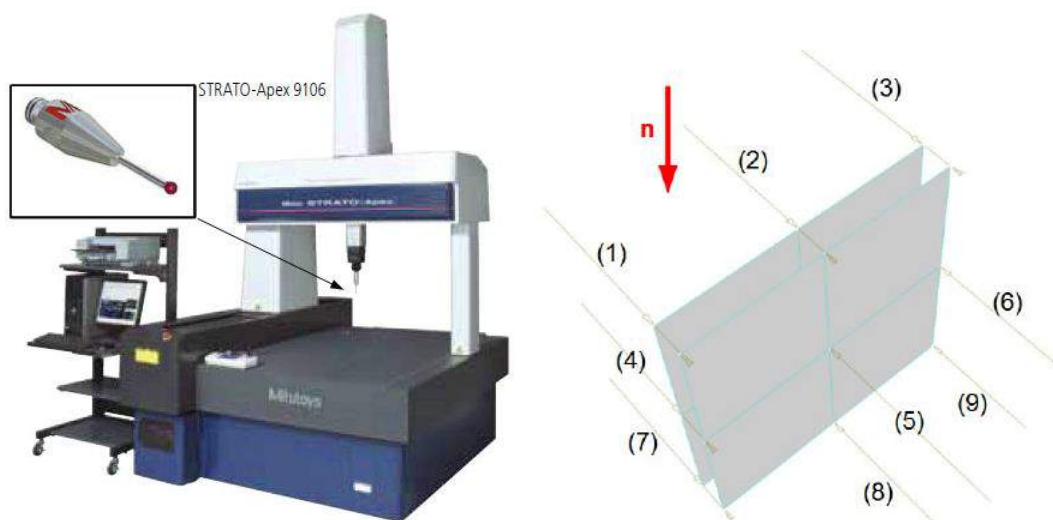


Figure A.6.: Interferometer geometry measurement. (left) Coordinate measuring machine Strato-Apex 9106, the inset shows the ruby sensor sphere (picture from Mitutoyo manual). (right) The blade thickness is taken at a $25 \times 25 \text{ mm}^2$ area on the blade surface.

Tab. A.3 shows the result of this measurement with an accuracy of $0.9 \mu\text{m}$. The largest deviation at the same height is: position (1)...(3) $7.8 \mu\text{m}$, (4)...(6) $6.1 \mu\text{m}$, and (7)...(9) $4.8 \mu\text{m}$. The overall largest deviation is $8.5 \mu\text{m}$. The distances between the blades (at position 5) are shown as well in tab. A.4 . The deviation of the blade pairs 1 - 2, 3 - 4, and 5 - 6 is $1.1 \mu\text{m}$, $2.7 \mu\text{m}$, and $3.8 \mu\text{m}$ from each other.

¹Eitnergasse 9, 1230 Wien

Table A.3.: Measurement of the interferometer blade thicknesses. Taken at 12.5 mm separated 3 x 3 points on the blade surface (fig. A.6). Values in mm, accuracy 2 x 0.9 μm . The blade no. are depicted in fig. A.5. A graphical representation is given in fig. 2.16. The largest thickness difference is 8.5 μm (blade 6-1, blade 2-9).

position	blade 1	blade 2	blade 3	blade 4	blade 5	blade 6
1	2.9395	2.9345	2.9366	2.9379	2.9382	2.9413
2	2.9400	2.9340	2.9367	2.9375	2.9395	2.9411
3	2.9405	2.9335	2.9368	2.9371	2.9408	2.9409
4	2.9366	2.9342	2.9358	2.9371	2.9366	2.9379
5 (average)	2.9371	2.9337	2.9359	2.9367	2.9379	2.9377
6	2.9376	2.9331	2.9360	2.9363	2.9392	2.9375
7	2.9337	2.9338	2.9350	2.9363	2.9350	2.9345
8	2.9342	2.9333	2.9351	2.9359	2.9363	2.9343
9	2.9347	2.9328	2.9352	2.9355	2.9376	2.9341

Table A.4.: Measurement of the distances between the interferometer blades. The deviation of the blade pairs 1 - 2, 3 - 4, and 5 - 6 is 1.1 μm , 2.7 μm , and 3.8 μm from each other. The blade no. are shown in fig. A.5.

between blades	normal distance / mm
1 - 2	33.0696
2 - 3	27.5406
3 - 4	33.0658
4 - 5	40.4055
5 - 6	33.0669

The calculated IFMSIM values are: 'blade1.front.pt=-14.19135,117.5', 'blade2.front.pt=36.81875,117.5', 'blade3.front.pt=-14.19135,23.299', 'blade4.front.pt=36.81875,23.299', 'blade5.front.pt=-42.59565,-117.5', 'blade6.front.pt=8.41445,-117.5'.

A.5. Temperature setup

During our measurements the temperature is recorded and can be changed, in order to yield an optimal contrast. The temperature of the guide hall varies during day and night about two-three degrees, the concrete walls of the experiment room are damping this temperature oscillation. Also the temperature of the monochromator within the neutron guide can be recorded (fig. A.7 left). For neutron interferometry this are not optimal conditions, for instance in [33] an Al skin around the IFM was tested, here we build a box around the interferometer (fig. A.7 right). The box is made of Al, its walls are 60 x 45 x 0.6 cm³. The bottom of the box is standing without an extra wall directly on the optical bench, on the top is a lid made of plastic, it can be easily removed for sample manipulations. The temperature change without the box is $\pm 0.01^\circ\text{C}$ and in the box center $\pm 0.002^\circ\text{C}$ within 1 h.

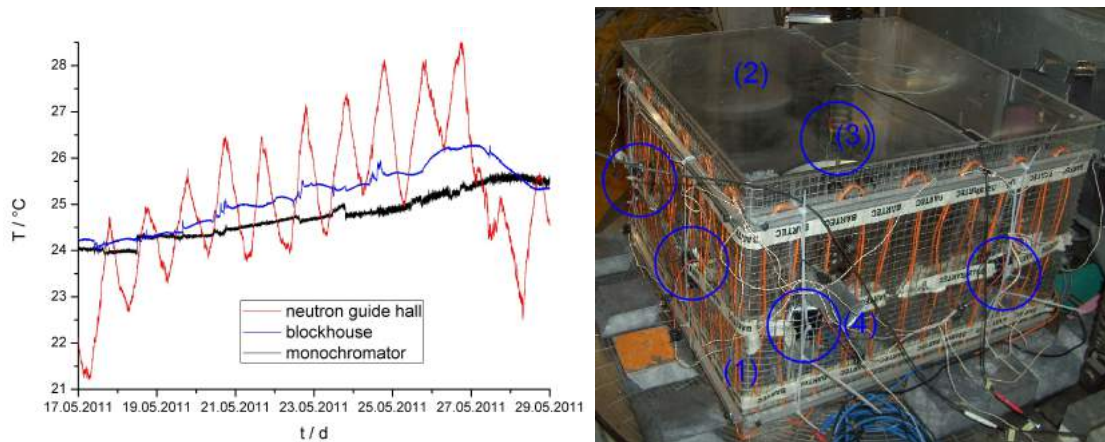


Figure A.7.: (left) Rough temperature conditions at S18 within several days. (right) Temperature box (1) with plastic lid (2), temperature sensor (3), and 2 Peltier elements on each box wall (4).

Additionally to the Al box itself, two different temperature control mechanisms can be used: heating mat and Peltier elements.

The heating mat is arranged around the box and below the optical bench (BARTEC Duennbettheizung, 210 x 45 cm² with 150 W/m²). The current can be changed with a dimmer (Phase-angle dimmer NS80 and NS68K, 2200 W) and a PID control loop in the S18 Labview control program (chap. A.3). It creates a control voltage at the PC output/dimmer input of 0...10 V. The PID values with the sensor on the IFM basis are: P=2246.6, I=5.95, D=1.19.

The mat is restricted to heating only, an alternative active stabilization system is implemented as well. It consists of eight Peltier elements (PE) for cooling and heating (two are placed at each box wall), arranged as depicted in fig. A.8 and a temperature controller for the control loop. On the 40 x 40 mm² Peltier elements² (max. $\pm 2...6$ A) are heat sinks sticking. The temperature controller LFI-3751 (PID control loop, <0.002 K temperature stability, max. ± 5 A, 40 W) can be connected to the S18 Labview control system. Its possible to save the temperature values in the measuring files and change the set temperature for the control loop as well as current limits, PID values and sensor calibration data [35]. The PID Autotune process yields $P=100$, $I=0.4$, $D=100$. With this setup a heating of 2.5°C and a cooling of 0.1°C is possible. The current limit is set to $-4/+0.8$ A. The temperature sensors are NTC thermistors (Wavelength Electron-

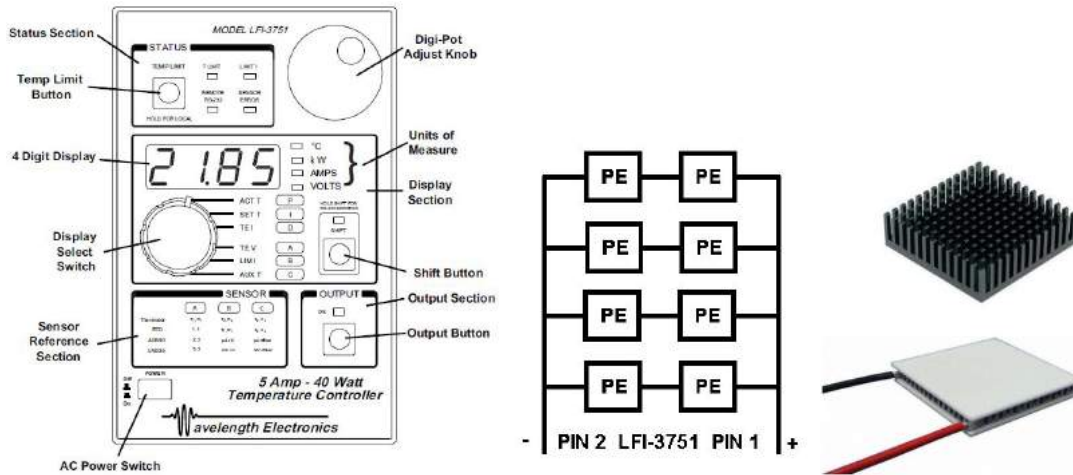


Figure A.8.: (left) Overview temperature controller, front panel, picture from [35].
(middle) Connection of 8 PE. (right) PE with heat sink.

ics TCS-605, ± 1 mK), which can be placed freely. The resistance R is changing with temperature T/K according to the Steinhart-Hart eq. [51]:

$$\frac{1}{T} = A + B \cdot \ln(R) + C \cdot (\ln(R))^3 \quad (\text{A.1})$$

The coefficients A , B and C are calculated by entering three temperature/resistance data pairs³. The setup is extended with additional temperature sensors PT1000 (platinum resistor, $\pm 1...2$ mK), due to the limitation of only two sensors on the LFI-3751. The sensor electronics (PT1000 Messumformer module, output: $0...10$ V, Hygrosens Instruments G.m.b.H) are implemented and connected to the S18 Labview control system. A measurement for the active and non-active control is given within 10 hours in fig. A.9. The sensor is placed on the inner side of the box wall. If the Peltier element control is switched off, the temperature increases about 0.04°C within this time. If the PE control is switched on, the temperature is stable within $\pm 0.005^{\circ}\text{C}$ ⁴.

²TEC (thermoelectric cooler) from Quick-Ohm Kuepper & Co. G.m.b.H

³TSC-605: A: 10°C , 9.950 k Ω ; B: 20°C , 6.245 k Ω ; C: 30°C , 4.028 k Ω

⁴In both cases the temperature of the experimental room changes about 0.1° .

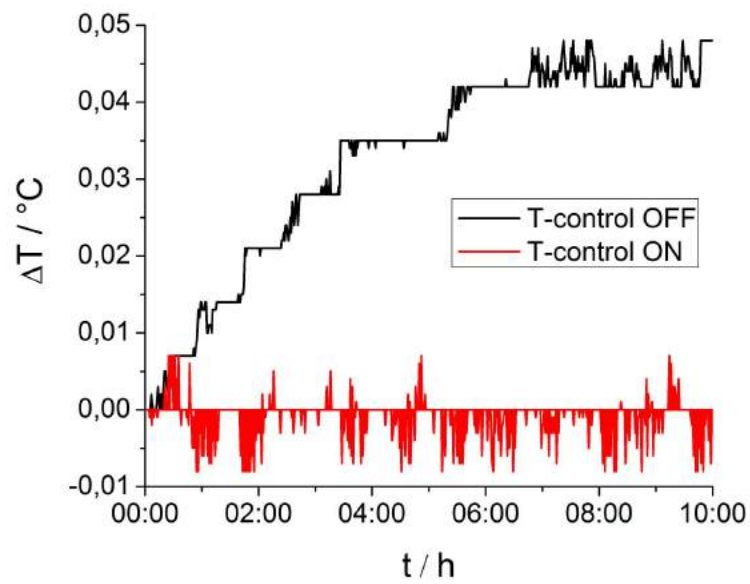


Figure A.9.: Temperature with/without active PE control within 10 h.

Alignment

Due to other experiments at S18 our setup has to be build up and adjusted for every measurement run. The alignment of a large interferometer with all its components, described in chap. 2.2.1 is time consuming. It begins with the adjustment of the monochromator Bragg angle, for this, the optical bench has to be moved to the correct position, as depicted in fig. A.10⁵. The monochromator crystal can be rotated and moved with motors in several directions until the beam, aperture and detector are in position. The reproducibility of the Bragg angle between the different measurement runs is about $(45 \pm 0.25)^\circ$.

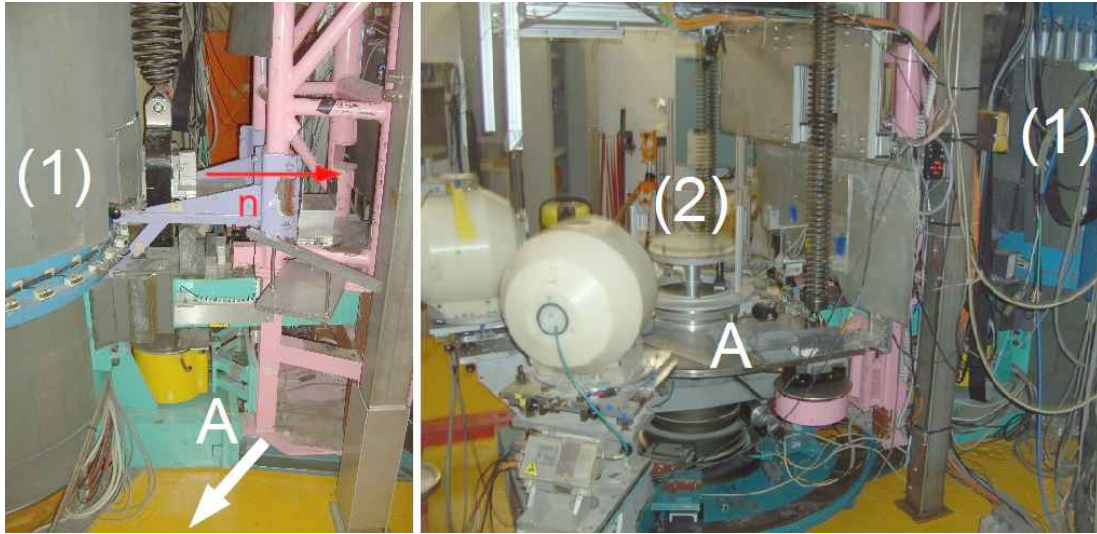


Figure A.10.: Bragg angle alignment. (A) The whole optical bench and frame can be moved to change the take off angle, (1) shutter, (2) interferometer table; n is the neutron beam.

The height of the interferometer table (2) and its support has to be chosen in order that the neutrons are able to pass through the interferometer blades at the preferred area. The angle of the interferometer relative to the beam is then adjusted to the correct Bragg angle (rocking angle). The ρ -axis angle (tilt of the interferometer versus the monochromator) is changed to the smallest rocking curve (fig. A.11, 2.10). With the ρ lever arm of 16.3 cm the ρ angle amounts to 0.07° (0.2 mm) and 0.14° (0.4 mm). The peak maximum position (Gauss fit) is 0.0007° (0.2 mm) and 0.0019° (0.4 mm) separated from the $\rho = 0$ mm position. The six fore-prisms are placed in front of the aperture. Then the phase shifter is mounted in the interferometer, parallel to the lamella, as shown in fig. A.12. Mechanical switches should prevent damages of the interferometer, if motors would not stop. Fig. A.13 shows for example the phase shifter limit switches. The optical bench with all this components is moved in horizontal position with motors. With the 'raster scan', the beam position is changed at different x-z positions (small aperture size), in order to optimize the intensity, phase and contrast.

⁵Due to radiation protection reasons this procedure needs permission from the ILL.

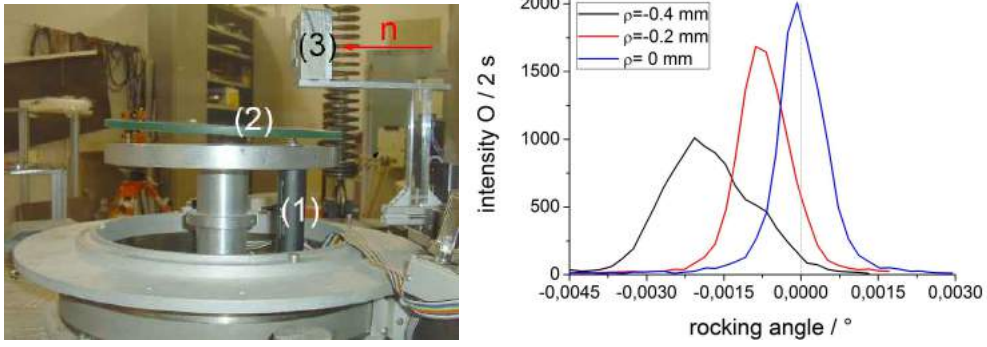


Figure A.11.: ρ -axis angle, (left) (1) ρ -axis motor (PI M-235 linear actuator, Push/Pull Load 120 N, min. incremental motion to $0.1 \mu\text{m}$), (2) tilt of the empty interferometer table, (3) aperture. (right) Rocking curves at different ρ -axis angles. FWHM = 0.00098° (0 mm), 0.00112° (0.2 mm) and 0.00203° (0.4 mm). Aperture: $26 \times 26 \text{ mm}^2$, (220) Bragg peak.

In case of low contrast due to crystal strains, the support has to be changed (see fig. A.12), e.g. position change of a small piece of paper below the IFM, as well as vibrations and temperature influences have to be taken into account. Now the Al prisms can be placed into the interferometer, a maximal rotation angle of the prisms within the beam must be possible⁶. The detectors have to be in a horizontal position and its windows should be as small as possible. The neutron flux (O+H detector) with all components (interferometer, fore-prisms, $5 \times 5 \text{ mm}^2$ aperture) reduces finally to $\approx 400 \text{ n/s}\cdot\text{cm}^2$ as listed in tab. A.5. The optimal alignment is characterized by maximal contrast and intensity. Unfortunately, the complete alignment procedure costs a lot of time, and reduces the effective measurement time immense.

Table A.5.: Typical neutron flux during the alignment at S18.

	Neutron flux /s·cm ² (O+H detector)
In the reactor core	$1.5 \cdot 10^{15}$
In the beam guide	$3.5 \cdot 10^9$
Direct beam from monochromator, $\theta_B = 45^\circ$	14000
IFM, without fore prisms	1000
IFM, fore prisms (220)	400
IFM, fore prisms (440)	200

⁶The prisms are not mounted on the vibration reduced bench, a damage of the IFM can happen very easily.

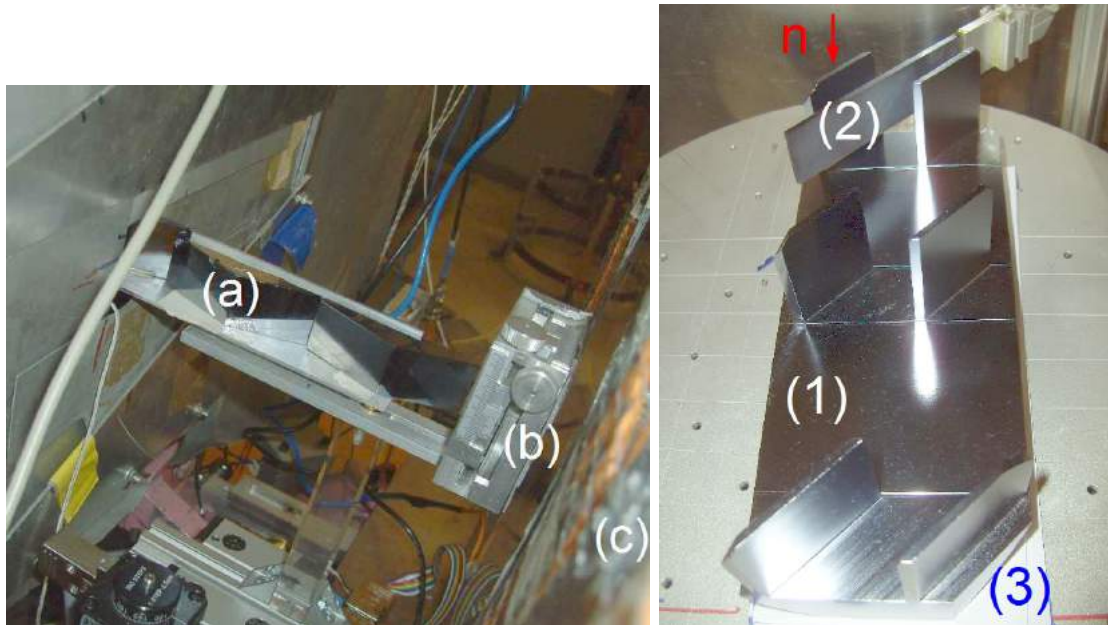


Figure A.12.: (left) Si fore prism mounting (a) in front of the aperture (b); the IFM is placed in the Al box (c). (right) IFM (1) with mounted phase shifter (2), IFM support (3): 10...20 layers of paper to optimize the contrast.

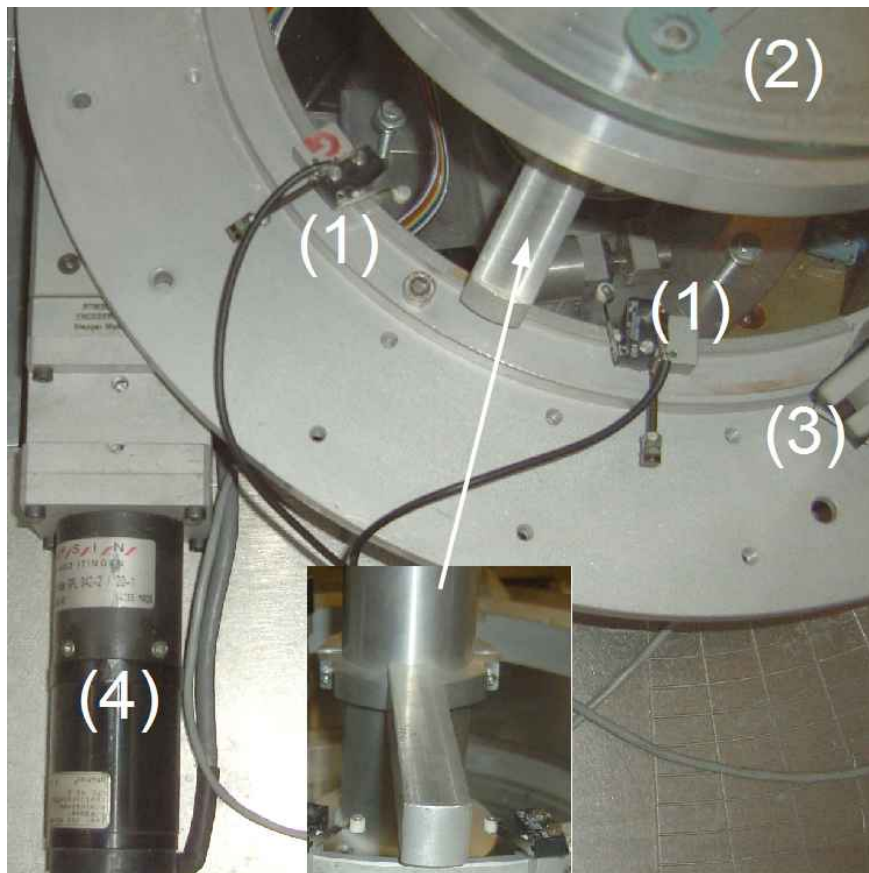


Figure A.13.: Phase shifter limit switches (1) below the interferometer table (2) do prevent accidents. The phase shifter is mounted on this metal ring (3) its rotation is performed by the motor (4).

A.6. Determination of σ_θ with rocking curves

Here we consider the empty interferometer without the Al prisms. We perform rocking curves, where we record the intensity as well as the phase versus the rocking angle (fig. 2.34). Due to a strong dependence of these curves on the beam divergence σ_θ we use measured rocking curves for a determination of σ_θ . For a comparison of the calculated and measured rocking curves, the height of the peaks are scaled with its areas, see chap. 2.4.4. The determined σ_θ values are smaller than the typically beam divergence in the experiment $\sigma_\theta = 900''$, because no wavelength distribution (monochromatic) is included in our calculations. The influence of the geometry on the rocking curve intensity is small but strong for the phase.

σ_θ for ρ -axis angle 0°

The intensity versus the rocking angle is given for Gauss, Square and Bragg in fig. A.14. The best match with the measured data amounts to $\sigma_\theta = 1.62(18)''$ (Gauss), $\sigma_\theta = 1.80(18)''$ (Square) and Darwin width = 1 (Bragg). The phase versus the rocking angle is given for all three monochromator functions in fig. A.15. The phase shows a strong influence on the interferometer's geometry as well (chap. 2.4.1). For the ideal interferometer this rocking phase is zero for all beam divergences. The obtained σ_θ values from the phase are in agreement with the σ_θ obtained from the intensity.

σ_θ for ρ -axis angle 0.09°

Additional, σ_θ for a different ρ value (the rocking curve is two times wider) is determined in fig. A.16 for Gauss, Square and Bragg. The best match are about three times the value at $\rho = 0^\circ$: $\sigma_\theta = 4.14(54)''$ and Darwin width = 3.0(2).

σ_θ for different Bragg peaks

The determination of the beam divergence is repeated for the (440) and (660) Bragg peak (for the Gauss monochromator function). A 50 s/point measurement yields $\sigma_\theta = 0.32(10)''$ and $\sigma_\theta = 0.34(20)''$, respectively.

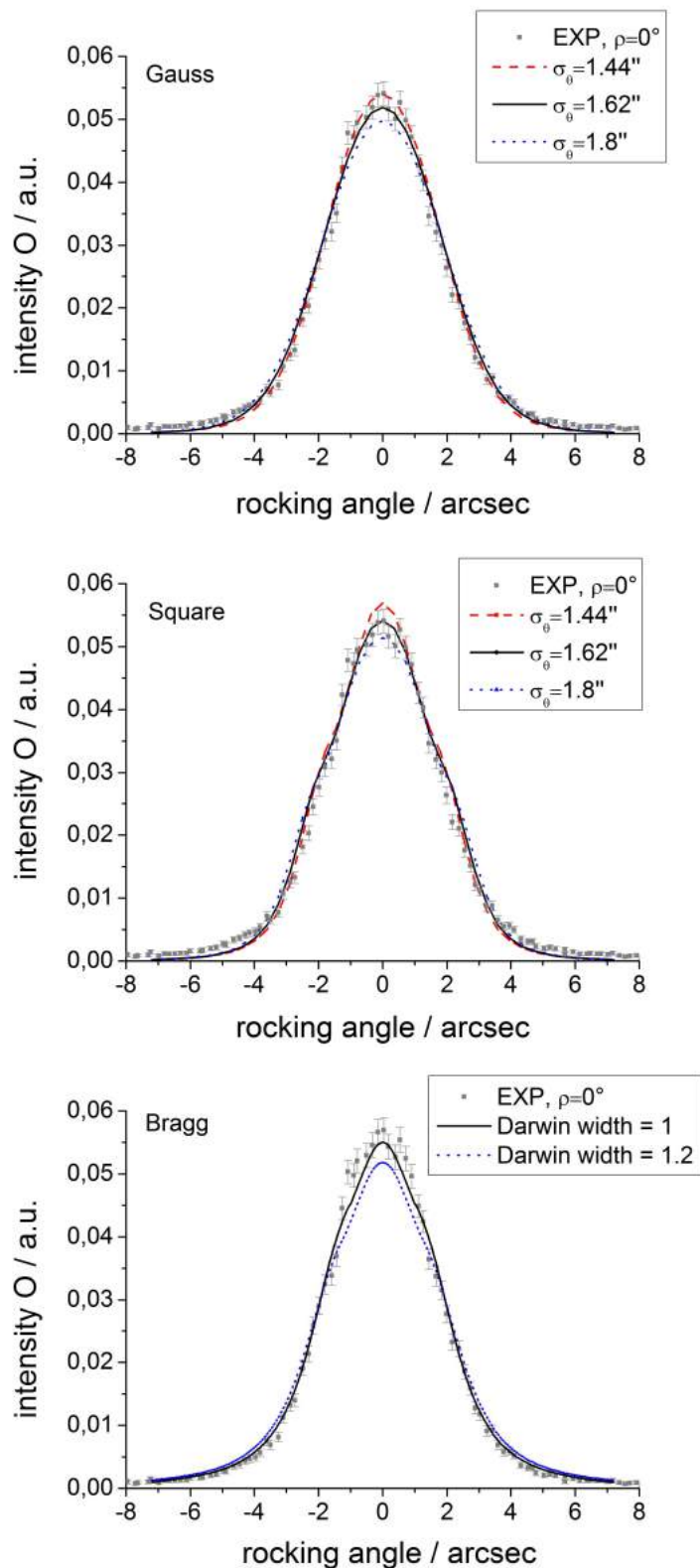


Figure A.14.: Determination of the beam divergence (monochromatic) from the rocking intensity. Gauss 1.62(18)'' (top), Square 1.80(18)'' (middle) and Bragg Darwin width = 1 ... 1.2 (bottom). Parameters: (220) case, real I geometry, experimental values (EXP): 60 s/point.

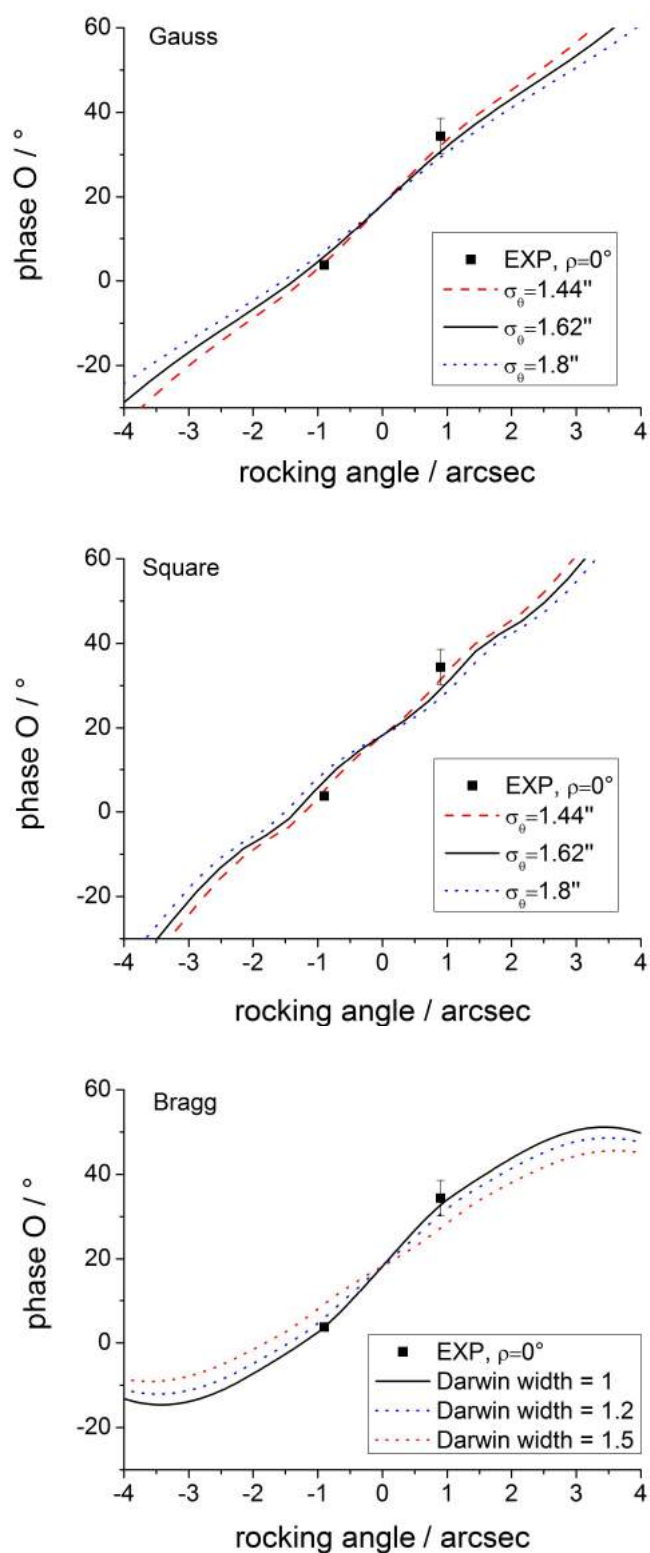


Figure A.15.: Determination of the beam divergence (monochromatic) from the rocking phase. Gauss $1.62(18)''$ (top), Square $1.80(18)''$ (middle) and Bragg Darwin width = 1...1.2 (bottom). Same parameters as in fig. A.14. The measurements are taken from chap. 2.4.1.

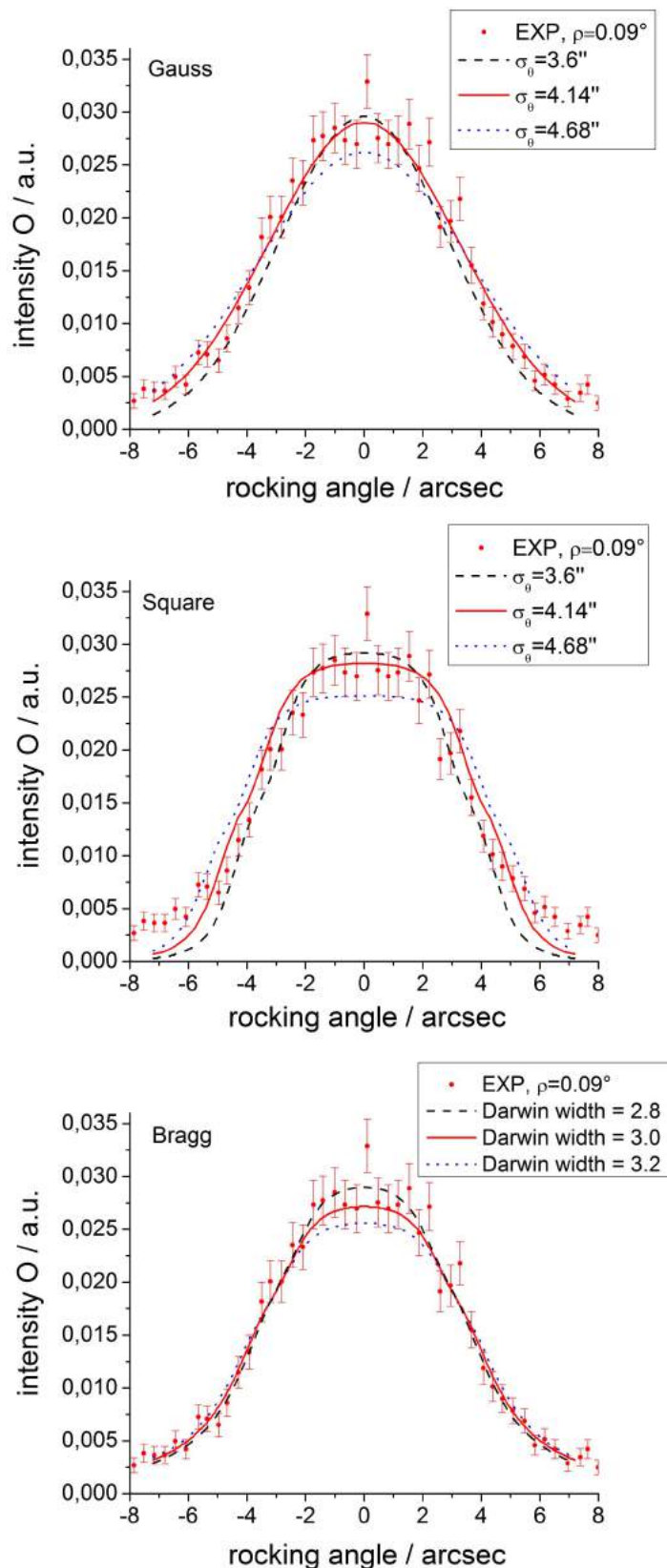


Figure A.16.: Determination of the beam divergence (monochromatic) from the rocking intensity for $\rho = 0.09^\circ$. Gauss 4.14(54)'' (top), Square 4.14(54)'' (middle) and Bragg Darwin width = 3.0(2) (bottom). Same parameters as in fig. A.14, EXP: 10 s/point.

A.7. Rocking position, further influences

Further influences on the contrast behavior at a rocking angle deviation are discussed in the following (chap. 2.4.5). **Geometry:** a comparison of the different geometries is given in fig. A.17 (left). The measurement favors the 'real I' IFM geometry in agreement with fig. 2.21. Furthermore, as already mentioned, the IFM with ideal geometry does not show a $\delta\theta$ -shift of the contrast peak maximum (at a rocking angle deviation). Additionally, the phase slope (around $\delta\theta = 0''$) are calculated for all possible rocking positions in fig. A.17 (right). It does not show a strong sensitivity to the IFM geometry and rocking angle within pos. $\pm A$. **Beam divergence:** a comparison of the different Darwin widths for rocking pos. -B is given in fig. A.18 (left). The shift is decreasing with increasing Darwin width. The measurement of the contrast and phase (not shown) is within a Darwin width of 1...1.2. **Monochromator function:** a comparison of the different monochromator functions for rocking pos. -B is given in fig. A.18 (right). The measurements favors the Bragg curve (chap. 2.4.3).

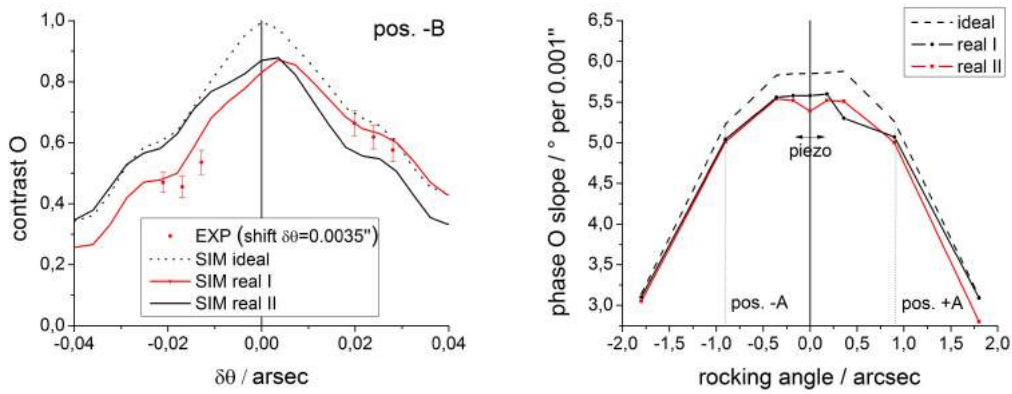


Figure A.17.: (left) Contrast behavior at rocking pos. -B, for different IFM geometries. The measurement favors the 'real I' geometry. (right) Laue phase slope for all rocking positions.

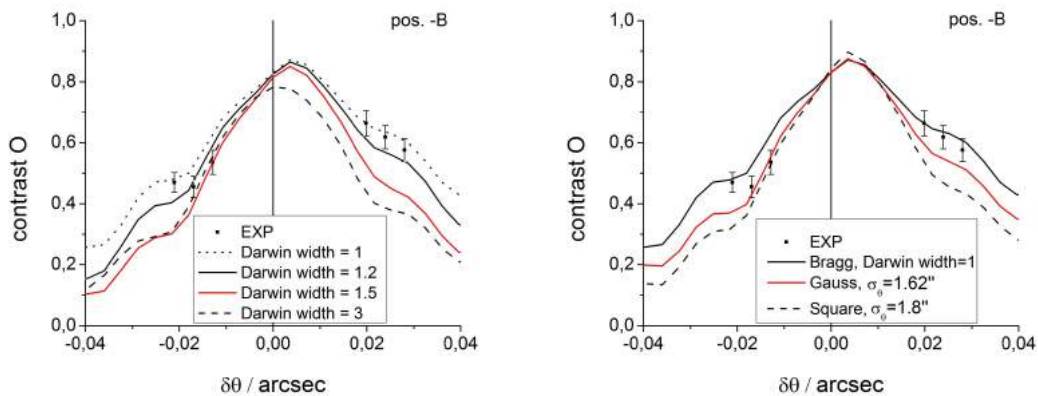


Figure A.18.: Contrast behavior at different rocking positions. Comparison of the Darwin width (left) and different monochromator functions (right) at pos. -B. All experimental values are shifted by $\delta\theta = 0.0035''$ acc. to chap. 2.3.

A.8. Scattering length tables

Here we calculate the Laue phase change $\Delta\phi$ resulting from two different b_{ne} values (chap. 2.4.8). The results for the interferometer with the 'real I' geometry are listed in tab. A.6 ... A.8. To see the interferometer's geometry influence, the results for 'real II' geometry are in tab. A.9 ... A.11. The calculations are performed for different Bragg peaks. The maximal number of plateaus are from the prism rotation up to $\alpha = 90^\circ$, but note that the prisms range in our experiment is limited to $\pm 15^\circ$. Different prism apex angle or prism material could extend the beam deflection range. The plateau positions can also be found in tab. 2.11. In comparison to the reached phase accuracy from the different parameters in chap. 2.4, one can say conclusive that this effect is too small for this method, even if the contrast in the measurements reaches the theoretical maximal value. The achieved phase accuracies in the experiment are: $\pm 9^\circ$ (1st plateaus) and $\pm 15^\circ$ (2nd plateaus), for the (220) case according to chap. 2.3.

Table A.6.: Laue phase change $\Delta\phi$ due to b_{ne} uncertainty. For several Pendelloesung plateaus, Bragg peak (220) and real I geometry; α is the rotation angle of the 25° prisms.

plateau no.	plateau at $\delta\theta'''$	$\alpha/^\circ$ (220)	contrast/% SIM	contrast/% EXP (max. 20%)	O-beam $\Delta\phi/^\circ$
$\pm 1^{st}$	0.025	6.1	34	6.8	0.20
$\pm 2^{nd}$	0.045	11.0	16	3.2	0.45
$\pm 3^{rd}$	0.062	15.1	9	1.8	1.00
$\pm 4^{th}$	0.081	20.1	4	0.8	1.80
$\pm 5^{th}$	0.100	25.1	2	0.4	3.00
$\pm 6^{th}$	0.123	31.3	1.6	0.3	3.50
$\pm 7^{th}$	0.158	41.9	2	0.4	1.70
$\pm 8^{th}$	0.231	78.2	3	0.6	3.50

Table A.7.: Laue phase change $\Delta\phi$ due to b_{ne} uncertainty. For several Pendelloesung plateaus, Bragg peak (440) and real I geometry; α is the rotation angle of the 25° prisms.

plateau no.	plateau at $\delta\theta'''$	$\alpha/^\circ$ (440)	contrast/% SIM	contrast/% EXP (max. 20%)	O-beam $\Delta\phi/^\circ$
$\pm 1^{st}$	0.012	11.2	32	6.4	0.3
$\pm 2^{nd}$	0.023	22.4	18	3.6	0.6
$\pm 3^{rd}$	0.035	35.8	8	1.6	2.5

Table A.8.: Laue phase change $\Delta\phi$ due to b_{ne} uncertainty. For several Pendelloesung plateaus, Bragg peak (660) and real I geometry; α is the rotation angle of the 25° prisms.

plateau no.	plateau at $\delta\theta'''$	$\alpha/^\circ$ (660)	contrast/% SIM	contrast/% EXP (max. 20%)	O-beam $\Delta\phi/^\circ$
$\pm 1^{st}$	0.008	16.8	37	7.4	1.0
$\pm 2^{nd}$	0.015	33.9	18	3.6	3.0
$\pm 3^{rd}$	0.021	52.0	5	1.0	4.7

Table A.9.: Laue phase change $\Delta\phi$ due to b_{ne} uncertainty. For several Pendelloesung plateaus, Bragg peak (220) and real II geometry; α is the rotation angle of the 25° prisms.

plateau no.	plateau at $\delta\theta''$	$\alpha/^\circ$ (220)	contrast/% SIM	contrast/% EXP (max. 20%)	O-beam $\Delta\phi/^\circ$
$\pm 1^{st}$	0.025	6.1	36	7.2	0.1
$\pm 2^{nd}$	0.045	11.0	15	3.0	0.05
$\pm 3^{rd}$	0.062	15.1	11	2.2	1.7
$\pm 4^{th}$	0.081	20.1	2.0	0.4	4.3
$\pm 5^{th}$	0.123	31.3	0.5	0.4	4.4
$\pm 6^{th}$	0.154	40.7	3.0	0.1	15
$\pm 7^{th}$	0.175	47.9	0.8	0.6	6

Table A.10.: Laue phase change $\Delta\phi$ due to b_{ne} uncertainty. For several Pendelloesung plateaus, Bragg peak (440) and real II geometry; α is the rotation angle of the 25° prisms.

plateau no.	plateau at $\delta\theta''$	$\alpha/^\circ$ (440)	contrast/% SIM	contrast/% EXP (max. 20%)	O-beam $\Delta\phi/^\circ$
$\pm 1^{st}$	0.012	11.2	32	6.4	0.2
$\pm 2^{nd}$	0.023	22.4	17	3.4	0.1
$\pm 3^{rd}$	0.035	35.8	7.5	1.5	7.0

Table A.11.: Laue phase change $\Delta\phi$ due to b_{ne} uncertainty. For several Pendelloesung plateaus, Bragg peak (660) and real II geometry; α is the rotation angle of the 25° prisms.

plateau no.	plateau at $\delta\theta''$	$\alpha/^\circ$ (660)	contrast/% SIM	contrast/% EXP (max. 20%)	O-beam $\Delta\phi/^\circ$
$\pm 1^{st}$	0.008	16.8	34	6.8	1
$\pm 2^{nd}$	0.015	33.9	20	4.0	2
$\pm 3^{rd}$	0.021	52.0	0.7	0.1	16

A.9. New interferometer: geometry measurement

Within this work a new neutron interferometer is fabricated with our co-operation partner at the 'Physikalisch- Technische- Bundesanstalt' (PTB), chap. 3. After grinding the quality of the geometry was measured at Rauch company in Vienna. Tab. A.12 lists the blade thicknesses. Due to this large thickness differences, this interferometer would be defocused (e.g. $29.5 \mu\text{m}$ between blade 2 and 6, at position 4). Therefore, a fine-grinding at Rauch company was performed⁷. The subsequent geometrical measurement gives a better result, as listed in tab. A.13 (blade thicknesses) and tab. A.14 (blade distances). Input of this geometry values in IFMSIM results in a maximal visibility of about 70%.

⁷Only 18 mm (from the top) of the 20 mm blades are grinded.

Table A.12.: Interferometer geometry measurement, after grinding at PTB 24.10.2014. The blade thicknesses (in mm) are taken at 3 x 3 points on the blade surface, similar to fig. A.6 but the separation in length is 12 mm and in height 5 mm. The blade no. are shown in fig. 3.7.

position	blade 1	blade 2	blade 3	blade 4	blade 5	blade 6
1	3.0892	3.0784	15.0864	15.1024	3.1055	3.1018
2	3.0932	3.0811	15.0899	15.1012	3.0988	3.1009
3	3.0970	3.0834	15.0918	15.0990	3.0984	3.1018
4	3.0904	3.0792	15.0866	15.1024	3.0994	3.1087
5	3.0900	3.0794	15.0883	15.0999	3.0994	3.1046
6	3.0941	3.0812	15.0937	15.0956	3.1000	3.1032
7	3.0948	3.0822	15.0901	15.1009	3.1002	3.1097
8	3.0923	3.0810	15.0914	15.0974	3.1018	3.1092
9	3.0894	3.0788	15.0924	15.0979	3.1040	3.1071

Table A.13.: Interferometer geometry measurement, after grinding at Rauch company 07.11.2014. Parameters: see tab. A.12.

position	blade 1	blade 2	blade 3	blade 4	blade 5	blade 6
1	3.0349	3.0369	15.0475	15.0476	3.0362	3.0377
2	3.0353	3.0371	15.0486	15.0479	3.0368	3.0373
3	3.0357	3.0381	15.0481	15.0481	3.0367	3.0374
4	3.0350	3.0370	15.0486	15.0483	3.0366	3.0372
5	3.0350	3.0377	15.0480	15.0485	3.0364	3.0366
6	3.0346	3.0386	15.0488	15.0479	3.0368	3.0375
7	3.0348	3.0370	15.0489	15.0485	3.0361	3.0367
8	3.0349	3.0381	15.0486	15.0483	3.0361	3.0365
9	3.0339	3.0377	15.0482	15.0477	3.0356	3.0362

Table A.14.: Interferometer geometry measurement (07.11.2014): blade distances.

between blades	normal distance / mm
1 - 2	37.9692
5 - 6	37.9642
1 - 5	181.6626
2 - 6	181.6563

A.10. Chameleon method II: wall thickness

The measured phase in fig. 4.13 behaves like an additional Al material of up to $12\ \mu\text{m}$ in one beam. Fig. A.19 shows the obtained phase from Al in either beam I or II versus the thickness. The wall thicknesses have been measured along the x-axis (fig. A.20). The thickness change of each wall is given in fig. A.21. The neutron beam pass through both walls, therefore the sum of this two walls are shown in fig. A.22.

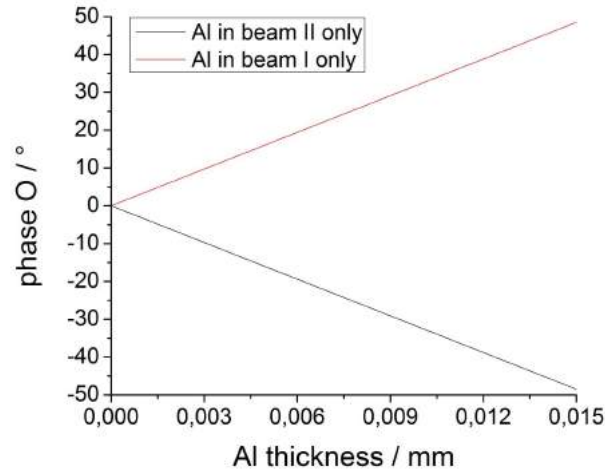


Figure A.19.: Phase vs. Al thickness in only one interferometer path. The measured phase of up to 40° is equal to $12\ \mu\text{m}$ additional Al between the robot X-positions 177 mm and 205 mm.

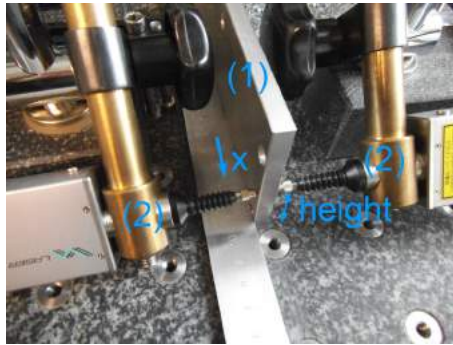


Figure A.20.: Principle of the chamber wall thickness measurement. (1) One of the two chamber walls at a specific x-position. (2) Springs pressing the sensors on the sample.

The total thickness difference is in the range of $10\ \mu\text{m}$ (between $X=177\ \text{mm}$ and $205\ \text{mm}$), and can therefore explain the measured phase in chap. A.10.

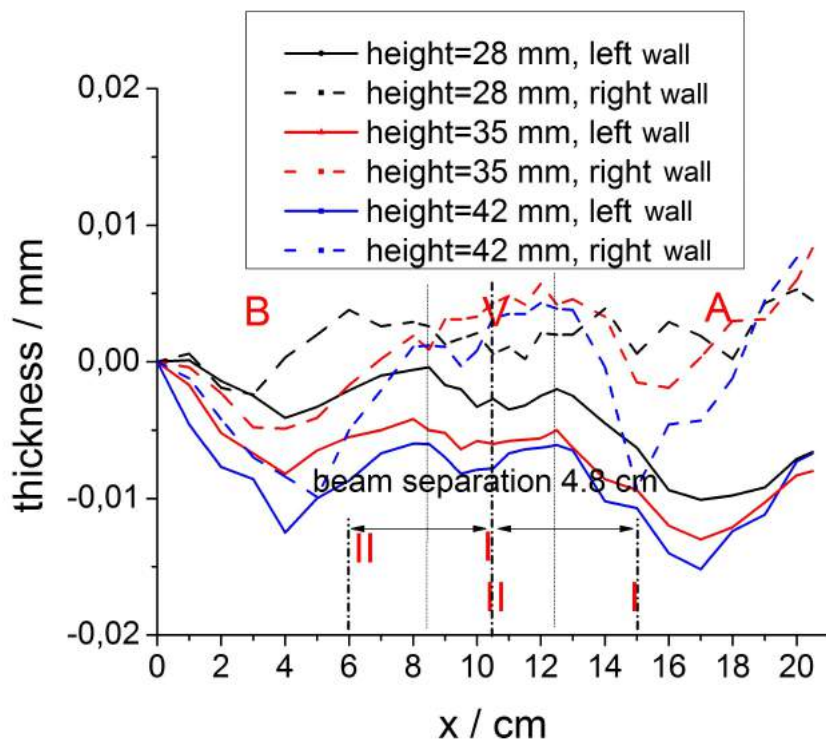


Figure A.21.: Measurement of the thickness profile of the outer chamber walls. The neutron beam pass through the right (fig. 4.5) wall first at a height of 22 ...28 mm (6 mm high aperture).

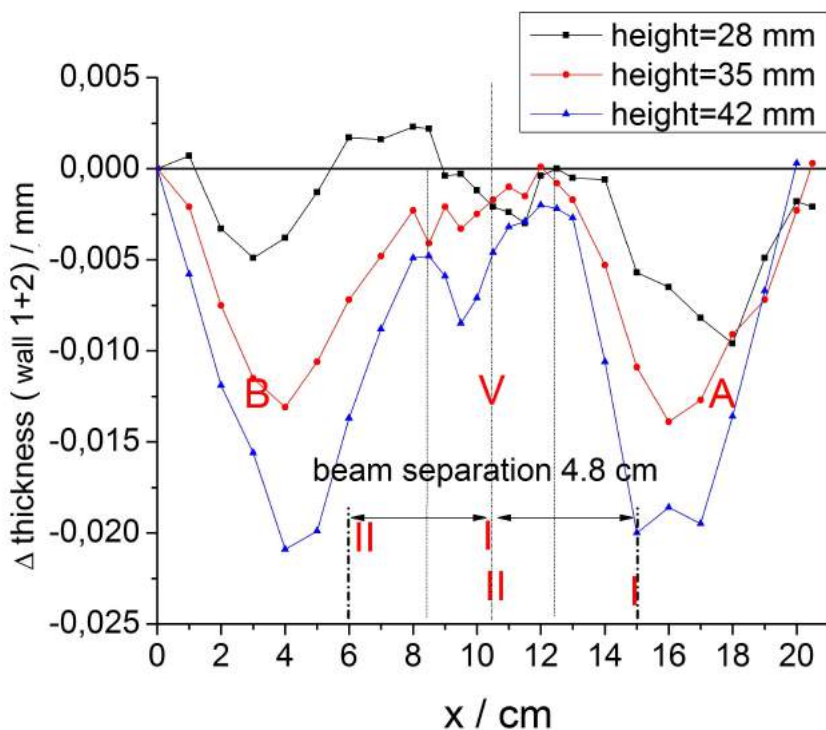


Figure A.22.: Sum of the thickness-change of both chamber walls.

Bibliography

- [1] A. Authier. *Dynamical Theory of X-Ray Diffraction*. Oxford Univ Pr. (2001)
- [2] H. Rauch and S. Werner. *Neutron Interferometry*. Oxford: Clarendon Press (2000)
- [3] V. Sears. *Neutron optics: an introduction to the theory of neutron optical phenomena and their applications*. Oxford: Clarendon Press (1989)
- [4] J. Springer, M. Zawisky, H. Lemmel and M. Suda. *A neutron interferometric measurement of a phase shift induced by Laue transmission*. Acta Cryst. A 66, 17-21 (2010)
- [5] A. Ioffe and M. Vrana. *A new neutron interferometry approach in the determination of the neutron-electron interaction amplitude*. Appl. Phys. A 74, 314-316 (2002)
- [6] G. Greene and V. Gudkov. *Neutron interferometric method to provide improved constraints on non-Newtonian gravity at the nanometer scale*. Phys. Rev. C 75, 015501 (2007)
- [7] H. Lemmel. *IFMSIM manual, Simulation Software for Neutron Interferometers*. unpublished, (2013)
- [8] W. Graeff et al. Acta. Cryst. A 34, 238 (1978)
- [9] H. Rauch. *Wave-Particle Properties Measured by Neutron Interferometry*. Nucl. Instrum. and Meth. A 284, 156-160 (1978)
- [10] K. Hirano and A. Momose. *Investigation of the Phase Shift in X-Ray Forward Diffraction Using an X-Ray Interferometer*. Phys. Rev. Lett. 76/20, 3735-3737 (1996)
- [11] H. Lemmel. *Dynamical diffraction of neutrons and transition from beam splitter to phase shifter case*. Phys. Rev. B 76, 144305 (2007)
- [12] H. Lemmel. *Influence of Bragg diffraction on perfect crystal neutron phase shifters and the exact solution of the two-beam case in the dynamical diffraction theory*. Acta Cryst. A 69, 459-474 (2013)
- [13] T. Potocar, M. Zawisky, H. Lemmel, J. Springer and M. Suda. *Neutron interferometric measurement and calculation of a phase shift induced by Laue transmission*. Acta Cryst. A 71, 534-541 (2015)
- [14] R. Colella, A. Overhauser and S. Werner. *Observation of Gravitationally Induced Quantum Interference*. Phys. Rev. Lett. 34, 1472 (1975)
- [15] M. Zawisky, J. Springer and H. Lemmel. *High angular resolution neutron interferometry*. Nucl. Instrum. and Meth. A 634, 46-49 (2011)

-
- [16] P. Brax and G. Pignol. *Strongly Coupled Chameleons and the Neutronic Quantum Bouncer*. Phys. Rev. Lett. 107, 111301 (2011)
- [17] P. Brax, G. Pignol and D. Roulier. *Probing Strongly Coupled Chameleons with Slow Neutrons*. arXiv: 1306.6536v1 (2013)
- [18] J. Alves, C. Bertout, F. Combes, A. Ferrara, T. Forveille, T. Guillot, R. Napiwotzki, H. Peter, S. Shore, E. Tolstoy and M. Walmsley *Planck 2013 results*. Astronomy & Astrophysics 571 (2014)
- [19] H. Lemmel, P. Brax, A. Ivanov, T. Jenke, G. Pignol, M. Pitschmann, T. Potocar, M. Wellenzohn, M. Zawisky and H. Abele. *Neutron Interferometry constrains dark energy chameleon fields*. Phys. Lett. B 743, 310-314 (2015)
- [20] W. Stirling. *Institut Laue-Langevin*. <http://www.ill.eu/> (2015)
- [21] H. Rauch and D. Petraschek. *Grundlagen fuer ein Laue-Neutroneninterferometer*. AIAU 76401 (1974)
- [22] M. Goldberger and F. Seitz. *Theory of the Refraction and the Diffraction of Neutrons by Crystals*. Phys. Rev. 71, 294 (1947)
- [23] B. Batterman and H. Cole. *Dynamical Diffraction of X Rays by Perfect Crystals*. Rev. Mod. Phys. 36, 681 (1964)
- [24] M. Laue. *Roentgenstrahleninterferenzen*. Akad. Verlagsges. Leipzig (1941)
- [25] H. Bethe. *Theorie der Beugung von Elektronen an Kristallen*. Ann. Phys. Leipzig 87, 55 (1928)
- [26] M. Laue. *Materiewellen und Interferenzen*. Akad. Verlagsges. Leipzig (1948)
- [27] M. Hart. *Ten years of X-ray interferometry (Royal Society Review Lecture)*. Proc. Roy. Soc. Lond. A 346, 1-22 (1975)
- [28] P. Mohr, B. Taylor and D. Newell. *CODATA Recommended Values of the Fundamental Physical Constants: 2010*. J. Phys. Chem. Ref. Data 41, 043109 (2012)
- [29] M. Zawisky, J. Springer, R. Farthofer and U. Kuetgens. *A large-area perfect crystal neutron interferometer optimized for coherent beam-deflection experiments: Preparation and performance*. Nucl. Instrum. and Meth. A 612, 338-344 (2010)
- [30] J. Springer. *Neutron interferometric investigation of phase shifts arising from dynamical diffraction theory*. TU Vienna, PhD thesis (2009)
- [31] C. Shull. *Observation of Pendelloesungs fringe structure in neutron diffraction*. Phys. Rev. Lett. 21, 1585-1589 (1968)
- [32] J. Summhammer. *Temperaturgradienten im LLL-Neutroneninterferometer*. TU Vienna, Master thesis (1980)
- [33] S. Mayer. *Experimente zur Phasenstabilitaet eines Neutroneninterferometers*. TU Vienna/Graz, Master thesis (2003)
- [34] U. Bonse and E. te Kaat. *A two-crystal x-ray interferometer*. Z. Phys., 214:16 (1968)

-
- [35] Wavelength Electronics. *LFI-3751 with Autotune PID Thermoelectric Temperature Controller*. Manual
- [36] F. Wiedtfeldt, M. Huber, T. Black, H. Kaiser, M. Arif, D. Jacobson and S. Werner. *Measuring the neutron's mean square charge radius using neutron interferometry*. Physica B, 385-386:1374-1376 (2006)
- [37] M. Baron. *Messung von Quantenzuständen im Neutroneninterferometer*. TU Vienna, PhD thesis (2005)
- [38] L. Bergmann and C. Schaefer. *Experimentalphysik III*. de Gruyter (1993)
- [39] V. Sears. *Electromagnetic neutron-atom interaction*. Physics Reports 141, 281-317 (1986)
- [40] J. Sparenberg and Leeb. *Neutron-electron scattering length deduced from Pendelloesung interferometry in neutron Bragg reflections on silicon*. J. Electron. Spectrosc. Relat. Phenom. 129, 315-317 (2003)
- [41] J. Khoury and A. Weltman. *Chameleon Cosmology*. Phys. Rev. D 69, 044026 (2004)
- [42] H. Winther. *Chameleon Model with Field-dependent Couplings*. Master thesis, Institute of Theoretical Astrophysics University of Oslo (2010)
- [43] J. Khoury. *Chameleon Field Theories*. arXiv: 1306.4326v1 (2013)
- [44] P. Brax, C. van de Bruck, A. Davis, J. Khoury and A. Weltman. *Detecting dark energy in orbit: The cosmological chameleon*. Phys. Rev. D 70, 123518 (2004)
- [45] T. Jenke, G.Cronenberg, P. Geltenbort, A. Ivanov, T. Lauer, T. Lins, U. Schmidt, H. Saul and H. Abele. *A quantized frequency reference in the short-ranged gravity potential and its application for dark matter and dark energy searches*. arXiv:1208.3875v1 [hep-ex] (2012)
- [46] T. Jenke, G.Cronenberg, J. Burgdoerfer, L. Chizhova, P. Geltenbort, A. Ivanov, T. Lauer, T. Lins, S. Rotter, H. Saul, U. Schmidt, and H. Abele. *Gravity Resonance Spectroscopy Constrains Dark Energy and Dark Matter Scenarios*. arXiv:404.4099v1 [gr-qc] (2014)
- [47] A. Ivanov, R. Hoellwieser, T. Jenke, M. Wellenzohn and H. Abele. *Influence of the chameleon field potential on transition frequencies of gravitationally bound quantum states of ultracold neutrons*. Phys. Rev. D 87, 105013 (2013)
- [48] A. Ivanov. *Neutron Interferometer as Laboratory for Testing of Chameleon Field*. (2014)
- [49] H. Kaiser, H. Rauch, G. Badurek, W. Bauspiess and U. Bonse. *Measurement of Coherent Neutron Scattering Lengths of Gases*. Z. Physik A 291, 231-238 (1979)
- [50] Sears 1992 and Rauch 2001. *Table of coherent scattering lengths and cross sections*. <http://www.ati.ac.at/~neutropt/scattering/table.html>
- [51] J. Steinhart and S. Hart. *Calibration curves for thermistors*. DEEP-SEA RES 15, 497-503 (1968)

- [52] H. Lemmel. *Neutron Interferometry Data Analysis, Script for Igor Pro* unpublished (2014)